

# AUS Repository

## A Static and Snapthrough Analysis of an Innovative Bistable Composite Wing

Item Type	Thesis
Authors	Hijazi, Sara
Download date	2026-04-16 12:05:37
Link to Item	<a href="http://hdl.handle.net/11073/25150">http://hdl.handle.net/11073/25150</a>

A STATIC AND SNAPTHROUGH ANALYSIS OF AN INNOVATIVE  
BISTABLE COMPOSITE WING

by  
Sara Hijazi


A Thesis presented to the Faculty of the  
American University of Sharjah  
College of Engineering  
In Partial Fulfilment  
of the Requirements  
for the Degree of  
  
Master of Science in  
Mechanical Engineering

Sharjah, United Arab Emirates

December 2022

## Declaration of Authorship

I declare that this thesis is my own work and, to the best of my knowledge and belief, it does not contain material published or written by a third party, except where permission has been obtained and/or appropriately cited through full and accurate referencing.

Signed..... Sara Hijazi 

Date..... **January 5, 2023**

The Author controls copyright for this report.

Material should not be reused without the consent of the author. Due acknowledgement should be made where appropriate.

© Year 2022

Sara Hijazi  
ALL RIGHTS RESERVED

## Approval Signatures

We, the undersigned, approve the Master's Thesis of Sara Hijazi



Thesis Title: A Static and Snapthrough Analysis of an Innovative Bistable Composite Wing

Date of Defense: November 17, 2022

### Name, Title and Affiliation

### Signature

---

Dr. Samir Emam  
Professor, Department of Mechanical Engineering  
Thesis Advisor

---

Dr. Maen Alkhader  
Associate Professor, Department of Mechanical Engineering  
Thesis Committee Member

---

Dr. Farid Abed  
Professor, Department of Civil Engineering  
Thesis Committee Member

---

Dr. Mamoun Abdel-Hafez  
Head  
Department of Mechanical Engineering

---

Dr. Lotfi Romdhane  
Associate Dean for Graduate Affairs and Research  
College of Engineering

---

Dr. Fadi Aloul  
Dean  
College of Engineering

---

Dr. Mohamed El-Tarhuni  
Vice Provost for Graduate Studies  
Office of Graduate Studies

## **Acknowledgements**

Foremost, I would like to thank my advisor Dr. Samir Emam for his efforts, continuous guidance, patience, motivation, and immense knowledge throughout this research. His guidance helped me in all the time of research and writing of this thesis.

Beside my advisor, I would like to thank the members of my thesis committee, Dr. Maen Alkhader and Dr. Farid Abed for their insightful comments, suggestions, and questions.

I would like to thank my university for giving me the opportunity to develop my academia career and improve my skills through the Graduate Teaching Assistantship (GTA).

Finally, I am eternally grateful to my family and my friend Khalid who always supported me unconditionally and never hesitated or thought twice in providing me with the best they could, without them, this day would not have been possible.

## Abstract

This thesis presents a numerical analysis of the room-temperature shapes and snapthrough response of thermally induced hybrid bistable symmetric laminates. The bistable laminate is clamped at one end and free at the other end to extend the applications of bistable laminates to non-free-free boundary conditions. The hybrid layup resolves the issue of losing the bistability of the laminate when attached to a larger structure or clamped. Bidirectional (BD) glass-epoxy layers are symmetrically embedded in the laminate's layup to trigger the bistability. An approximate analytical model that is based on the Rayleigh-Ritz method along with the ABAQUS Finite Element (FE) package are used in the analysis. The model is validated against the results available in the literature and a good agreement is obtained. The significance of the BD layers on the thermally induced room-temperature shapes and the snapthrough response is examined. Three parameters are considered: the BD layers' width, thickness, and location from the laminate's center. It is found out that the three parameters greatly affect the static equilibrium shapes and the snapthrough/snapback response. This analysis complements the ongoing research on the bistable laminates for morphing applications. The second part of this study is to propose an innovative design of a bistable wing which has a symmetric flat platform followed by a winglet that utilizes the modified hybrid symmetric bistable laminate. The snap-through and snap-back responses under concentrated load of the proposed design is investigated. The proposed design is referred to as an innovative hybrid bistable laminate i-HBSL throughout this thesis.

**Keywords:** Bistable composite laminates; unsymmetric laminates; bistability; snapthrough; Rayleigh-ritz.

## Table of Contents

Abstract .....	5
List of Figures .....	9
List of Tables .....	13
Nomenclature .....	14
Chapter 1. Introduction .....	15
1.1. Bistable Composite Laminates.....	15
1.2. Thesis Organization.....	16
1.3. Thesis Objectives.....	16
Chapter 2. Background and Literature Review.....	18
2.1. History and Basic Foundation.....	18
2.1.1. Hyer's analytical scheme.....	19
2.2. Snapthrough Analysis Review.....	21
2.3. Advances in Manufacturing and Design.....	22
2.4. Morphing Applications using Bistable Composite Laminates.....	24
Chapter 3. Problem Formulation.....	31
3.1. Base Model.....	31
3.1.1. Rayleigh-ritz method.....	33
3.1.2. The newton raphson method.....	34
3.2. Square plate - Extended Model.....	35
3.3. Compound plate - Extended Model.....	37
3.4. Hybrid Bistable Symmetric Laminate (HBSL).....	39
Chapter 4. Methodology .....	47
4.1. Base Model.....	47
4.2. Square plate - Extended Model.....	48
4.3. Compound plate - Extended Model.....	51
4.4. Hybrid Bistable Symmetric Laminates (HBSL).....	53
4.4.1. Analytical analysis of the hbsl.....	53
4.4.2. Finite element analysis of the hbsl.....	54

4.5.	Modified Hybrid Bistable Symmetric Laminates (m-HBSL).....	57
Chapter 5. Parametric Study on M-HBSL .....		59
5.1.	Effect of varying BD Glass Epoxy Layer Width.....	59
5.2.	Effect of the BD Glass Epoxy Layer Thickness.....	62
5.3.	Effect of the BD Glass Epoxy Layer Location.....	64
Chapter 6. An Innovative Bistable Wing.....		68
6.1	Analytical Model of an Innovative Hybrid Bistable Symmetric Laminate..	68
6.2.	Finite Element Implementation.....	73
6.2.1.	Snapthrough analysis .....	73
Chapter 7. Results and Discussion.....		75
7.1.	Effect of the Length of the Flat Segment.....	77
7.2.	Effect of the BD Glass Epoxy Layer Thickness.....	77
7.3.	Effect of the BD Glass Epoxy Layer Location.....	79
7.4.	Effect of the Concentrated Load Location.....	82
7.5.	Effect of the Thickness Mismatch.....	84
Chapter 8. Conclusion and Future Work .....		87
8.1.	Future Work.....	88
References.....		89
Appendix A. Fundamentals of Composite Materials.....		93
A.1.	Lamina and Laminate.....	93
A.2.	Fibers and Matrix.....	93
A.3.	Elastic Material Behaviour in Composite Material.....	94
A.3.1.	Stiffness matrix $C_{ij}$ .....	94
A.3.2.	Compliance matrix $S_{ij}$ .....	95
A.3.3.	Plane-stress assumption. ....	96
A.3.4.	Transformation of axes - ply orientation.....	98
A.3.5.	Transformed stiffness and compliance matrices.....	99
A.4.	Laminate Formulation.....	99
A.4.1.	Classical lamination theory.....	99
A.4.2.	Laminate displacements.....	101

A.4.3. Laminate strains. ....	101
A.4.4. Laminate stresses. ....	102
A.4.5. The ABD matrix.....	102
A.4.6. Laminate layup and stacking.....	105
A.4.7. Thermal loading. ....	106
Vita.....	108

## List of Figures

Figure 2-1: Laminate's shape $[0/90]_T$ (a) at elevated curing or room temperature (b) saddle shape (c) first cylindrical shape (d) second cylindrical shape [3].	19
Figure 2-2: Geometry of the force acting on the $[0/90]_T$ bistable laminate Danno and Hyer [14].	22
Figure 2-3: The effect of clamping on the bistability characteristics of: (a) The unsymmetric cross-ply laminate proposed by Hyer [12], (b) The multisectioned laminate consisting of symmetric and unsymmetric laminate developed by [22], The multisectioned bistable laminate clamped at both ends proposed by [23], (d) The hybrid bistable symmetric laminate proposed by [25].	24
Figure 2-4: Lateral view of the stable shapes for camber change of airfoil section [26].	25
Figure 2-5: Left: Lateral shape view for chord length change. Right: Isometric shape view for chord length change. (a) first stable shape (b) second stable shape [26].	27
Figure 2-6: Stacking sequence used in the bistable winglet, after [27].	28
Figure 2-7: First stable configuration - Extended Configuration (b) Second stable configuration - Deployed Configuration for the bistable winglet application [27].	28
Figure 2-8: Symmetric and unsymmetric stacking regions of the variable camber trailing edge design, after [27].	29
Figure 2-9: First stable configuration - Deployed Configuration (b) Second stable configuration - Extended Configuration for the variable camber trailing edge application [27].	29
Figure 2-10: Stacking Sequence of the bistable laminate, after [28].	30
Figure 2-11: Camber change region on rotor blade [28].	30
Figure 3-1: Schematic of the stacking sequence of the modified hybrid bistable laminate (m-HBSL) top and isometric view.	40
Figure 4-1: Variation of the principal curvature $\kappa_x$ and $\kappa_y$ with the width-to-thickness ratio for 8-ply $[90_4/0_4]_T$	48

Figure 4-2: The obtained configurations of 8-ply $[90_4/0_4]_T$ square laminate using base model. (a) Saddle unstable shape (b) First stable cylindrical shape (c) Second stable cylindrical shape. ....	49
Figure 4-3: Principal curvatures comparison of the base and extended model. ....	50
Figure 4-4: The unstable and stable equilibrium shapes using the extended model (a) The first stable equilibrium configuration (b) The second stable equilibrium configuration. ....	51
Figure 4-5: The stable equilibrium shapes of the compound plate using analytical model with ABAQUS FE and experiment of Mattioni et al. [22] (a) longitudinal cross section of the curled configuration (b) Unsymmetric cross section of the flat configuration. ....	52
Figure 4-6: The stable equilibrium shapes of the compound plate obtained using ABAQUS FE (a) Curled configuration (b) Flat configuration. ....	53
Figure 4-7: Bistable shapes of clamped HBSL using the current model and the ABAQUS results of Mukherjee et. al [10] for free-free and clamped boundary conditions. ....	54
Figure 4-8: The equilibrium shapes of HBSL with free-free boundary conditions using FEA (a) First stable shape (b) Second stable shape. ....	55
Figure 4-9: Contour maps of transverse bending curvature $\kappa_y$ (free-free boundary conditions) ....	55
Figure 4-10: Contour maps of longitudinal bending curvature $\kappa_x$ (free-free boundary conditions) ....	55
Figure 4-11: The equilibrium shapes of HBSL with clamped boundary conditions (a) First stable shape (b) Second stable shape. ....	56
Figure 4-12: Contour maps of transverse bending curvature $\kappa_y$ (clamped boundary conditions) ....	57
Figure 4-13: Contour maps of longitudinal bending curvature $\kappa_x$ (clamped boundary conditions) ....	57
Figure 4-14: Bistable shapes of m-HBSL using the current model, ABAQUS and experimental results of [10]. ....	58
Figure 5-1: A schematic of the laminate's cross section showing the bidirectional layer width. ....	59

Figure 5-2: The equilibrium shapes of clamped m-HBSL with varying bidirectional ply width using analytical model and ABAQUS.....	60
Figure 5-3: The lateral load-tip deflection curves of a clamped m-HBSL with varying bidirectional width using the ABAQUS FE and the variation of the longitudinal curvature $\kappa x$ with the applied load for a clamped m-HBSL with varying bidirectional width using analytical model. ....	61
Figure 5-4: A schematic of the laminate's cross section showing the bidirectional layer thickness. ....	62
Figure 5-5: Bistable shapes of a clamped m-HBSL with varying bidirectional plies' thickness using the analytical model and ABAQUS. ....	63
Figure 5-6: The lateral load-tip deflection curves of a clamped m-HBSL with varying bidirectional thickness using ABAQUS FE and the variation of the longitudinal curvature $\kappa x$ with the applied load for a clamped m-HBSL with varying bidirectional width using analytical model. ....	63
Figure 5-7: Schematic figure of the BD layer's location (a) $Z_{BD}/h = 0.5$ (b) $Z_{BD}/h = 1$ . ....	65
Figure 5-8: Bistable shapes of a clamped m-HBSL with varying bidirectional plies' location using ABAQUS FE.....	65
Figure 5-9: Load-deflection curves of a clamped m-HBSL with varying bidirectional plies' location using ABAQUS FE.....	66
Figure 5-10: Midplane strain colormap for different configurations (a-b) $Z_{BD}/h = 0$ (c-d) $Z_{BD}/h = 0.5$ .....	67
Figure 6-1: Schematic figure of the proposed innovative composite wing. ....	68
Figure 6-2: Schematic of the stacking sequence of the proposed innovative bistable composite wing (i-HBSL).....	69
Figure 6-3: Isometric view of the proposed innovative bistable composite wing (i-HBSL).....	70
Figure 6-4: Model geometry and coordinate system. ....	71
Figure 6-5: FEA simulation flowchart.....	74
Figure 7-1: Stable equilibrium shapes of the Innovative Composite Wing.....	75
Figure 7-2: Bistable shapes of the innovative composite wing (i-HBSL) using the analytical model and ABAQUS FE.....	76

Figure 7-3: Schematic of the proposed innovative bistable composite wing with $L_1$ varying. ....	77
Figure 7-4: The equilibrium shapes and load-deflection curves at different $L_1/L_2$ ratios. ....	78
Figure 7-5: The stable equilibrium shapes and load-deflection curve of the compound m-HBSL plate with varying bidirectional plies' thickness using ABAQUS. ....	79
Figure 7-6: Contour maps of the longitudinal curvatures $\kappa x$ at different BD layer thickness (a) $t_{BD} = 0.25$ mm (b) $t_{BD} = 0.75$ mm. ....	79
Figure 7-7: The stable equilibrium shapes of the compound m-HBSL and load-displacement plot with varying bidirectional plies' location using ABAQUS. ....	80
Figure 7-8: Contour maps of mid-plane strain at different BD layer location (a-b) $Z_{BD}/h = 0$ (c-d) $Z_{BD}/h = 1$ . ....	81
Figure 7-9: Schematic figure of the load applied at different locations. ....	82
Figure 7-10: The stable equilibrium shapes and load-deflection curve of the compound m-HBSL plate with varying the concentrated load location using ABAQUS. ....	82
Figure 7-11: The intermediate shapes at different load locations, $L_p/L_2 = 0.7$ and $L_p/L_2 = 0.5$ . ....	83
Figure 7-12: Schematic figure of the thickness mismatch. ....	84
Figure 7-13: Load-displacement plot at different -no material- layer thickness. ....	85
Figure A-1: Various types of fiber orientation (a) Continuous (b) Discontinuous [32]. ....	93
Figure A-2: Scheme of a laminate composite material. ....	94
Figure A-3: Coordinates of unidirectional reinforced lamina [33]. ....	97
Figure A-5: Laminated plate geometry. ....	103
Figure A-6: ABD-matrix components and their impact on the laminate deformation [34]. ....	104
Figure A-7: (a) Symmetric Laminate (b) Unsymmetric Laminate [36]. ....	106

## List of Tables

Table 1: Material properties of graphite/epoxy used in the model of Dano and Hyer [29]. .....	31
Table 2: Unknown Coefficients obtained for the cross-ply unsymmetric square laminate $[90_4/0_4]_T$ first shape. ....	35
Table 3: Unknown Coefficients obtained for the cross-ply unsymmetric square laminate $[90_4/0_4]_T$ second shape. ....	35
Table 4: Unknown Coefficients obtained for the cross-ply unsymmetric square laminate $[90_4/0_4]_T$ first shape – Extended. ....	36
Table 5: Unknown Coefficients obtained for the cross-ply unsymmetric square laminate $[90_4/0_4]_T$ second shape – Extended. ....	37
Table 6: Material properties of carbon/epoxy UD and aluminium layers used in HBSL. ....	41
Table 7: Material properties of carbon/epoxy UD and Glass/epoxy BD used in m-HBSL. ....	41
Table 8: A comparison between the curvature of the square plate obtained using the two models. ....	50
Table 9: Comparison of longitudinal curvatures of BHSLs given by FEA and analytical model with free-free boundary conditions. ....	56
Table 10: Comparison of the tip displacement of clamped HBSL using the analytical model and ABAQUS FE. ....	57
Table 11: Comparison of the tip displacement of clamped m-HBSL using the analytical model, ABAQUS FE and experiment. ....	58
Table 12: Comparison of the snapthrough load and tip displacement with varying BD layer width using the analytical model and ABAQUS. ....	61
Table 13: Comparison of the snapthrough load and tip displacement with varying BD layer thickness using the analytical model and ABAQUS. ....	64
Table 14: No material layer thickness. ....	86

## Nomenclature

$C_{ij}$	Stiffness Matrix
$S_{ij}$	Compliance Matrix
$Q_{ij}$	Reduced stiffness Matrix
$N_x$	Resultant force in x-direction
$N_y$	Resultant force in y-direction
$N_{xy}$	Shear force resultant
$M_x$	Bending moment in x-direction
$M_y$	Bending moment in y-direction
$M_{xy}$	Twisting moment
$\bar{Q}_{ij}$	Transformed reduced stiffness
$\epsilon_x^0$	The extensional strain of the reference surface in the x-direction
$\kappa_x^0$	The curvature of the reference surface in the x-direction
$\epsilon_y^0$	The extensional strain of the reference surface in the y-direction
$\kappa_y^0$	The curvature of the reference surface in the y-direction
$\kappa_x$	Principal Curvature in x-direction
$\kappa_y$	Principal Curvature in y-direction
$\sigma_i$	Stress
$\tau_{ij}$	Shear strain
$\gamma_{ij}$	Engineering shear strain
$\epsilon_j$	Strain
$\epsilon_x^0$	Extensional strain of the reference surface in x- direction
$\epsilon_y^0$	Extensional strain of the reference surface in the y-direction

## Chapter 1. Introduction

### 1.1. Bistable Composite Laminates

A composite material is formed by the combination of two or more distinct materials that results in a new material with enhanced properties. Composites that use more than one type of reinforcement materials are called hybrids. Modern composites use metal, ceramic, or polymer binders or matrix reinforced with a variety of fibers or particles. Based on the matrix, the modern-day composites can be classified into metal composites, Ceramic composites, and Polymer composites. Similarly based on the reinforcement, they can be classified into Fiber reinforced composites and Particle or Whisker reinforced composites. Advanced composites are being employed for many industrial applications. Bistable Composites are a common type of unsymmetrical laminate fiber reinforced polymer composites. Bistable composite laminates are excellent candidates for their applications in morphing structures due to their unique features. In fields such as aerospace and automotive, bistable composite laminates are proposed as a method for generating novel-shape-changing structures [1, 2]. The interest in bistable composites stems from the fact that they are able to sustain significant changes in shape without the need for a continuous power supply. Bistable composite laminates are relatively thin unsymmetric laminates, commonly  $[0_n/90_n]_T$ , which have been cured at elevated temperature. Such composites are multi-stable and exhibit as at least two distinct structurally stable shapes as a result of anisotropic thermal expansions of the composite plies creating a residual stress field during manufacture [3, 4, 5]. The bistability of unsymmetric composite laminate configurations, such as  $[0_n/90_n]_T$ , has been extensively studied for many years both analytically and experimentally. In such laminates bistability occurs due to geometric nonlinearity and opposing residual stresses as a result of thermal contraction of the matrix and fibre materials upon cool down from curing. However, a bistable laminate is not necessarily unsymmetric in its lay-up. One of the solutions proposed recently is to mechanically prestress the fibers in selected plies prior to cure in an otherwise symmetric lay-up. It has been noticed that the snap-through forces required for bistability were dependent on the location and magnitude of prestress within a laminate. Shape memory alloys and piezoelectric materials have been used as actuator materials to induce snap-through between stable states [6, 7, 8, 9]. It can be said that if the thermal

load is applied to the unsymmetric composite laminates, they will have two cylindrical stable states in addition to an unstable saddle shape. This cannot be predicted with the classical lamination theory with these two configurations. The analytical model, used in various research, was based on the total potential energy and the Rayleigh–Ritz method using a geometrical nonlinearity. Regions of locally reversed curvature which are seen near the corners and edges of bistable laminates are not currently predicted by analytical methods. While localized variation in curvature has been predicted using finite element technique. The detailed review of what is a composite, fiber reinforced composite material and unsymmetric laminates is presented in appendix A.

## **1.2. Thesis Organization**

Chapter 2 gives a brief summary of the development and current research on bistable composite materials. Chapter 3 presents the methodology and formulation. Chapter 4 presents validation results. Chapter 5 presents a parametric study on the snapthrough of the m-HBSL model proposed in the literature. Chapter 6 provides the analytical model and numerical steps used for the proposed design “innovative bistable symmetric composite wing”. In Chapter 7, a parametric study is conducted on the proposed model, the i-HBSL. A summary and an overview of future work are presented in Chapter 8.

## **1.3. Thesis Objectives**

When asymmetric laminates get clamped or attached to a larger structure, they lose their bistability behaviour. Therefore, to overcome this undesirable phenomena, researchers investigated different lay-ups to maintain the bistability behaviour, leading to the hybrid laminates. In this section, an overview of the main objectives of the thesis is provided. The ultimate objective of the thesis is to investigate the effect of the geometric parameters on the equilibrium shapes and snapthrough loads of the modified hybrid bistable laminates, and then produce an innovative design for a bistable wing that has a flat platform followed by a modified hybrid symmetric bistable winglet. Prior to starting with the main objective of the thesis, the analytical models proposed in the literature are validated. Therefore, the thesis is divided into two parts: a parametric study on the modified hybrid bistable symmetric laminates (m-HBS) proposed by Mukherjee et al. [10], and a parametric study on the proposed innovative hybrid bistable symmetric wing (i-HBSL). The main objectives of the thesis are the following:

- Conduct a parametric study of the modified bistable symmetric laminate clamped model proposed by Mukherjee et al. [10] .
- Propose an innovative design of a bistable wing that has a flat platform followed by a modified bistable symmetric laminate.
- Generate the equilibrium shapes of the proposed model (i-HBSL).
- Study the static response under concentrated load of the proposed design.
- Perform a parametric study on the influence of the key geometric and material parameters on the shape and snapthrough of the proposed wing.
- Verify the results of the proposed analytical model using ABAQUS FE analysis.

## Chapter 2. Background and Literature Review

Bistable composite laminates were initially introduced by Hyer [3]. Since then, there has been a continuous research efforts on this topic using analytical, experimental, and numerical methods. In this chapter, an overview of the past and recent literature on bistable laminates has been compiled, summarized, and analyzed. The literature review covers the history and basic foundation and the applications of bistable composite laminates.

### 2.1. History and Basic Foundation

A Bistable laminate is a composite structure that has two stable configurations. It can snap from one stable configuration to another by applying a load that is sufficient to cross the potential barriers between the two states. No continuous load is required to maintain the structure at its equilibrium position. The action to switch back is called snapback. Bistable composite laminates are used in many aerospace and industrial applications for their potential in morphing and energy harvesting. According to the literature, thermal curing is the most common method of manufacturing bistable composites [11].

Hyer [3] was the first to report multistability in thin unsymmetric laminates  $[0/90]_T$ . The unsymmetric laminates were initially found undesirable due to their bending-stretching coupling. The room temperature shapes of all unsymmetric laminates were showed to be saddle shape using the classical lamination theory which is linear. The other equilibrium and stable shapes still exist but the theory is not capable to predict them since it is based on a linear analysis and very limited. Hence, the physics and mechanics of the problem are lost. However, Hyer [12] proved that this conclusion applies on thick laminates. When the laminate is thick enough, it remains almost flat and does not show the bistability behaviour. Hyer's [12] analysis used a nonlinear theory to large deformation, where the two bistable cylindrical shapes can be captured. In this case, the saddle shape is unstable and we can only get it mathematically, but it does not exist in reality. The only two stable shapes that the structure can stand or assume at the room temperature without applying any loads are the cylindrical shapes. The thermal curing of thin laminates leads to the development of residual thermal stresses, which results in multistability. Figure 2-1 corresponds to the flat laminate in

the cured state at the elevated curing temperature. As the laminate settles to any of the shapes shown in Figure 2-1b, 2-1c, 2-1d, based on the initial guess of the equilibrium state that minimizes the total potential energy.

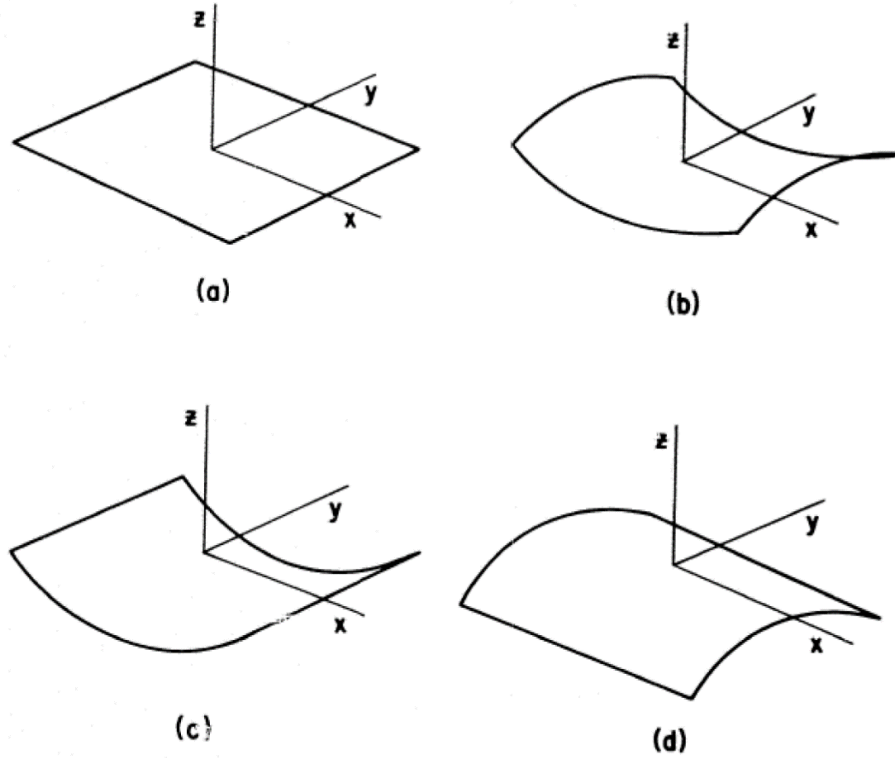


Figure 2-1: Laminate's shape  $[0/90]_T$  (a) at elevated curing or room temperature (b) saddle shape (c) first cylindrical shape (d) second cylindrical shape [3].

**2.1.1. Hyer's analytical scheme.** Hyer [12] provided the first approximate analytical model for predicting the equilibrium shapes of bistable laminates. His study was based on developing an analytical solution using the Rayleigh-Ritz method as an extension method of the classical lamination theory. The total potential energy was calculated as:

$$U = \int_V \left( \frac{1}{2} C_{ijkl} \epsilon_{ij} \epsilon_{kl} - \beta_{ij} \epsilon_{ij} \Delta T \right) dV \quad (1)$$

where,  $C_{ijkl}$  are the elastic constants of the material,  $\beta_{ij}$  are the thermo-mechanical coefficients,  $\epsilon_{ij}$  are the strain components and  $\Delta T$  is the change in temperature from

curing to room temperature. Based on the Classical Lamination Plate theory (CLPT), the strain-displacement relations were assumed as:

$$u(x, y, z) = u^0(x, y) - z \frac{\partial w^0(x, y)}{\partial x} \quad (2)$$

$$v(x, y, z) = v^0(x, y) - z \frac{\partial w^0(x, y)}{\partial y} \quad (3)$$

$$w(x, y, z) = w^0(x, y) \quad (4)$$

As stated earlier, Hyer [12] accounted for nonlinearity in the formulation by assuming Von Kármán strains as:

$$\epsilon_x = \epsilon_x^0 + z\kappa_x^0 \quad (5)$$

$$\epsilon_y = \epsilon_y^0 + z\kappa_y^0 \quad (6)$$

$$\gamma_{xy} = \gamma_{xy}^0 + z\kappa_{xy}^0 \quad (7)$$

where the strain and curvatures are defined as:

$$\{\epsilon^0\} = \begin{Bmatrix} \epsilon_x^0 \\ \epsilon_y^0 \\ \gamma_{xy}^0 \end{Bmatrix} = \begin{Bmatrix} \frac{\partial u^0}{\partial x} + \frac{1}{2} \left( \frac{\partial w^0}{\partial x} \right)^2 \\ \frac{\partial v^0}{\partial y} + \frac{1}{2} \left( \frac{\partial w^0}{\partial y} \right)^2 \\ \frac{\partial u^0}{\partial y} + \frac{\partial v^0}{\partial x} + \frac{\partial w^0}{\partial x} \frac{\partial w^0}{\partial y} \end{Bmatrix}, \{\kappa^0\} = \begin{Bmatrix} \kappa_x^0 \\ \kappa_y^0 \\ \kappa_{xy}^0 \end{Bmatrix} = \begin{Bmatrix} -\frac{\partial^2 w^0}{\partial x^2} \\ -\frac{\partial^2 w^0}{\partial y^2} \\ -2 \frac{\partial^2 w^0}{\partial x \partial y} \end{Bmatrix} \quad (8)$$

To solve for the equilibrium shapes the out of plane displacement  $w^0$  was assumed as:

$$w^0 = \frac{1}{2}(ax^2 + by^2) \quad (9)$$

The unknown coefficients are  $a$  and  $b$ , where the solution can either have  $a \neq 0, b = 0$  or  $a = 0, b \neq 0$ . The inplane displacements were assumed as:

$$u^0(x, y) = cx - \frac{a^2 x^3}{6} - \frac{abxy^2}{4} \quad (10)$$

$$v^0(x, y) = dx - \frac{b^2 y^3}{6} - \frac{abx^2 y}{4} \quad (11)$$

To ensure there is no shear strain  $\gamma_{xy} = 0$ , a third term has been introduced in the displacement field, and this is expected for cross-ply laminates. Substituting the strain fields into Eq. (1) and taking the first derivation with respect to each unknown, gives a set of nonlinear equations. Solving the set of nonlinear equations gives the equilibrium states of the laminate. However, stability analysis is required to ensure that the obtained solutions are stable. The stability is determined by finding the determinant of the matrix obtained by taking the second variation of the potential energy function [12]. The analytical model of Hyer was restricted to cross-ply laminates, therefore, Jun and Hong [13] modified the model of Hyer [3] by including more terms in the polynomial to include the inplane shear strain and hence extending the model for a general layup. They found that shear strain was indeed negligible for square laminates with very large or small length-to-thickness ratios. However, for intermediate length-to-thickness ratios, shear strain can be significant. Schlecht et al. [14] performed finite element analyses to calculate the room temperature shapes of square unsymmetric cross-ply laminates. The finite element analysis calculations compared very well with the predictions from Hyer's theory [12].

## 2.2. Snapthrough Analysis Review

Following the work presented by Hyer [12], Danno and Hyer [15] proposed a numerical and experimental study to analyze the snapthrough of  $[0/90]_T$  laminate subjected to a concentrated load. The virtual work contribution of the forces was added to the total potential energy to account for the applied load. The virtual work is defined as follows:

$$\delta W_F = \vec{F} \cdot \delta \vec{R}_F|_{(x=L,y=0)} + \vec{F} \cdot \delta \vec{R}_F|_{(x=-L,y=0)} \quad (12)$$

where  $\delta \vec{R}_F$  is the virtual displacement of the force at the supports. The schematic figure of the load acting on the bistable laminate is shown in Figure 2-2. To achieve snapthrough, it is necessary to design an actuation system that produces a force sufficient to cross the potential barrier between the states. Moreover, the location of the applied force plays an important role in the snapthrough.

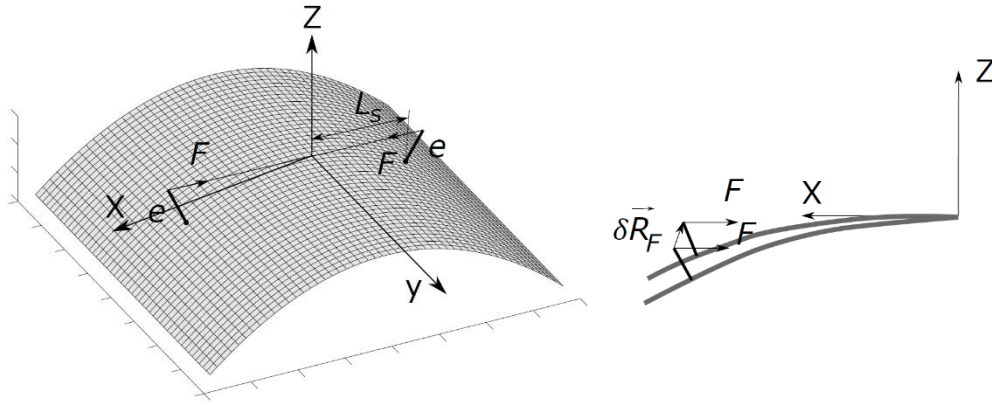


Figure 2-2: Geometry of the force acting on the  $[0/90]_T$  bistable laminate Danno and Hyer [14].

### 2.3. Advances in Manufacturing and Design

Several modifications have been made to the original  $[0/90]_T$  layup initially studied by [3] to achieve different design objectives, e.g., increasing curvatures of stable states and reducing snapthrough loads, ensuring integrability, etc. Daynes and Weaver [16] proposed an unsymmetric hybrid layup by introducing a metal layer in the middle of unsymmetric laminate  $[0/90]_T$ , the purpose of the design is to increase the snapthrough loads and the curvatures of the equilibrium shapes. Due to the thermal contraction of the isotropic metal layer post-curing, it generated significant thermal stresses, resulting in a significant increase in snapthrough loads and principal curvatures. A second attempt was made by Daynes et al. [17] to induce bistability using mechanical prestressing, which eliminates the issue of hygrothermal effect. Moreover, mechanical prestressing allows curvatures and snapthrough loads to be tailored.

To mitigate the stress concentration caused by multisectioned layups, an advanced fiber placement (AFP) technology was introduced by Sousa et al. [18] to manufacture bistable laminates. The bistability and snapthrough characteristics of the bistable VS laminate were investigated using a commercial FE package. Following that, Haldar et al. [19] proposed a semi-analytical scheme based on the Rayleigh-Ritz method to obtain the stable configurations of the variable stiffness composite laminate (VS). Later, Anilkumar et al. [20] studied the snapthrough characteristics of the variable stiffness composite laminates using MFC patches. These bistable VS laminates can be snapped at sufficiently low input voltages, according to the study of Anilkumar et al. [20].

A numerical and experimental investigation on a new category of bistable hybrid composite laminates that consist of CFRP layers in the upper and lower layers and aluminum strips and CFRP in the middle layer is seen in the study of Firouzian-Nejad et al. [21]. The results revealed that the laminates have bistability for wide ranges of geometry and lay-ups and it was possible to adjust the residual curvature and load-carrying capability of the laminate by adjusting the number, width, and thickness of the metallic strips and the laminate geometry. The BHCLs presented were more designable and variable than conventional bistable pure composite laminates for the purpose of tailoring responses. The bistable laminates must be integrated into a larger structure to use them as a structural element. However, the unsymmetric laminate  $[0/90]_T$  seen in the literature either loses bistability or the curvature significantly reduces when clamped. To overcome this phenomena, researchers started to look at different layups in order to avoid using unsymmetric laminate. An important milestone in the development of bistable laminated models was done by Mattioni et al. [22], where a piecewise layup consisting of a symmetric part and unsymmetric part was proposed. Furthermore, the effect of integration on the bistability and snapthrough was investigated.

A subsequent study by Arrieta et al. [23] proposed a bistable laminate with a multi-sectioned layup, which could be clamped at both ends without the loss of bistability. The equilibrium shapes of the model were also obtained using FEA in ABAQUS®. Following this, Daynes et al. [24] developed a symmetric layup  $[0/90/90/0]_T$ , where the bistability was induced through prestressing the outer  $0^\circ$  plies, which leads to mechanical buckle of the central region. The proposed model achieves a two cylindrical equilibrium shapes with principal direction in the opposite direction. However, the manufacturing process of this design requires a special arrangement for the prestressing process.

Li et al. [25] developed an analytical model for a bistable hybrid symmetric laminate consisting of a multisectioned layup made of aluminum and carbon fibers that has two equilibrium shapes, similar to the model proposed by Daynes et al. [24] The study was restricted to free-free boundary conditions. A mismatching, debonding and slip phenomena between the metal and composite was found. Recently, Mukherjee et al. [10] proposed an analytical model of a modified hybrid bistable laminate, where the

aluminum plies were replaced by bidirectional glass/epoxy layers with the same thermal expansion coefficient to eliminate the problem of slippage and debonding between the metal and the carbon-epoxy layers found in [25]. The analytical model was also modified to account for clamped boundary conditions. Figure 2-3 summarizes the development of bistable laminates accounting for clamped boundary conditions.

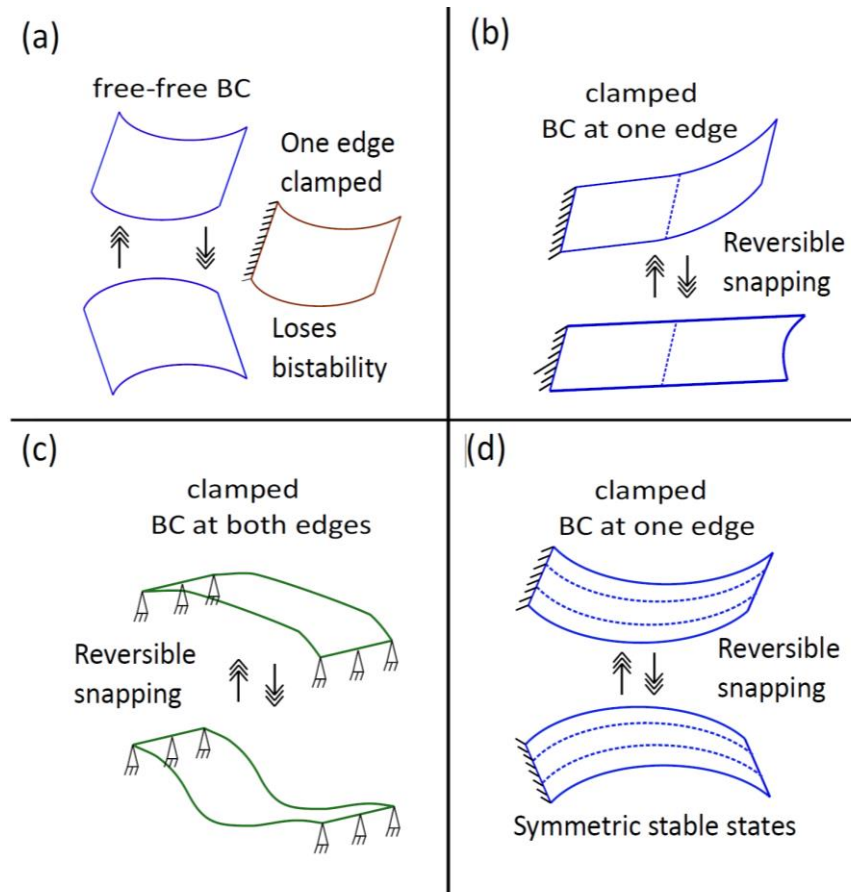


Figure 2-3: The effect of clamping on the bistability characteristics of : (a) The unsymmetric cross-ply laminate proposed by Hyer [12], (b) The multisectioned laminate consisting of symmetric and unsymmetric laminate developed by [22], The multisectioned bistable laminate clamped at both ends proposed by [23], (d) The hybrid bistable symmetric laminate proposed by [25].

## 2.4 Morphing Applications using Bistable Composite Laminates

Morphing structures are commonly used in aerospace, automotive and wing energy for their ability to change shape depending on environmental, operating and load conditions. Bistable laminates are considered as energy-efficient morphing structures since they exhibit more than one stable configuration and remain in the new equilibrium position without continuous application of external force as previously mentioned. Moreover, it was shown that the bistable laminates achieve large deflections by snap-

through process with very small energy input. In the studies of Diaconu et al. [26], carbon-fiber laminated composites with unsymmetric laminate configuration are used for morphing the airfoil section. The airfoil model used is NACA 2301 with a chord of 680 mm, this airfoil section is mainly used in rotor blades. The three proposed morphing concepts for an airfoil section include, morphing of flap-like structure, change in chord length and change in airfoil camber. For the camber change, a square bi-stable composite plate was used with the dimension 234 x 234 mm. The bi-stable plate was placed horizontally along the airfoil chord with three unsymmetric cross-ply laminate configuration.  $[90_4/0_4]_T$   $[90_6/0_6]_T$   $[90_8/0_8]_T$ . These configurations were selected to maintain high loads while keeping large displacement of the plate with a desirable range. Also, placing the bi-stable plate along the chord can support aerodynamic loads transverse to the top and bottom area of the plate (skin). Hence, the bistable-plate acts as an actuator for morphing purposes and also as a stiffener.

It was shown that the airfoil section has two stable configurations as seen in Figure 2-4, the first stable configuration refers to the original airfoil. The location of few parts of the structure were changed in the second stable configuration. These stable configurations are obtained using two concentrated loads applied vertically on the two leading corners of the plate, near the spar. It can be observed that the area between the web and spar (top and bottom skins) bend below and above the bistable plate in the second stable shape. Moreover, the web location behind the bi-stable plate experiences a slight change from its original vertical position. It was noted that all other laminate configurations share similar stable shapes.

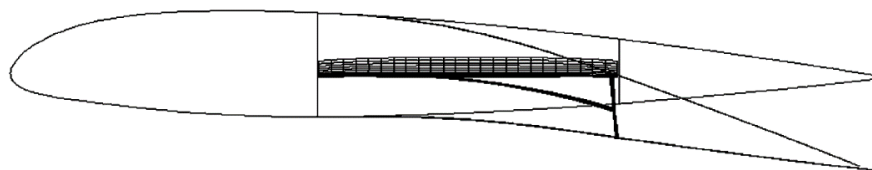


Figure 2-4: Lateral view of the stable shapes for camber change of airfoil section [26].

The magnitude of loads required to actuate the airfoil to switch from one stable configuration to another were evaluated for all the laminate configurations against the displacement of the bi-stable plate. It was observed that the actuation load during the snap-back process have smaller absolute value, since the plate is already loaded with

stresses resulting from the deformation of the rest of the structure. For the chord change, a rectangular bi-stable composite plate was placed vertically along the main spar of the airfoil. The bi-stable plate dimensions are  $L = 300mm$ ,  $W = 70mm$  with two cross-ply unsymmetric laminate configuration,  $[0_2/90_2]_T$  and  $[0_3/90_3]_T$ , both configurations have four and six layers respectively. The chord length of the airfoil will vary between the two stable configurations as the actuation load is applied on the center of the bi-stable composite plate. The bi-stable composite plate continues to snap-through and stabilize into the second stable configuration even when the load is removed, and this is due to the residual stresses.

Figure 2-5 show the two stable configuration of the four layer laminate configuration  $[0_2/90_2]_T$  at two different view. the other six layer laminate configuration shares similar stable shape, but smaller relative distance between their trailing edge was observed. The second stable configuration, half of the bi-stable plate fibers are perpendicular to the chord, hence, the chord change morphing concept also acts as a internal stiffener for the airfoil structure. It is clearly shown that these morphing concepts also have an advantage over the airfoil structure stiffness and aerodynamic performance. The bistability is induced by residual stresses due to thermal curing. Hence, the structures proposed in this study are highly affected by temperature and moisture. The research pointed out that the bistability is enhanced for cold condition. Whereas bistability is likely to disappear at high temperature.

Mattioni et al. [27] investigated different concepts for morphing structures using bistable composites. The results were validated using FEA and experimental data. Three morphing concepts were proposed in his studies, bistable winglet, variable camber trailing edge and variable sweep wing. The structure used in the bistable winglet consist of unsymmetric laminate made of orthotropic materials in which the internal stresses of the laminate produces more than one stable configuration as shown in Figure 2-6. This creates structures that can be at the same time flexible and stiff and opens the possibility of combining several bistable components to obtain structures with multiple configurations. Figure 2-7 represents the two stable configurations of the winglet, the first configuration is named as Extended configuration, where the panel is in flat position and acts as a high-lift device, at a given speed, it switches to the second configuration named as deployed configuration.

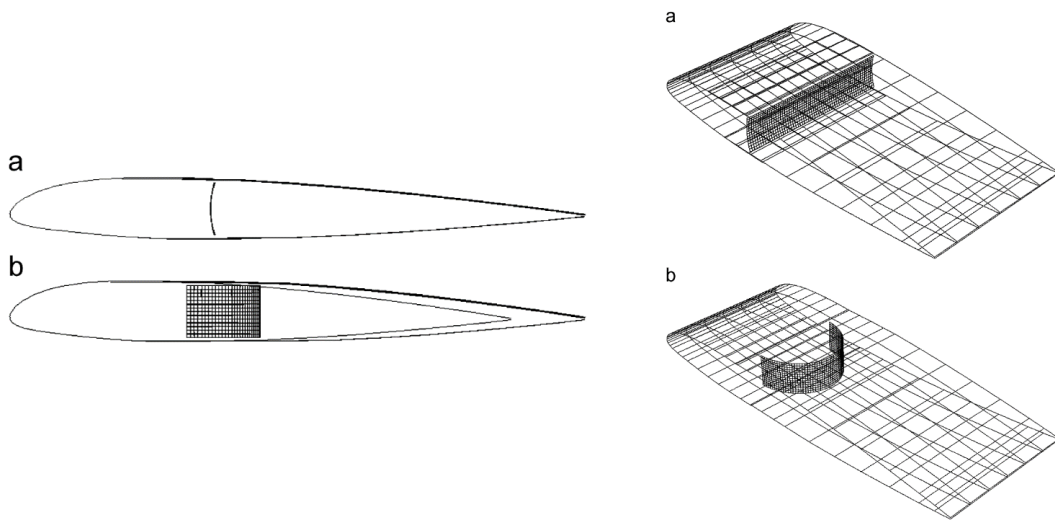


Figure 2-5: Left: Lateral shape view for chord length change. Right: Isometric shape view for chord length change. (a) first stable shape (b) second stable shape [26].

Mattioni et al. [27] investigated different concepts for morphing structures using bistable composites. The results were validated using FEA and experimental data. Three morphing concepts were proposed in his studies, bistable winglet, variable camber trailing edge and variable sweep wing. The structure used in the bistable winglet consist of unsymmetric laminate made of orthotropic materials in which the internal stresses of the laminate produces more than one stable configuration as shown in Figure 2-6. This creates structures that can be at the same time flexible and stiff and opens the possibility of combining several bistable components to obtain structures with multiple configurations. Figure 2-7 represents the two stable configurations of the winglet, the first configuration is named as Extended configuration, where the panel is in flat position and acts as a high-lift device, at a given speed, it switches to the second configuration named as deployed configuration.

The panel in this configuration acts as a blended winglet in which the aerodynamic performance is improved during cruising condition. Furthermore, it was seen the the extended configuration helps in generating lift during take off due to the curvature in the chord-wise direction. On the other hand, the composite plates behaves as a blended winglet when it is in the deployed configuration, due to the curvature resulting from the residual stresses. Therefore, in this configuration, a reduction of the angle of attack can be seen on the wing-tip, which helps in delaying the flow separation

at the wing-tip. The effect of the laminate axis rotation for the bistable winglet was also examined, along with the airspeed at snap for different angle of attack for both configurations. Results show that after the winglet snap, a reduction in the aerodynamic forces is seen. i.e, lift, drag and pitching moment, which confirms that the device can be used to increase the lift of the wing at certain flight conditions, i.e, takeoff and landing. However, a mechanism to snapback to the extended configuration was not yet investigated.

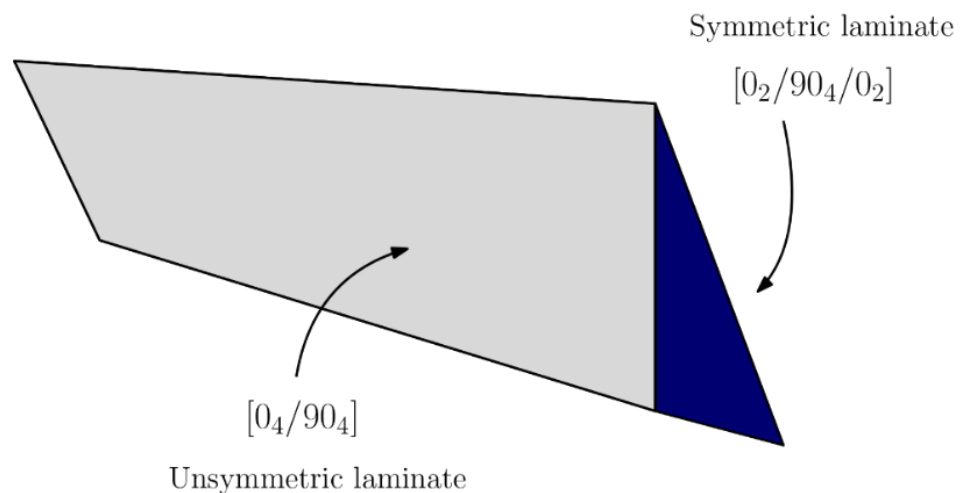


Figure 2-6: Stacking sequence used in the bistable winglet, after [27].

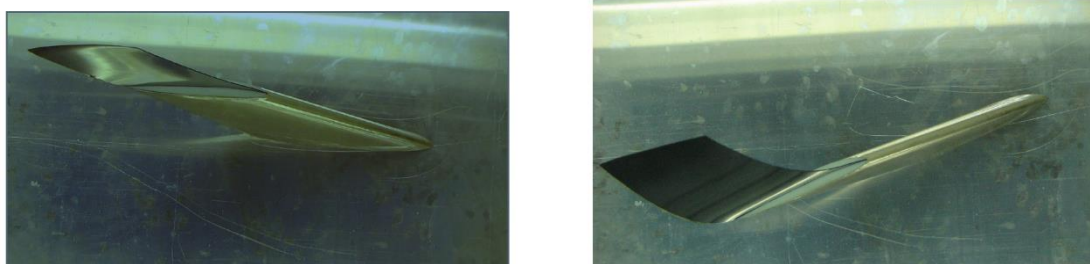


Figure 2-7: First stable configuration - Extended Configuration (b) Second stable configuration - Deployed Configuration for the bistable winglet application [27].

The purpose of this design is to change the camber of the airfoil by morphing the geometry. The shape change is based on the bistability of the unsymmetric patches of the composite material in the upper and lower skin of the trailing-edge. Figure 2-8 shows the geometry and stacking of the device used for the variable camber trailing edge, where the blue areas have unsymmetric stacking sequence, and the gray areas are

symmetric. Four different configurations were obtained for this design, however, only two configurations are used for aerodynamic applications, shown in Figure 2-9. Results showed that the force required to extend the trailing edge is almost a third of that required to obtain the deployed configuration, hence, the deployed configuration has higher stiffness than the extended configuration. In this case, the airfoil will experience an increase in camber, therefore, withstand higher structural loads and generate higher aerodynamic forces.

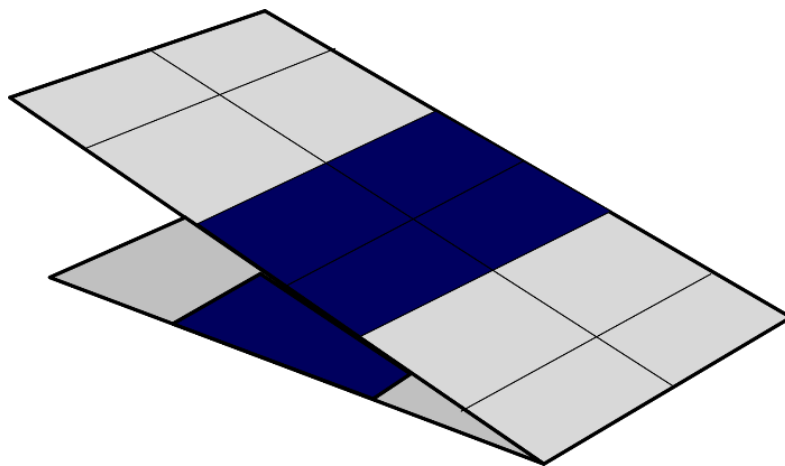


Figure 2-8: Symmetric and unsymmetric stacking regions of the variable camber trailing edge design, after [27].



Figure 2-9: First stable configuration - Deployed Configuration (b) Second stable configuration - Extended Configuration for the variable camber trailing edge application [27].

A bistable airfoil design which has two stable camber geometries was proposed in the study of Daynes et al. [28], the presented design includes a bistable flap which consist of six prestressed buckled laminates. The laminate layup selected is  $[0/90/90/0]_T$  as shown in Figure 2-10, where the blue shaded area represents the  $0^\circ$  layup. This design enables the trailing edge to get deflected downward by 10 degrees

as per the need and to withstand aerodynamic loading at any of the stable configurations without the help of further actuation. In addition, the design proposed is lightweight and achieves a smooth camber variation which improves the aerodynamic flow around the airfoil. Therefore, during the transition from hovering to forward flight, the proposed bistable device could enhance rotor blade performance. The stable states obtained are presented in Figure 2-11.

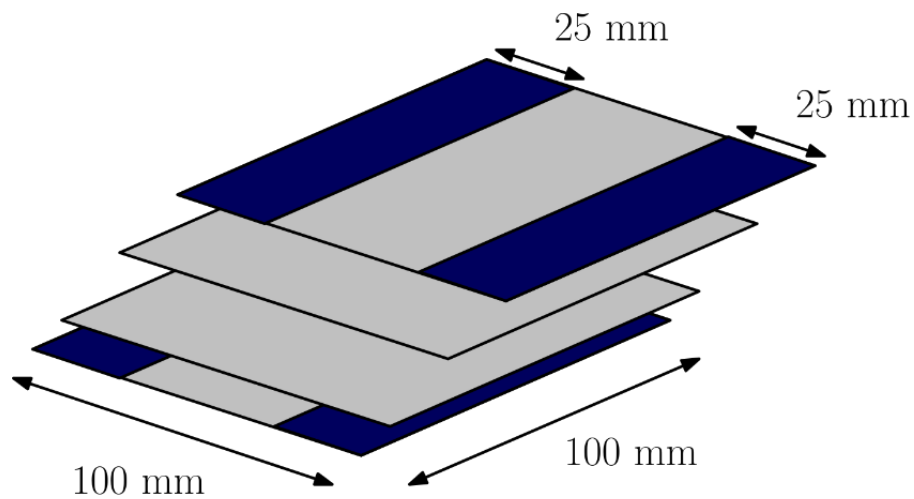


Figure 2-10: Stacking Sequence of the bistable laminate, after [28].

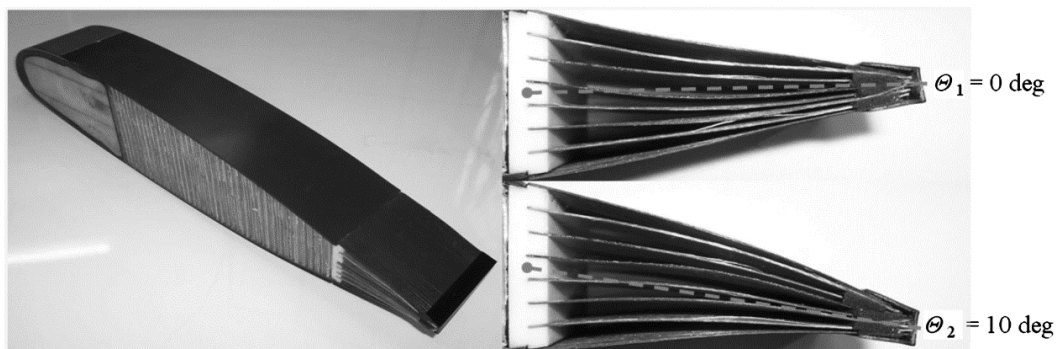


Figure 2-11: Camber change region on rotor blade [28].

## Chapter 3. Problem Formulation

### 3.1. Base Model

Of all the models available in the literature, the model by Dano and Hyer [29] is the most robust and straightforward Emam and Inman [11]. Unsymmetric composite laminates are manufactured by a typical fabrication process. Fabrication loads are subsequently developed during the cure cycle, where the temperature is lowered to room temperature and the cured laminate is then removed from the autoclave. A laminated plate with a length  $L$ , width  $W$ , and a thickness  $h$  is considered for this analysis. The important geometric parameters for the model are: the width-to-thickness ratio  $W/h$ , and the aspect ratio  $L/W$ . The material properties used for the base model are listed in Table 1.

Table 1: Material properties of graphite/epoxy used in the model of Dano and Hyer [29].

$E_1(GPa)$	$E_2(GPa)$	$G_{12}(GPa)$	$\nu_{12}(GPa)$	$\alpha_1$ ( $10^{-6}/^{\circ}C$ )	$\alpha_2$ ( $10^{-6}/^{\circ}C$ )	$t_{ply} (mm)$
130	10	4.4	0.33	-0.18	30	0.125

Owing to the fact that the unsymmetric composite laminates are subjected to large deformation, and the out-of-plane displacements are many times larger than the laminate thickness, von-Karman strains should be taken into account to capture the plate's geometric nonlinearity. Hence, the midplane strains on the reference surface (midplane) are defined as follows [29]:

$$\epsilon_x^0 = \frac{\partial u^0}{\partial x} + \frac{1}{2} \left( \frac{\partial w^0}{\partial x} \right)^2 \quad (13)$$

$$\epsilon_y^0 = \frac{\partial v^0}{\partial y} + \frac{1}{2} \left( \frac{\partial w^0}{\partial y} \right)^2 \quad (14)$$

$$\gamma_{xy}^0 = \frac{\partial u^0}{\partial y} + \frac{\partial v^0}{\partial x} + \frac{\partial w^0}{\partial x} \frac{\partial w^0}{\partial y} \quad (15)$$

The equilibrium positions of the laminate minimizes the potential energy when it is cooled to the room temperature. The Rayleigh Ritz method is a good approach to approximate the displacement of the laminate and obtain the equilibrium positions. The

model of Dano and Hyer [29] was selected as a base model to validate the accuracy of the approach. The assumed extensional midplane strains field for the 8 ply  $[90_4/0_4]_T$  square laminates are given as follows [29]:

$$\epsilon_x^0 = c_1 + c_2x^2 + c_3y^2 + c_4xy \quad (16)$$

$$\epsilon_y^0 = c_5 + c_6x^2 + c_7y^2 + c_8xy \quad (17)$$

The inplane shear strain can be determined using the strain-displacement relations, and that will be shown shortly. The out-of-plane displacements can be approximated as follows:

$$w^0 = \frac{1}{2}(c_9x^2 + c_{10}y^2 + c_{11}xy) \quad (18)$$

For the base model, a uniform principal curvature are assumed. Therefore, the inplane curvatures are given by:

$$\kappa_x^0 = -\frac{\partial^2 w^0}{\partial x^2} = -c_9 \quad (19)$$

$$\kappa_y^0 = -\frac{\partial^2 w^0}{\partial y^2} = -c_{10} \quad (20)$$

$$\kappa_{xy}^0 = -2\frac{\partial^2 w^0}{\partial x \partial y} = -c_{11} \quad (21)$$

Since the base model is a cross-ply laminate, the twisting curvature can be assumed to be zero,  $\kappa_{xy}^0 = 0$ . Substituting the assumed extensional strains  $\epsilon_x^0$  and  $\epsilon_y^0$  given by Eqs. (16) and (17) and the out-plane-displacement  $w^0$  given by Eq. (18) rearranging and integrating with respect to  $x$  and  $y$  yield to the following in-plane-displacements:

$$u^0(x, y) = c_1x + \frac{1}{3}c_2x^3 + c_3xy^2 - \frac{1}{2}c_4x^2y - \frac{1}{6}c_9^2x^3 - \frac{1}{4}c_9c_{11}x^2y - \frac{1}{8}c_{11}^2xy^2 + h(y) \quad (22)$$

$$v^0(x, y) = c_5y + c_6x^2y + \frac{1}{3}c_7y^3 + \frac{1}{2}c_8xy^2 - \frac{1}{6}c_{10}^2y^3 - \frac{1}{4}c_{10}c_{11}xy^2 - \frac{1}{8}c_{11}^2x^2y + g(x) \quad (23)$$

Where  $h(y)$  and  $g(x)$  are functions to be determined. They were chosen to maintain the pattern of  $u^0(x, y)$  and  $v^0(x, y)$  in odd powers of  $x$  and  $y$ .

$$h(y) = c_{12}y + c_{13}y^3 \quad (24)$$

$$g(x) = c_{12}x + c_{14}x^3 \quad (25)$$

The inplane shear strain can now be determined using Eq. (8c) which yields to the following:

$$\begin{aligned} \gamma_{xy}^0 = & 2c_{12} + \left( c_9c_{10} - \frac{c_{11}^2}{4} + 2c_3 + 2c_6 \right) xy + \left( \frac{1}{2} \left( \frac{c_9c_{11}}{2} + c_4 \right) + c_{14} \right) x^2 + \\ & \left( \frac{1}{2} \left( \frac{c_{10}c_{11}}{2} + c_8 \right) + c_{13} \right) y^2 \end{aligned} \quad (26)$$

**3.1.1. Rayleigh-ritz method.** The equilibrium shapes are obtained by minimizing the potential energy, that leads to 14 nonlinear algebraic equations with 14 unknowns:  $c_1$  to  $c_{14}$ . The total potential energy ( $\Pi$ ) of a composite structure in plane-stress which is subjected to temperature difference can be expressed as a function of the mid-plane strains ( $\epsilon_x^0$ ), curvatures ( $k^0$ ) and laminate stiffness as follows:

$$\Pi = \int_{-\frac{L_x}{2}}^{\frac{L_x}{2}} \int_{-\frac{L_y}{2}}^{\frac{L_y}{2}} \frac{1}{2} \left( \begin{bmatrix} \epsilon^0 \\ k^0 \end{bmatrix}^T \begin{bmatrix} A & B \\ B & D \end{bmatrix} - \begin{bmatrix} \epsilon^0 \\ k^0 \end{bmatrix}^T \begin{bmatrix} N^{th} \\ M^{th} \end{bmatrix} \right) dx dy \quad (27)$$

where the A, B and D are the standard stiffness matrices and are defined as:

$$A_{ij} = \sum_{k=1}^N \bar{Q}_{ij}^k (z_k - z_{k-1}) \quad (28)$$

$$B_{ij} = \frac{1}{2} \sum_{k=1}^N \bar{Q}_{ij}^k (z_k^2 - z_{k-1}^2) \quad (29)$$

$$D_{ij} = \frac{1}{3} \sum_{k=1}^N \bar{Q}_{ij}^k (z_k^3 - z_{k-1}^3) \quad (30)$$

The  $\bar{Q}_{ij}^k$  is the reduced stiffness of the kth layer. The thermal forces and moments per unit length are obtained using the following:

$$N_i^{th} = \sum_{k=1}^{Nl} \sum_{j=1}^N \bar{Q}_{ij}^k \alpha_j^k (z_k - z_{k-1}) \Delta T \quad (31)$$

$$M_i^{th} = \frac{1}{2} \sum_{k=1}^{Nl} \sum_{j=1}^N \bar{Q}_{ij}^k \alpha_j^k (z_k^2 - z_{k-1}^2) \Delta T \quad (32)$$

The stiffness matrix [ABD] and the thermal forces and moments were computed for the cross-ply laminate and substituted into the potential energy ( $\Pi$ ) Eq. (27), along with the assumed polynomial strains and curvature. To obtain the 14 equations, the potential energy should be minimized by taking the derivative of the potential energy with respect to each of the unknown coefficients. Hence, the 14 nonlinear algebraic equations take the form:

$$f_i = \frac{\partial \Pi}{\partial c_i} \quad (33)$$

where  $i = 1, 2, 3, \dots, 14$ . To determine the stability of an equilibrium position, the Jacobian matrix can be computed using the following:

$$J_{ij} = \frac{\partial f_i}{\partial c_j} \quad (34)$$

where  $i, j = 1, 2, 3, \dots, 14$ . if the eigenvalues of Jacobian matrix  $J$  is positive, the equilibrium position is stable.

**3.1.2. The newton raphson method.** The system of nonlinear algebraic equations were solved using the *Newton Raphson* method in MATLAB<sup>®</sup> to obtain the unknown coefficients. For the first iteration  $k = 0$ , the initial guess for the unknown coefficients was selected as  $x_0 = [0, 0, 0, 0, 0, 0, 0, 0, 0, 0, 0, 0, 0, 0] = x_k$  and the Jacobian was computed using Eq. (34). The vector  $x$  was then updated using the following:

$$x_{k+1} = x_k - J(x_k)^{-1} f(x_k) \quad (35)$$

The absolute value of the difference between the vector  $x_k$  and  $x_{k+1}$  is computed, when the error gets below the specified tolerance, the loop stops. Otherwise, the iteration continues. The tolerance used for this analysis is  $\varepsilon = 1 \times 10^{-6}$  and the solution converged at  $iter = 481$ . The equations were also solved using

**Mathematica**® for further validation. The results of the unknown coefficients of the two table shapes are shown in Table 2 and Table 3.

Table 2: Unknown Coefficients obtained for the cross-ply unsymmetric square laminate  $[90_4/0_4]_T$  first shape.

$c_1$	$c_2$	$c_3$	$c_4$	$c_5$	$c_6$	$c_7$
-0.000365	-0.000633	0.0134289	0	-0.0011474	0.0134289	-0.000633
$c_8$	$c_9$	$c_{10}$	$c_{11}$	$c_{12}$	$c_{13}$	$c_{14}$
0	0.0397279	-3.51649	0	0	0	0

Table 3: Unknown Coefficients obtained for the cross-ply unsymmetric square laminate  $[90_4/0_4]_T$  second shape.

$c_1$	$c_2$	$c_3$	$c_4$	$c_5$	$c_6$	$c_7$
-0.0011474	-0.000633	0.0134289	0	-0.000365	0.0134289	-0.000633
$c_8$	$c_9$	$c_{10}$	$c_{11}$	$c_{12}$	$c_{13}$	$c_{14}$
0	3.51649	-0.0397279	0	0	0	0

### 3.2. Square plate - Extended Model

To model a laminate with boundary conditions that are not simply free edges, Mattioni et al. [22] modified the model of Dano and Hyer [29] by relaxing the constant curvature assumption, and this is due to the expected variation in the local curvature when a moment is applied on the edges. In the previous base model, the curvatures along  $x$  and  $y$  directions were constant. For the extended model, a square laminate with side length  $L$  of 180 mm and stacking sequence  $[0_4/90_4]_T$  was used to validate the accuracy of the modified model before considering more complex geometries. The material properties used for the extended model remain unchanged.

The inplane strains are assumed as follows [30]:

$$\epsilon_x^0 = c_1 + c_2x^2 + c_3xy + c_4y^2 \quad (36)$$

$$\epsilon_y^0 = c_5 + c_6x^2 + c_7xy + c_8y^2 \quad (37)$$

Therefore, the in-plane displacements function are then given by:

$$u_{(x,y)}^0 = \int \left( \epsilon_x^0 - \frac{1}{2} \left( \frac{\partial w^0}{\partial x} \right)^2 \right) dx + c_{18}y + c_{19}y^2 \quad (38)$$

$$v_{(x,y)}^0 = \int \left[ \epsilon_y^0 - \frac{1}{2} \left( \frac{\partial w^0}{\partial x} \right)^2 \right] dx + c_{18}x + c_{20}x^2 \quad (39)$$

The shear strain deformation is given by:

$$\gamma_{xy}^0 = \frac{\partial u^0}{\partial y} + \frac{\partial v^0}{\partial x} + \frac{\partial w^0}{\partial x} \frac{\partial w^0}{\partial y} \quad (40)$$

The out-of-plane displacement is assumed as a product of two parabolic functions which yields to the following displacement:

$$w^0(x,y) = c_9 + c_{10}x + c_{11}y + c_{12}x^2 + c_{13}y^2 + c_{14}xy + c_{15}xy^2 + c_{16}x^2y + c_{17}x^2y^2 \quad (41)$$

Solving for the in-plane curvature using Eqs. (19) and (20) presented in the previous section show that they are not constant anymore. Then, plugging the ABD stiffness matrix, thermal load and moments, assumed strains and curvatures into the potential energy Eq. (27) and taking the derivative of each unknown coefficient, yield to a system of nonlinear equations, with 20 unknown coefficients, which can be solved using NSolve command on **Mathematica**<sup>®</sup> or FSolve on **MATLAB**<sup>®</sup>, the system of equations can also be solved using any numerical method, such as Newton Raphson. The results of the unknown coefficients of the two stable shapes are presented in Table 4 and Table 5.

Table 4: Unknown Coefficients obtained for the cross-ply unsymmetric square laminate  $[90_4/0_4]_T$  first shape – Extended.

$c_1$	$c_2$	$c_3$	$c_4$	$c_5$	$c_6$	$c_7$	$c_8$	$c_9$	$c_{10}$
-0.000354	-0.000910	0.007222	0	-0.0016	0.01930	-0.00034	0	0	0
$c_{11}$	$c_{12}$	$c_{13}$	$c_{14}$	$c_{15}$	$c_{16}$	$c_{17}$	$c_{18}$	$c_{19}$	$c_{20}$
0.004439	1.78974	0	0	0	-14.0662	0	0	0	0

Table 5: Unknown Coefficients obtained for the cross-ply unsymmetric square laminate  $[90_4/0_4]_T$  second shape – Extended.

$c_1$	$c_2$	$c_3$	$c_4$	$c_5$	$c_6$	$c_7$	$c_8$	$c_9$	$c_{10}$
-0.0016	-0.00034	0.01930	0	-0.000354	0.007222	-0.00091	0	0	0
$c_{11}$	$c_{12}$	$c_{13}$	$c_{14}$	$c_{15}$	$c_{16}$	$c_{17}$	$c_{18}$	$c_{19}$	$c_{20}$
-1.78974	0.004439	0	0	0	14.0662	0	0	0	0

### 3.3. Compound plate - Extended Model

Mattioni et. al [22] was first to extend the modeling efforts and consider the continuity requirements between a symmetric and an unsymmetric plate. In the second part of his study, a high order model was used to account for piecewise variation. A test structure conducted in his study by joining two square plates with satisfying continuity conditions at the interface. The dimension of the panel is 360 mm  $\times$  180 mm, in which the dimension of each square panel is 180 mm  $\times$  180 mm.

The out-of-plane displacement selected for the two plates is given by:

$$w(x_i, y)^{(i)} = c_9^{(i)} + c_{10}^{(i)} x_i + c_{11}^{(i)} y + c_{12}^{(i)} x_i^2 + c_{13}^{(i)} y^2 + c_{14}^{(i)} x_i y + c_{15}^{(i)} x_i y^2 + c_{16}^{(i)} x_i^2 y + c_{17}^{(i)} x_i^2 y^2 \quad (42)$$

The superscripts (1) and (2) represent the first and second plate of the structure. The strain functions are as follows:

$$\epsilon_x^{0(i)} = c_1^{(i)} + c_2^{(i)} x^2 + c_3^{(i)} xy_i + c_4^{(i)} y_i^2 \quad (43)$$

$$\epsilon_y^{0(i)} = c_5^{(i)} + c_6^{(i)} x^2 + c_7^{(i)} xy_i + c_8^{(i)} y_i^2 \quad (44)$$

The in-plane displacements can be obtained through the following expressions:

$$\epsilon_x^{(i)} = \frac{\partial u^{(i)}}{\partial x} + \frac{1}{2} \left( \frac{\partial w^{(i)}}{\partial x} \right)^2 \quad (45)$$

$$\epsilon_y^{(i)} = \frac{\partial v^{(i)}}{\partial y} + \frac{1}{2} \left( \frac{\partial w^{(i)}}{\partial y} \right)^2 \quad (46)$$

Integrating Equations (45) and (46) and solving for the in-plane displacements yields to 4 additional coefficients.

$$u_{(x,y)}^{(i)} = \int \left( \epsilon_x^0 - \frac{1}{2} \left( \frac{\partial w^0}{\partial x} \right)^2 \right) dx + c_{18}y + c_{19}y^3 \quad (47)$$

$$v_{(x,y)}^{(i)} = \int \left[ \epsilon_y^0 - \frac{1}{2} \left( \frac{\partial w^0}{\partial x} \right)^2 \right] dx + c_{20}x + c_{21}x^3 \quad (48)$$

The expression for  $\gamma_{xy}^{(i)}$  is obtained through

$$\gamma_{xy}^{(i)} = \frac{\partial u^{(i)}}{\partial y} + \frac{\partial v^{(i)}}{\partial x} + \frac{\partial w^{(i)}}{\partial x} \frac{\partial w^{(i)}}{\partial y} \quad (49)$$

The strain  $\epsilon_x^{(i)}(x,y)$  and curvature vectors can be assembled as the following:

$$\epsilon^{(i)} = \begin{Bmatrix} \epsilon_x \\ \epsilon_y \\ \gamma_{xy} \end{Bmatrix}^{(i)} \quad (50)$$

$$\kappa^{(i)} = \begin{Bmatrix} -\frac{\partial^2 w^o}{\partial x^2} \\ \frac{\partial^2 w^o}{\partial y^2} \\ -2\frac{\partial^2 w^o}{\partial x \partial y} \end{Bmatrix}^{(i)} \quad (51)$$

The strain energy of the entire structure can now be calculated using a Rayleigh-Ritz technique similar to that used by Hyer [12]. Each substructure has an individual strain energy that is formulated considering the different stacking sequences, and integration limits, and then the two contributions are combined to obtain the total strain energy.

$$\begin{aligned} \Pi = & \iint_{A_1} \frac{1}{2} \left( \begin{bmatrix} \epsilon^{(1)} \end{bmatrix}^T \begin{bmatrix} A^1 & B^1 \\ B^1 & D^1 \end{bmatrix} \begin{bmatrix} \epsilon^{(1)} \\ \kappa^{(1)} \end{bmatrix} - \begin{bmatrix} \epsilon^{(1)} \end{bmatrix}^T \begin{bmatrix} N^{th} \\ M^{th} \end{bmatrix}^1 \right) dx dy + \\ & \iint_{A_2} \frac{1}{2} \left( \begin{bmatrix} \epsilon^{(2)} \end{bmatrix}^T \begin{bmatrix} A^2 & B^2 \\ B^2 & D^2 \end{bmatrix} \begin{bmatrix} \epsilon^{(2)} \\ \kappa^{(2)} \end{bmatrix} - \begin{bmatrix} \epsilon^{(2)} \end{bmatrix}^T \begin{bmatrix} N^{th} \\ M^{th} \end{bmatrix}^2 \right) dx dy \end{aligned} \quad (51)$$

Where  $\epsilon^{(1)}$  and  $\kappa^{(1)}$  are the mid-plane strains and in-plane curvatures respectively  $A^1, B^1, D^1, A^2, B^2, D^2$ , are the laminate stiffness matrices,  $[A], [B]$  and  $[D]$  are extensional stiffness matrix, bending extension coupling stiffness matrix and bending stiffness matrix respectively.  $N^{th(1)}, N^{th(2)}, M^{th(1)}, M^{th(2)}$  are the thermally induced force and moment vectors respectively. The total strain energy  $\Pi = \Pi(c_{ij}^{(i)})$  is a function of 42 unknown coefficients, Where  $j = 1, 2, 3, \dots, 21$  for  $i = 1, 2$ . The local minima of the total strain energy correspond to the stable shapes of the plate. In order to ensure continuity of displacement across domain A, the following compatibility conditions must hold:

$$w_1\left(\frac{L_1}{2}, y\right) = w_2\left(\frac{-L_2}{2}, y\right) \quad (52)$$

$$\frac{\partial w_1}{\partial x}\left(\frac{L_1}{2}, y\right) = \frac{\partial w_2}{\partial x}\left(\frac{-L_2}{2}, y\right) \quad (53)$$

$$u_1\left(\frac{L_1}{2}, y\right) = u_2\left(\frac{-L_2}{2}, y\right) \quad (54)$$

$$v_1\left(\frac{L_1}{2}, y\right) = v_2\left(\frac{-L_2}{2}, y\right) \quad (55)$$

To simplify the equations and computational time, the following assumptions are made:

- $c_9^{(1)} = 0$  by clamping the geometric center of the symmetric part.
- The experimental results showed that the stable configuration are symmetric with respect to x axis for  $i = 1, 2$ , therefore the following terms can be eliminated  $c_{11}^{(i)}, c_{14}^{(i)}, c_{16}^{(i)}$
- The drilling degree of freedom is eliminated for both plates,  $c_{18} = c_{20}$

The set of nonlinear equations were solved using Fmincon on MATLAB<sup>®</sup>, where the continuity equations were set as constrains for the nonlinear optimization tool.

### 3.4. Hybrid Bistable Symmetric Laminate (HBSL)

In this section, the model developed by Li et al. [25] presented to validate the published work for HBSL with free-free boundary conditions. The model developed by Li et al. [25] was then improved by Mukherjee et al. [10] to account for clamped boundary conditions and to eliminate the debonding issue by replacing the aluminium layers by glass/epoxy bidirectional layers. This section presents the formulations used

for free-free and clamped boundary conditions of the hybrid bistable laminates. Figure 3-1 shows the schematic figure of the modified hybrid bistable laminates (m-HBSL). It is seen that the model consists of three piecewise sections: a central region having a layup  $(90_2/0_2/90_2)_s$  and an outer section of layup  $(90_2/BD_2/90_2)_s$ .

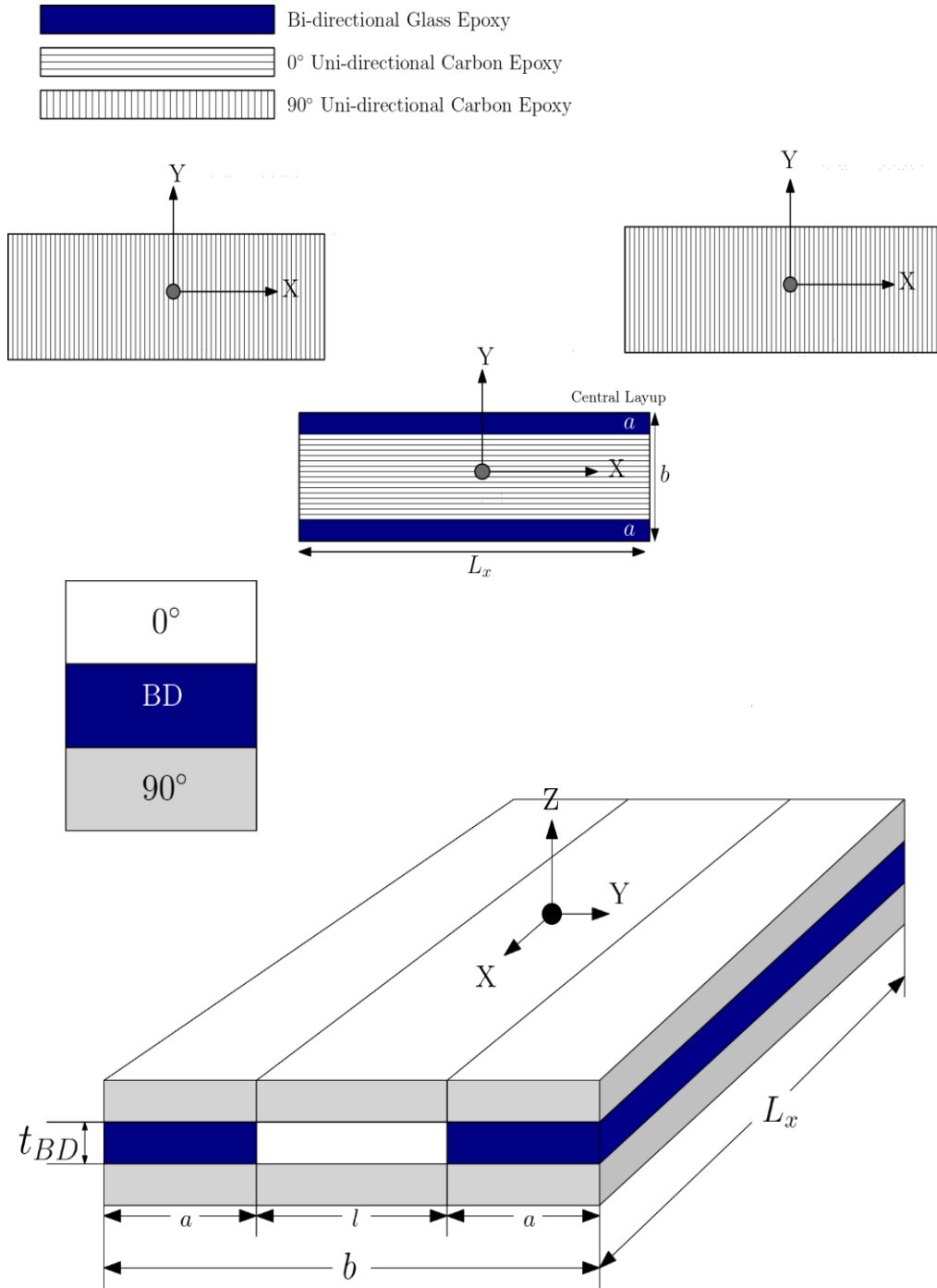


Figure 3-1: Schematic of the stacking sequence of the modified hybrid bistable laminate (m-HBSL) top and isometric view.

The materials used for the HBSL and m-HBSL are shown in Table 6 and Table 7, respectively. Li et al. [25] assumed separate displacement functions for the central section and the two-outer hybrid sections while maintaining continuity requirements between the sections. The dimensions chosen for HBSL in the study of Li et. al [25] and Mukherjee et al. [10] are  $L_x = 280$  mm,  $b = 70$  mm and  $a = 15$  mm.

Table 6: Material properties of carbon/epoxy UD and aluminium layers used in HBSL.

Material	$E_1(GPa)$	$E_2(GPa)$	$G_{12}(GPa)$	$\nu_{12}(GPa)$	$\alpha_1(10^{-6}/^{\circ}C)$	$\alpha_2(10^{-6}/^{\circ}C)$
Carbon/Epoxy UD	137.4	10.07	4.4	0.23	0.37	24.91
Aluminum	79	79	3.0385	0.3	18.8	18.8

Table 7: Material properties of carbon/epoxy UD and Glass/epoxy BD used in m-HBSL.

Material	$E_1(GPa)$	$E_2(GPa)$	$G_{12}(GPa)$	$\nu_{12}(GPa)$	$\alpha_1(10^{-6}/^{\circ}C)$	$\alpha_2(10^{-6}/^{\circ}C)$
Carbon/Epoxy UD	135.4	10	4.4	0.23	0.4	24.5
Glass/Epoxy BD	22.3	22.3	4.75	0.198	19.78	19.78

The out-of-plane displacements and mid-plane strain fields for free-free boundary conditions assumed by Li et al. [25] are given by:

$$w^0 = \begin{cases} \frac{1}{2}(c_1x^2 + c_2y^2) & -\frac{l}{2} < y < \frac{l}{2} \\ \frac{1}{2}c_1x^2 + \frac{1}{2}c_2ly - \frac{1}{8}c_2l^2 & y \geq \frac{l}{2} \\ \frac{1}{2}c_1x^2 - \frac{1}{2}c_2ly - \frac{1}{8}c_2l^2 & y \leq -\frac{l}{2} \end{cases} \quad (56)$$

$$\epsilon_x^0 = \begin{cases} c_3 + c_4y^2 & -\frac{l}{2} < y < \frac{l}{2} \\ c_3 + \frac{1}{4}c_4l^2 + c_7y - \frac{1}{2}c_7l & y \geq \frac{l}{2} \\ c_3 + \frac{1}{4}c_4l^2 - c_7y - \frac{1}{2}c_7l & y \leq -\frac{l}{2} \end{cases} \quad (57)$$

$$\epsilon_y^0 = \begin{cases} c_5 + c_6x^2 & -\frac{l}{2} < y < \frac{l}{2} \\ c_8 + c_9y - \frac{1}{2}c_9l & y \geq \frac{l}{2} \\ c_8 - c_9y - \frac{1}{2}c_9l & y \leq -\frac{l}{2} \end{cases} \quad (58)$$

The in-plane displacements can be obtained through the following expressions:

$$\epsilon_x = \frac{\partial u}{\partial x} + \frac{1}{2} \left( \frac{\partial w}{\partial x} \right)^2 \quad (59)$$

$$\epsilon_y = \frac{\partial v}{\partial y} + \frac{1}{2} \left( \frac{\partial w}{\partial y} \right)^2 \quad (60)$$

Substituting the mid-plane strains and the out-of-plane displacement into Eqs. (59) and (60) yields:

$$u^0 = \begin{cases} c_3 x - \frac{1}{6} c_1^2 x^3 + c_4 x y^2 & -\frac{l}{2} < y < \frac{l}{2} \\ c_3 x - \frac{1}{6} c_1^2 x^3 + c_7 x y - \frac{1}{2} c_7 l x + \frac{1}{4} c_4 l^2 x & y \geq \frac{l}{2} \\ c_3 x - \frac{1}{6} c_1^2 x^3 - c_7 x y - \frac{1}{2} c_7 l x + \frac{1}{4} c_4 l^2 x & y \leq -\frac{l}{2} \end{cases} \quad (61)$$

$$v^0 = \begin{cases} c_5 y + c_6 x^2 y - \frac{1}{6} c_2^2 y^3 & -\frac{l}{2} < y < \frac{l}{2} \\ c_8 y + \frac{1}{2} c_9 y^2 - \frac{1}{2} c_9 l y - \frac{1}{8} c_2^2 l^2 y + \frac{1}{8} c_9 l^2 \\ + \frac{1}{2} c_6 x^2 l + \frac{1}{24} c_2^2 l^3 + \frac{1}{2} c_5 l - \frac{1}{2} c_8 l & y \geq \frac{l}{2} \\ c_8 y + \frac{1}{2} c_9 y^2 - \frac{1}{2} c_9 l y - \frac{1}{8} c_2^2 l^2 y + \frac{1}{8} c_9 l^2 \\ + \frac{1}{2} c_6 x^2 l + \frac{1}{24} c_2^2 l^3 + \frac{1}{2} c_5 l - \frac{1}{2} c_8 l & y \leq -\frac{l}{2} \end{cases} \quad (62)$$

Next, the displacement and strain fields obtained for the clamped boundary conditions are presented. The inner section assumes constant longitudinal curvature, however, due to the clamping of one of the shorter edges, Li et al. [25] assumption of constant transverse curvature was relaxed.

The displacements fields are modified by Mukherjee et al. [10] to account for clamped boundary condition by introducing a new variable  $\bar{x} = x + \frac{Lx}{2}$ , such that at the edge of the laminate  $x = -\frac{Lx}{2}$ ,  $w^0 = 0$ ,  $u^0 = 0$ ,  $v^0 = 0$ .

where  $w^0, u^0, v^0$  are respectively, the lateral and longitudinal deformations,  $\epsilon_x^0$  and  $\epsilon_y^0$  are the normal midplane strains and  $\gamma_{xy}^0$  is the shear midplane strain. The displacement field, modified by Mukherjee et al. [10] to account for the clamped boundary conditions at  $x = 0$ , assumes the lateral displacement as follows:

$$w^0 = \begin{cases} \frac{1}{2}(c_1x^2 + c_2y^2x^2) & -\frac{l}{2} < y < \frac{l}{2} \\ \frac{1}{2}c_1x^2 + \frac{1}{2}c_2lyx^2 - \frac{1}{8}c_2l^2x^2 & y \geq \frac{l}{2} \\ \frac{1}{2}c_1x^2 - \frac{1}{2}c_2lyx^2 - \frac{1}{8}c_2l^2x^2 & y \leq -\frac{l}{2} \end{cases} \quad (63)$$

The midplane normal strains are assumed as follows:

$$\epsilon_x^0 = \begin{cases} \frac{1}{2}x^2c_1^2 + x^2y^2c_1c_2 + \frac{1}{2}x^2y^4c_2^2 + 3x^2c_3 \\ + y^2c_4 + 2xc_5 + 2xy^2c_6 + c_{11} + y^4c_{12} \\ + 3x^2y^2c_{13} & -\frac{l}{2} < y < \frac{l}{2} \\ \frac{1}{2}x^2c_1^2 - \frac{1}{4}l^2x^2c_1c_2 + lx^2yc_1c_2 + \frac{1}{32}l^4x^2c_2^2 \\ - \frac{1}{4}l^3x^2yc_2^2 + \frac{1}{2}l^2x^2y^2c_2^2 + 3x^2c_3 - \frac{1}{4}l^2c_4 \\ + lyc_4 + 2xc_5 - \frac{1}{2}l^2xc_6 + 2lyc_6 + c_{11} \\ - \frac{1}{16}l^4c_{12} + ly^3c_{12} - \frac{3}{4}l^2x^2c_{13} + 3lx^2yc_{13} & -\frac{l}{2} < y < \frac{l}{2} \\ \frac{1}{2}x^2c_1^2 - \frac{1}{4}l^2x^2c_1c_2 - lx^2yc_1c_2 + \frac{1}{32}l^4x^2c_2^2 \\ + \frac{1}{4}l^3x^2yc_2^2 + \frac{1}{2}l^2x^2y^2c_2^2 + 3x^2c_3 - \frac{1}{4}l^2c_4 \\ - lyc_4 + 2xc_5 - \frac{1}{2}l^2xc_6 - 2lyc_6 + c_{11} \\ - \frac{1}{16}l^4c_{12} - ly^3c_{12} - \frac{3}{4}l^2x^2c_{13} - 3lx^2yc_{13} & y \leq -\frac{l}{2} \end{cases} \quad (64)$$

$$\epsilon_y^0 = \begin{cases} \frac{1}{2}x^4y^2c_2^2 + \frac{1}{4}l^2c_7 + 2lyc_7 - c_8 \\ -x^2c_9 + \frac{1}{4}l^2xc_{10} + 2lxy c_{10} & -\frac{l}{2} < y < \frac{l}{2} \\ \frac{1}{8}l^2x^4c_2^2 - \frac{1}{4}l^2c_7 + 2lyc_7 + c_8 \\ +x^2c_9 - \frac{1}{4}l^2xc_{10} + 2lxy c_{10} & y \geq \frac{l}{2} \\ \frac{1}{8}l^2x^4c_2^2 + \frac{1}{4}l^2c_7 + 2lyc_7 - c_8 \\ -x^2c_9 + \frac{1}{4}l^2xc_{10} + 2lxy c_{10} & y \leq -\frac{l}{2} \end{cases} \quad (65)$$

Solving Eqs. (59) and (60) for  $\frac{\partial u^0}{\partial x}$  and  $\frac{\partial v^0}{\partial y}$ , integrating over the domain, and imposing the compatibility conditions at the interfaces, the inplane displacements  $u^0$  and  $v^0$  can be obtained as follows:

$$u^0 = \begin{cases} c_3x^3 + c_4xy^2 + c_5x^2 + c_6x^2y^2 + c_{11}x \\ +c_{12}xy^4 + c_{13}x^3y^2 & -\frac{l}{2} < y < \frac{l}{2} \\ c_3x^3 + c_4xyl - \frac{1}{4}c_4xl^2 + c_5x^2 + c_6x^2yl - \frac{1}{4}c_6x^2l^2 \\ +c_{11}x + c_{12}xy^3l - \frac{1}{16}c_{12}xl^4 + c_{13}x^3yl - \frac{1}{4}c_{13}x^3l^2 & y \geq \frac{l}{2} \\ c_3x^3 - c_4xyl - \frac{1}{4}c_4xl^2 + c_5x^2 - c_6x^2yl - \frac{1}{4}c_6x^2l^2 \\ +c_{11}x - c_{12}xy^3l - \frac{1}{16}c_{12}xl^4 - c_{13}x^3yl - \frac{1}{4}c_{13}x^3l^2 & y \leq -\frac{l}{2} \end{cases} \quad (66)$$

$$v^0 = \begin{cases} c_7y^3 + c_8y + c_9x^2y + c_{10}xy^3 & -\frac{l}{2} < y < \frac{l}{2} \\ c_7y^2l - \frac{1}{4}c_7yl^2 + c_8y + c_9x^2y \\ +c_{10}xy^2l - \frac{1}{4}c_{10}xy^3 & y \geq \frac{l}{2} \\ c_7y^2l + \frac{1}{4}c_7yl^2 - c_8y - c_9x^2y \\ +c_{10}xy^2l + \frac{1}{4}c_{10}xy^3 & y \leq -\frac{l}{2} \end{cases} \quad (67)$$

The curvatures  $\kappa_x^0$  and  $\kappa_y^0$  can be obtained as follows:

$$\kappa_x^0 = -\frac{\partial^2 w^0}{\partial x^2} = \begin{cases} -c_1 - y^2 c_2 & -\frac{l}{2} < y < \frac{l}{2} \\ -c_1 + \frac{1}{4} l^2 c_2 + l y c_2 & y \geq \frac{l}{2} \\ -c_1 + \frac{1}{4} l^2 c_2 + l y c_2 & y \leq -\frac{l}{2} \end{cases} \quad (68)$$

$$\kappa_y^0 = -\frac{\partial^2 w^0}{\partial y^2} = \begin{cases} -x^2 c_2 & -\frac{l}{2} < y < \frac{l}{2} \\ 0 & y \geq \frac{l}{2} \\ 0 & y \leq -\frac{l}{2} \end{cases} \quad (69)$$

This piecewise displacement field is selected such that the continuity or compatibility conditions of  $u^0$ ,  $v^0$ ,  $w^0$ ,  $\frac{\partial w^0}{\partial x}$  and  $\frac{\partial w^0}{\partial y}$  are satisfied at the interfaces along the laminate's width, i.e., at  $y = -\frac{l}{2}$  and  $y = \frac{l}{2}$ . In addition, the displacement field satisfies the following geometric boundary conditions at the clamped end:  $w^0 = 0$ ,  $\frac{\partial w^0}{\partial x} = 0$ ,  $\frac{\partial w^0}{\partial y} = 0$ ,  $u^0 = 0$ . One may also notice that the assumption introduced by Li et al. [25] of the constant inplane curvatures  $\kappa_x^0$  and  $\kappa_y^0$  is relaxed, as it is evident from Eqs. (68) and (69). However, it can be observed that the condition  $v^0 = 0$  at the clamped edge is only satisfied on an averaged sense. The equilibrium positions of the laminate are calculated using the Rayleigh Ritz method via the minimization of the total potential energy to find the constant  $c_i$ . The minimization of the potential energy leads to thirteen nonlinear algebraic equations for thirteen unknowns:  $c_1$  to  $c_{13}$ . The total potential energy of the laminate is defined as:

$$\begin{aligned} \Pi = & 2 \int_0^{L_x} \int_0^{\frac{l}{2}} \int_{-\frac{h}{2}}^{\frac{h}{2}} \frac{1}{2} \left( [\epsilon^0]^T \begin{bmatrix} A & A \\ B & D \end{bmatrix} [\kappa^0] - [\epsilon^0]^T \begin{bmatrix} N^{th} \\ M^{th} \end{bmatrix} \right) dz dy dx \\ & + 2 \int_0^{L_x} \int_{\frac{l}{2}}^l \int_{-\frac{h}{2}}^{\frac{h}{2}} \frac{1}{2} \left( [\epsilon^0]^T \begin{bmatrix} A & A \\ B & D \end{bmatrix} [\kappa^0] - [\epsilon^0]^T \begin{bmatrix} N^{th} \\ M^{th} \end{bmatrix} \right) dz dy dx \end{aligned} \quad (70)$$

where the  $A, B$  and  $D$  are the standard longitudinal, coupling, and bending stiffness matrices of the laminate defined as:

$$A_{ij} = \sum_{k=1}^N \bar{Q}_{ij}^k (z_k - z_{k-1}) \quad (71)$$

$$B_{ij} = \frac{1}{2} \sum_{k=1}^N \bar{Q}_{ij}^k (z_k^2 - z_{k-1}^2) \quad (72)$$

$$D_{ij} = \frac{1}{3} \sum_{k=1}^N \bar{Q}_{ij}^k (z_k^3 - z_{k-1}^3) \quad (73)$$

The  $\bar{Q}_{ij}^k$  are the reduced transformed stiffnesses of the  $k^{\text{th}}$  layer. The thermal force and moment stress resultants are given by

$$N_i^{th} = \sum_{k=1}^N \sum_{j=1}^N \bar{Q}_{ij}^k \alpha_j^k (z_k - z_{k-1}) \Delta T \quad (74)$$

$$M_i^{th} = \frac{1}{2} \sum_{k=1}^N \sum_{j=1}^N \bar{Q}_{ij}^k \alpha_j^k (z_k^2 - z_{k-1}^2) \Delta T \quad (75)$$

The total potential energy is minimized by setting its first variation with respect to every unknown constant equal to zero. This yields a system of nonlinear algebraic equations for the constants  $c_i$  as follows:

$$f_i = \frac{\partial \Pi}{\partial c_i}, \quad (76)$$

where  $i = 1, 2, \dots, 13$ . The equations were solved using NSolve command on Mathematica<sup>®</sup>.

## Chapter 4. Methodology

Prior to starting with the proposed model and objectives of this thesis, it is important to validate some of the results seen in the literature. The base model of Danno and Hyer [29] was validated using the methodology and formulation explained in the previous chapter which includes the modification of the classical lamination theory model by considering the nonlinear terms and large deformation, named as the base model. The extended model of Mattioni et al. [22] which includes the variation of the curvature across the domain by including a fourth order displacement function as a basis to extend the model was also validated. Furthermore, the results obtained using the proposed model of Li et al. [25] for the the hybrid bistable laminates are also shown in this chapter.

### 4.1. Base Model

When a composite laminate is unsymmetric, the mismatch of the thermal expansion coefficient between plies results in thermally induced strain. . Therefore, the laminate develops a curved deformation when it is cooled from the curing temperature to the room temperature. Depending on the geometric parameters of the laminate, the thermal strain induced can lead to the development of the two stable equilibrium shapes, known as bistability. The variation of the principal curvature in x-axis,  $\kappa_x$ , and principal curvature in y-axis,  $\kappa_y$ , are plotted against the width-to-thickness ratio for a 8-ply  $[90_4/0_4]_T$  graphite epoxy laminate base model. The equilibrium position depends on the length to thickness ratio as the laminate is cooled down from the curing temperature to the room temperature. The results obtained show that below a certain width-to-thickness ratio, the only stable equilibrium shape is the saddle shape, as seen in Figure 4-1 at point **A**. On the other hand, the laminate's bistability is recognized at a critical width-to-thickness ratio of 100, this point refers to the bifurcation point **B** where the laminate exhibits two stable equilibrium cylindrical shapes point **D** and **C** and the saddle shape becomes the unstable equilibrium shape. This compares well with existing literature, as the bending and twisting moments that are generated within the laminate structure, resulting in out-of-plane displacements causing residual stresses.

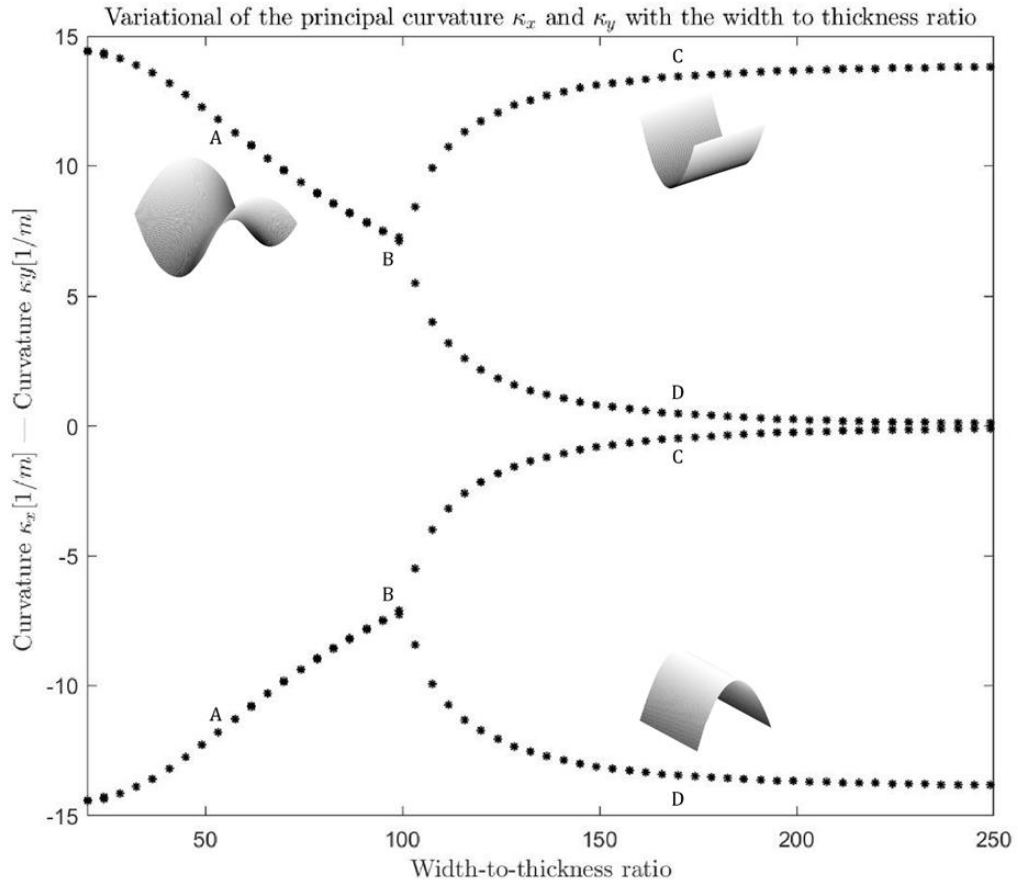


Figure 4-1: Variation of the principal curvature  $\kappa_x$  and  $\kappa_y$  with the width-to-thickness ratio for 8-ply  $[90_4/0_4]_T$ .

At room temperature, these residual stresses result in cylindrical equilibrium positions. The saddle equilibrium shape of an 8-ply  $[90_4/0_4]_T$  square laminate of a width of 18 mm and width-to-thickness ratio of 75 is presented in Figure 4-2a. As mentioned, the saddle shape becomes unstable once the laminate exhibits the bistability at a certain width-to-thickness ratio [100 mm]. Below this ratio, the only stable equilibrium position is the saddle shape, where  $\kappa_x$  and  $\kappa_y$  are equal in magnitude and opposite in out-of-plane directions. The first and the second cylindrical equilibrium shapes obtained are shown in Figures 4-2b. and 4-2c. Therefore, the width-to-thickness ratio at the bifurcation point **B** is one of the key parameters of the bistable behaviour of the laminate.

#### 4.2. Square plate - Extended Model

The analytical models are usually based on the hypothesis of constant and uniform curvatures, as in the base model, Danno and Hyer [29] which could only take into account free-free boundary conditions. To consider more complex geometries and

attach two or more laminates together, where the boundary condition is not free-free, the hypothesis of constant curvature must be modified using the model of Mattioni et al. [22]. The results were obtained using the methodology and formulation of the extended model detailed in the section 3.2 in Chapter 3. When considering complex geometries, where a moment is applied to an edge, variation in the local curvature is expected. Hence, the curvature must vary across the domain, Therefore, a fourth-order displacement was selected as a basis to extend the model.

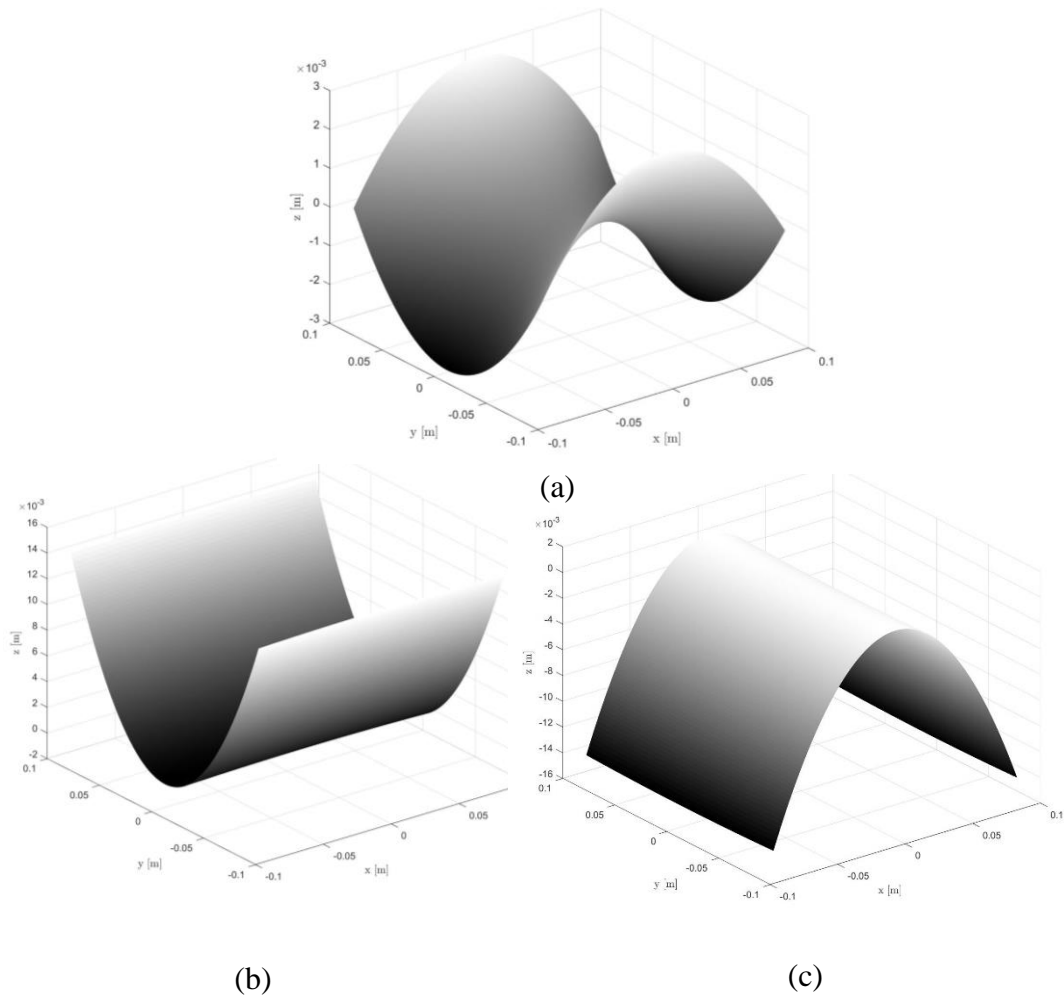


Figure 4-2: The obtained configurations of 8-ply  $[90_4/0_4]_T$  square laminate using base model. (a) Saddle unstable shape (b) First stable cylindrical shape (c) Second stable cylindrical shape.

Table 8 shows the values of the principal curvatures  $\kappa_x$  and  $\kappa_y$  for the two equilibrium configurations the base and extended models. Figure 4-3 shows a comparison of the curvature values across the domain using two analytical models, the base and extended model. The results obtained show good agreement with the literature, where the higher order model predicts quadratic curvature, whereas the base

model has a constant curvature value across the domain. The equilibrium shapes of the extended model are shown in Figure 4-4. In comparison with the shapes obtained in Figure 4-2 it is clearly seen that the vertical displacement has slightly increased. However, both models have quite similar displacements all over the plate. The huge difference can be seen within the region close to the edges, where the curvature was varied. The results obtained with the model of Danno and Hyer [29] shows an almost straight edge. On the other hand, the edges of the extended model computed with higher order model has a slight parabolic variation on the edges. As stated earlier, continuation of this work include joining the unsymmetric laminate 4-ply  $[90_2/0_2]_T$  to the 4-ply  $[0/90]_S$  symmetric laminate taking into account the interaction between the symmetric and unsymmetric part of the plate by satisfying certain matching condition. Validating the model of the compound plate will help us understand the behaviour of such structures when considering different boundary conditions and complex geometries.

Table 8: A comparison between the curvature of the square plate obtained using the two models.

Configuration	Base Model $m^{-1}$	Extended Model $m^{-1}$
<i>First Configuration</i>		
$\kappa_x$	0.0397279	$-0.00887939 + 28.1324 y^2$
$\kappa_y$	-3.51649	$-3.57948 + 28.1324 x^2$
<i>Second Configuration</i>		
$\kappa_x$	3.51649	$3.57948 - 28.1324 x^2$
$\kappa_y$	-0.0397279	$0.00887939 - 28.1324 y^2$

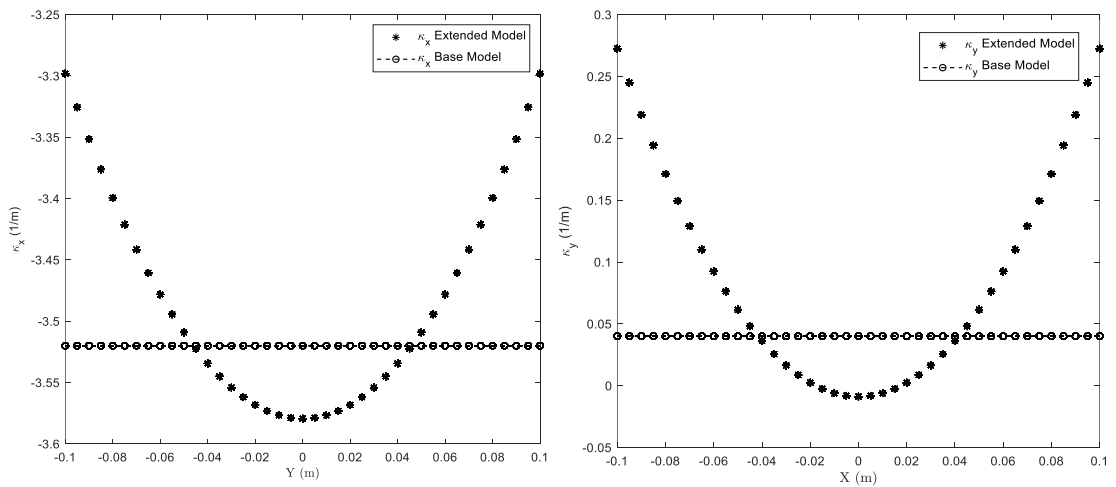


Figure 4-3: Principal curvatures comparison of the base and extended model.

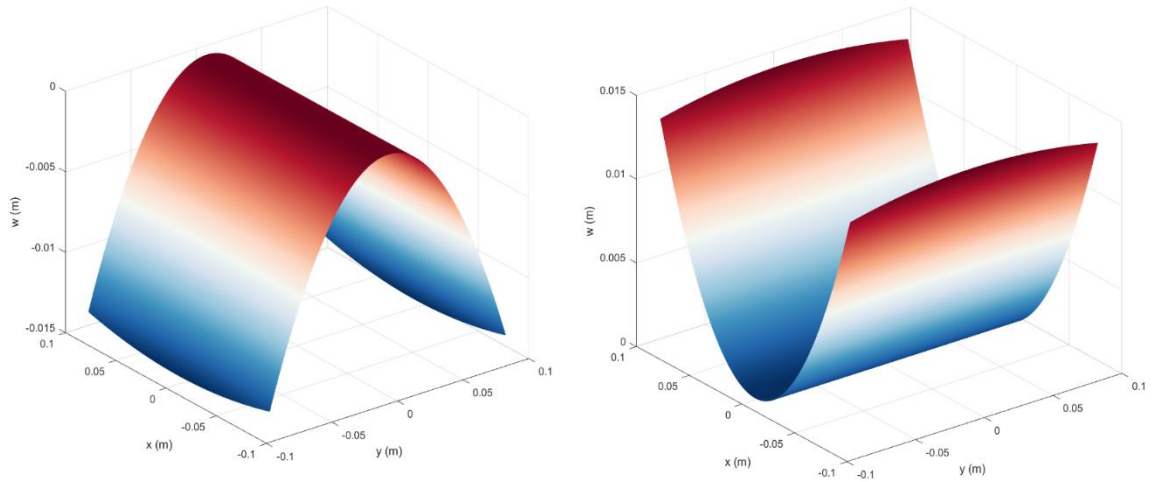


Figure 4-4: The unstable and stable equilibrium shapes using the extended model (a) The first stable equilibrium configuration (b) The second stable equilibrium configuration.

### 4.3. Compound plate - Extended Model

In this section, the unsymmetric square 4-ply laminate  $[90_2/0_2]_T$  is joined with the symmetric square 4-ply laminate  $[0/90]_S$  considering the continuity requirements at the intersection of the two plates. The results presented in this section are obtained using the analytical model proposed by Mattioni et al. [22] for the compound plate. The formulation is detailed in Chapter 3 section 3.3. The equilibrium shapes obtained using the analytical model are validated against the experiment and ABAQUS FE results generated in the literature as Figure 4-5 shows and a good agreement was achieved. The equilibrium shapes of the compound plate are named as “flat configuration” and “curled configuration”, therefore, the curvature values of the two shapes are not the same. The compound plate was also simulated using the commercial software ABAQUS<sup>®</sup> with “static, stabilize” option which makes use of an automatic stabilization based on the addition of viscous forces to the global equilibrium equation. A uniform initial curing temperature of 140°C and a final temperature of 0°C was applied to all the nodes while restricting all degrees of freedom at the center of the plate to prevent rigid body motions. After the cooling down process, the laminate develops internal stresses causing the laminate to settle to the first equilibrium stable shape seen in Figure 4-6a. For the snapthrough analysis, an additional two steps are required and the following boundary and loading conditions are applied:

1. Prevent rotational degrees of freedom on the four corners of the plate, i.e.,  $U_{R1}, U_{R2}, U_{R3}$ .

2. The geometric center of the unsymmetric part of the shell is constrained using “encastre” option.
3. A concentrated force along the vertical axis, is applied to the four corners of the laminate.
4. The applied load is then removed, and the plate settles to the second equilibrium shape seen in Figure 4-6b.

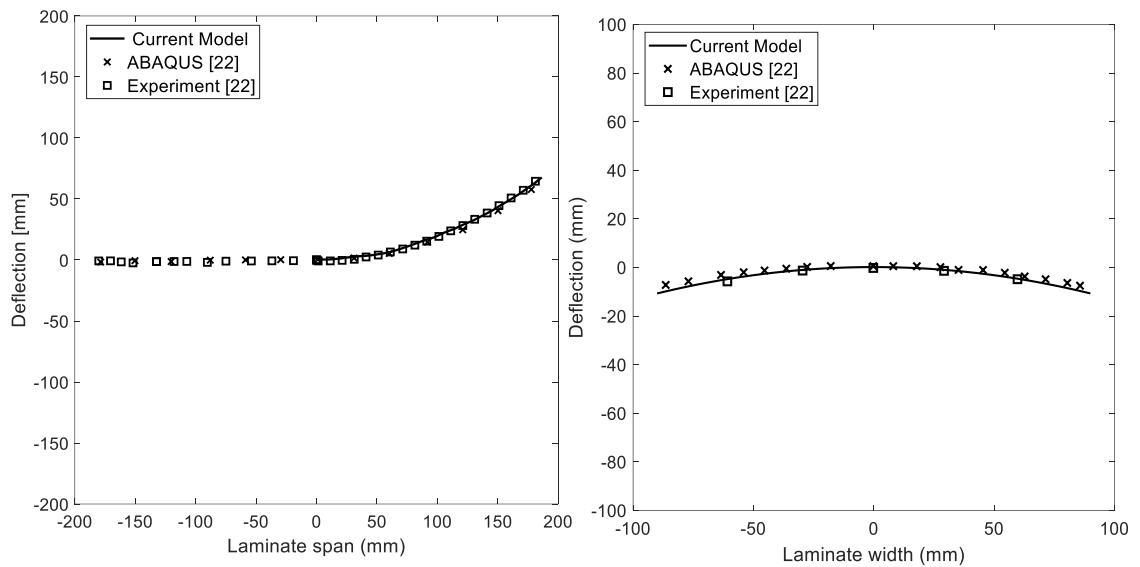
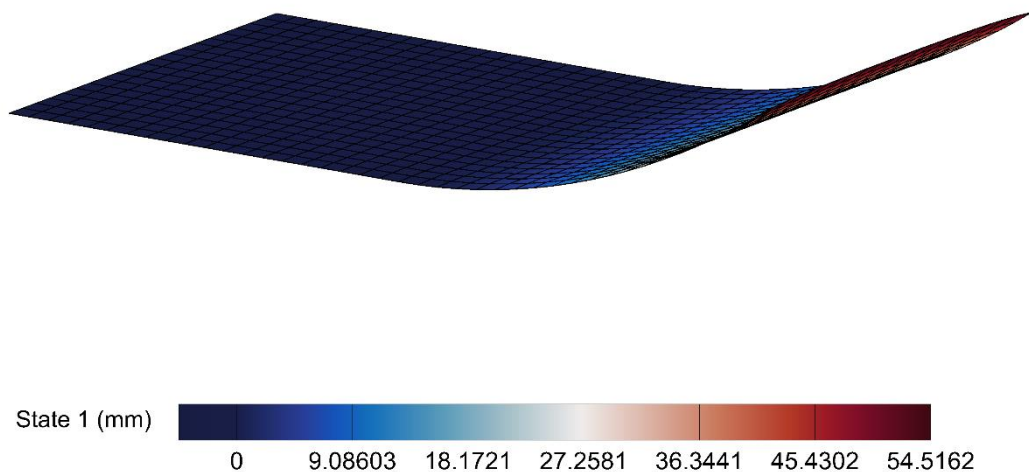
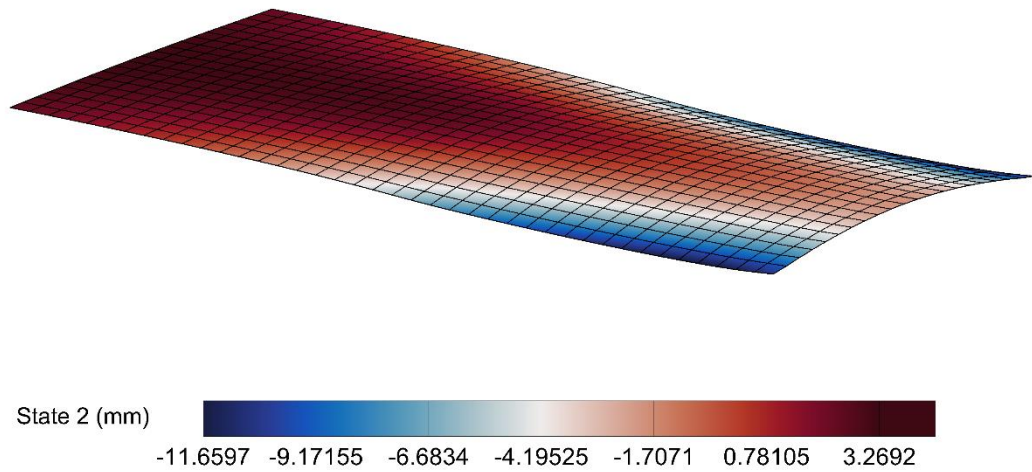


Figure 4-5: The stable equilibrium shapes of the compound plate using analytical model with ABAQUS FE and experiment of Mattioni et al. [22] (a) longitudinal cross section of the curled configuration (b) Unsymmetric cross section of the flat configuration.



(a)



(b)

Figure 4-6: The stable equilibrium shapes of the compound plate obtained using ABAQUS FE (a) Curled configuration (b) Flat configuration.

#### 4.4. Hybrid Bistable Symmetric Laminates (HBSL)

In this section, the analytical model of the hybrid bistable symmetric laminates proposed by Li et al. [25] is verified with free-free boundary condition, followed by the modified model proposed Mukherjee et al. [10] to account for clamped boundary conditions of the model. The results were also validated against FEA using the commercial *ABAQUS*<sup>®</sup> software

**4.4.1. Analytical analysis of the hbsl.** To find the equilibrium shapes of the hybrid bistable symmetric laminates HBSL with the layup laminate  $(90_2/Al_2/90_2)_T \cup (90_2/0_2/90_2)_T \cup (90_2/Al_2/90_2)_T$  for free-free boundary condition, the assumed displacement and strain fields proposed by Li et al. [25] and shown in Chapter 3, section 3.4 are used with a uniform temperature field of  $\Delta T = 120^\circ c$ . Substituting the displacement fields into the total potential energy field and minimize it, yields to a system of nine algebraic equations. clamped model has thirteen nonlinear algebraic equations. Figure 4-7 shows the stable equilibrium of HBSL with free-free and clamped boundary condition at the centerline.

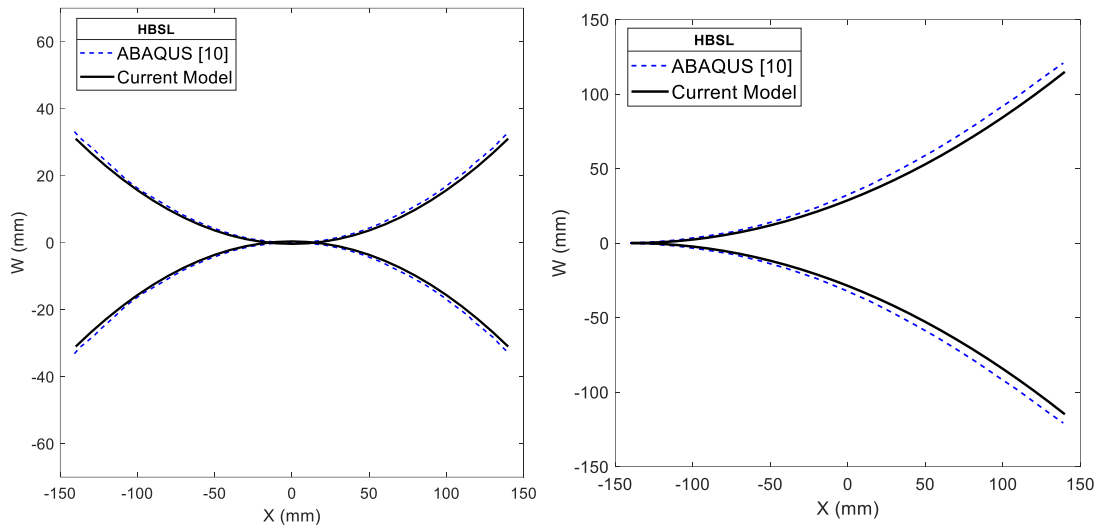


Figure 4-7: Bistable shapes of clamped HBSL using the current model and the ABAQUS results of Mukherjee et. al [10] for free-free and clamped boundary conditions.

#### 4.4.2. Finite element analysis of the hbsl.

**4.4.2.1 Free-free boundary conditions.** The model was simulated using ABAQUS. For the curing process, a temperature field of  $150^{\circ}c$  was applied to the entire laminate, while restricting any motion in  $x, y, z$  at the center of the laminate. In the next step, the laminate was allowed to cool-down to a room temperature field of  $20^{\circ}c$ .

The change in temperature causes the laminate to develop internal thermal stresses, however, as a result of the symmetry, the structure settles to an unstable flat configuration. The stable states are obtained by applying a small load at the four corners of the laminate along the  $z$  direction, while fixing all degrees of freedom at the central node of the laminate. The load applied on the laminate is removed to settle to the first stable configuration. The stable shapes obtained using FEA are shown in Figure 4-8.

Figures 4-9 and 4-10 show the contour maps of the transverse and longitudinal bending curvature, respectively. It is seen that the curvature magnitudes are identical for both configurations, but the curvature signs are opposite. Figure 4-9 illustrates the contour maps of the transverse bending curvature,  $\kappa_y$ . In the region with aluminum ply, the curvature  $\kappa_y$  is very small, the curvature variation remains almost the same along the length direction, except the regions near the shorter edges. As can be seen from the contour maps in Figure 4-10, most of the regions have a constant longitudinal curvature. However, due to the boundary effect, the longitudinal curvature  $\kappa_x$  decreases in the region close to the short edges. From the FEA results, it is shown that for a multi-

sectioned laminate, the characteristic for each section is different. i.e, out-of-plane displacement and mid-plane strains, therefore, a piecewise continuous displacement functions was required to model a multisectioned laminate. In the central region, it is assumed that the longitudinal and transverse curvature are constant, and the boundary effects close to the short edges are neglected.

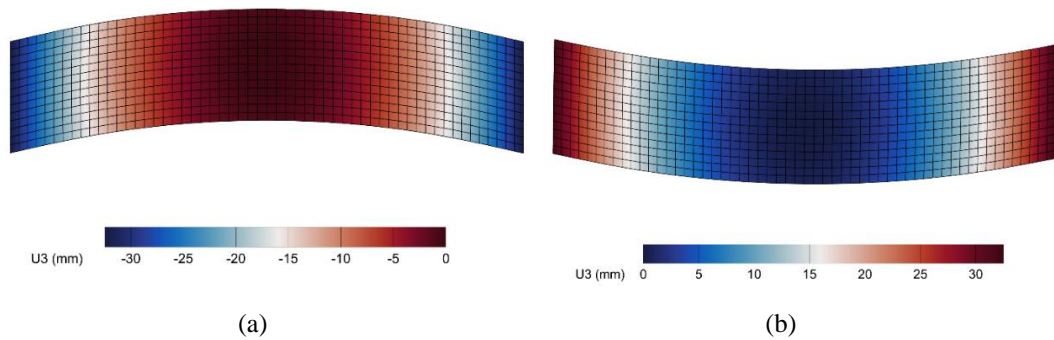


Figure 4-8: The equilibrium shapes of HBSL with free-free boundary conditions using FEA (a) First stable shape (b) Second stable shape

The longitudinal curvature of the aluminum hybrid region is identical to the central region, However, the transverse curvature of the hybrid region is very small and it is assumed to be zero. Variations in curvature along the laminate show how piecewise functions were developed. A comparison of the BHSL curvature using analytical and FEA for free-free boundary condition is shown in Table 9.

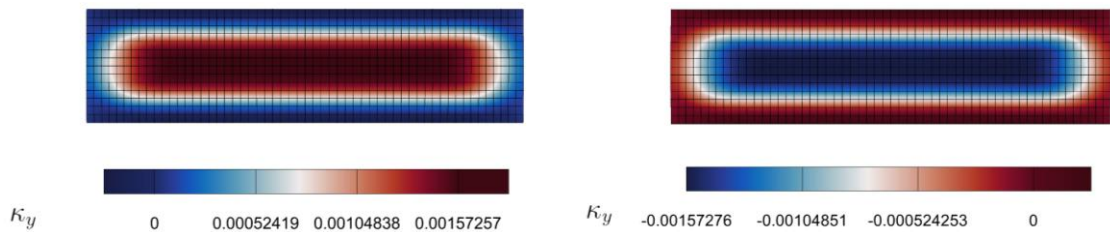


Figure 4-9: Contour maps of transverse bending curvature  $\kappa_y$  (free-free boundary conditions)

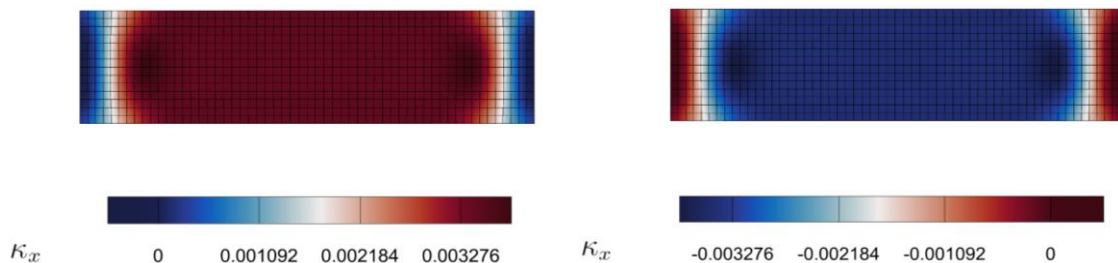


Figure 4-10: Contour maps of longitudinal bending curvature  $\kappa_x$  (free-free boundary conditions)

Table 9: Comparison of longitudinal curvatures of BHSLs given by FEA and analytical model with free-free boundary conditions.

	Analytical		FEA	
	Current	Literature [10]	Current	Literature [10]
<i>Longitudinal Curvature <math>\kappa_x</math> <math>m^{-1}</math></i>	3.3135	3.293	3.276	3.274

**4.4.2.2 Clamped boundary conditions.** The curing process of this model is similar to the free-free boundary condition, in the subsequent step, one of the shorter edges is clamped using ‘encastre’ boundary condition on ABAQUS. Selecting this option allows to restrict all degrees of freedom in  $x, y, z$ . To obtain the equilibrium shapes of the laminate, a concentrated load was applied at the edge of the free shorter edge along the  $z$  direction. In the next step, the load is removed to allow the laminate settle to one of the equilibrium shapes. A more detailed analysis of the FEA will be discussed in the coming chapter. Figure 4-11 shows the equilibrium shapes under clamped boundary conditions.

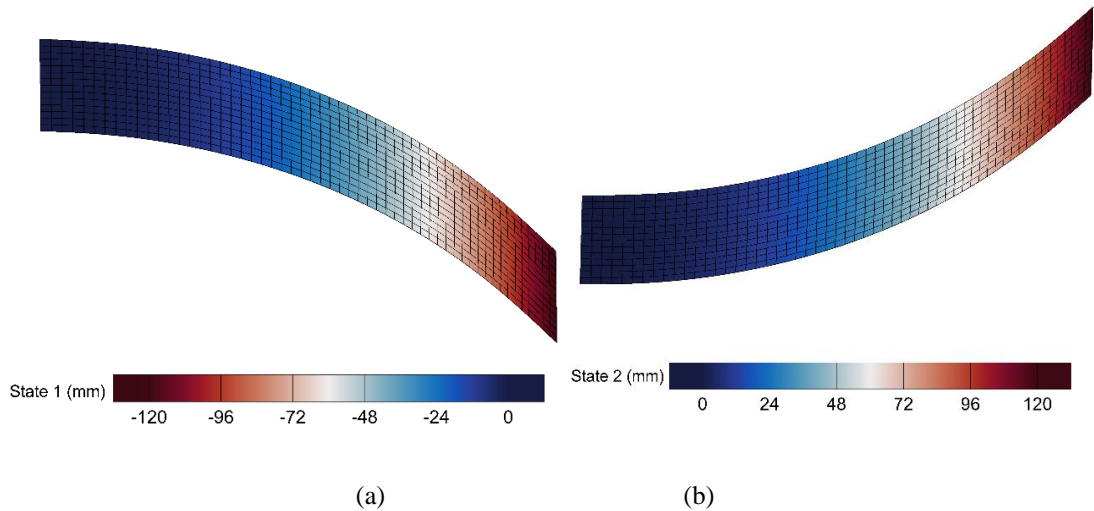


Figure 4-11: The equilibrium shapes of HBSL with clamped boundary conditions (a) First stable shape (b) Second stable shape

The transverse and longitudinal curvatures of the HBSL with clamped boundary condition are shown in Figures 4-12 and 4-13 respectively, for the two stable shapes. For the longitudinal curvature  $\kappa_x$ , the central region has a constant curvature, except near the shorter, and this is due to the boundary condition effect, as discussed in the previous section. The contour map variation of the longitudinal curvature of the clamped

boundary condition is identical to the free-free boundary condition, the central region has a small  $\kappa_y$  curvature and hybrid region has almost zero transverse curvature.

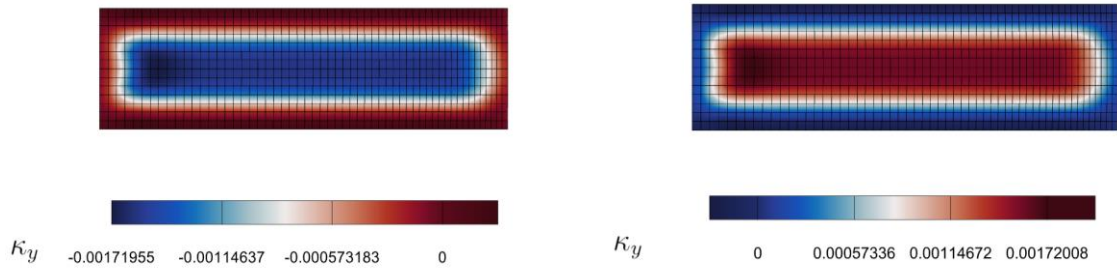


Figure 4-12: Contour maps of transverse bending curvature  $\kappa_y$  (clamped boundary conditions)

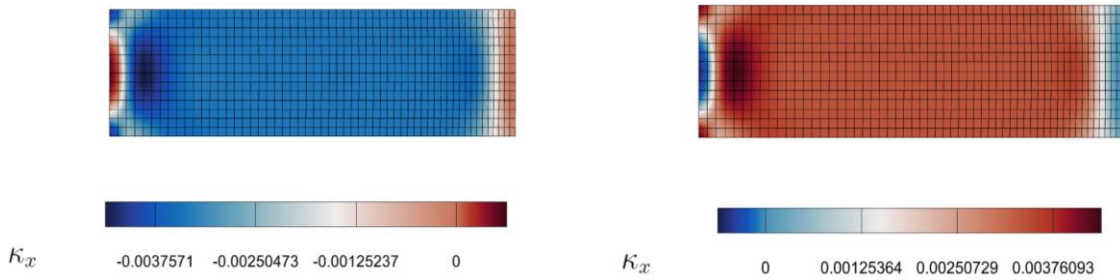


Figure 4-13: Contour maps of longitudinal bending curvature  $\kappa_x$  (clamped boundary conditions)

A comparison of the longitudinal curvature obtained using the analytical scheme and FEA with clamped boundary condition is shown in Table 10. Comparing the results to the literature shows that they are in good agreement, which is helpful in establishing the project's objective

Table 10: Comparison of the tip displacement of clamped HBSL using the analytical model and ABAQUS FE.

Configuration	Tip Displacement (mm)		
	Model	ABAQUS [10]	Error (%)
HBSL	115	120.7	4.72

#### 4.5. Modified Hybrid Bistable Symmetric Laminates (m-HBSL)

It has been identified that metal epoxy composite laminates proposed by Li et al. [25] tend to debond at the metal epoxy interface. Thus, the HBSL mode was improved by Mukherjee et al. [10] to eliminate the slippage and debonding issues that occur at the metal and the carbon/epoxy interface of the original layup by replacing the aluminum ply with bidirectional glass/epoxy prepregs to ensure the effect of slippage is minimal. The bistable shapes of the m-HBSL using the analytical model in

comparison with the ABAQUS FE and experiment results obtained from Mukherjee et al. [10] are shown in Figure 4-14 and Table 11.

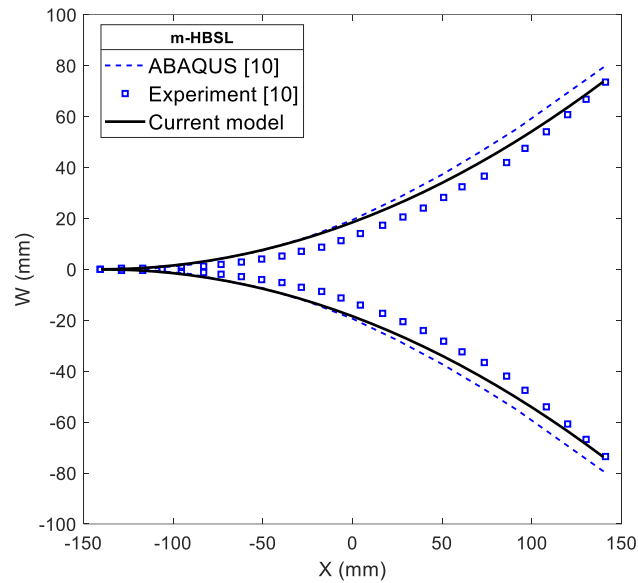


Figure 4-14: Bistable shapes of m-HBSL using the current model, ABAQUS and experimental results of [10].

Table 11: Comparison of the tip displacement of clamped m-HBSL using the analytical model, ABAQUS FE and experiment.

Configuration	Tip Displacement (mm)			Error (%)
	Model	ABAQUS [10]	Experiment [10]	
m-HBSL	73.7	80.3	73.3	8.21,0.545

## Chapter 5. Parametric Study on M-HBSL

In this chapter, a parametric analysis on the m-HBSL plate attached to a rigid wall is presented. The dimensions of the laminate were changed to represent a non-dimensionalized parameters. For a baseline configuration, the dimensions selected are  $b = 100$  mm,  $L_x = 300$  mm and the thickness of the laminate is  $t = 0.75$  mm where the thickness of each layer is  $t_{layer} = 0.125$  mm. The results obtained for five different sets of numerical and analytical studies aimed to understand the effects of varying the bi-directional glass/epoxy layers width, thickness, location on the snapthrough characteristics.

### 5.1. Effect of varying BD Glass Epoxy Layer Width

In this section, the bidirectional ply width,  $2a$ , is varied from 0 to 1. A schematic figure of the laminate's cross section showing the varied parameter  $a$  is shown in Figure 5-1. When  $2a = 0$ , the laminate's core is free of the bidirectional layer and is purely filled with the unidirectional carbon-epoxy prepregs. On the other hand, when  $2a = 1$ , the core is purely filled with the bidirectional plies.

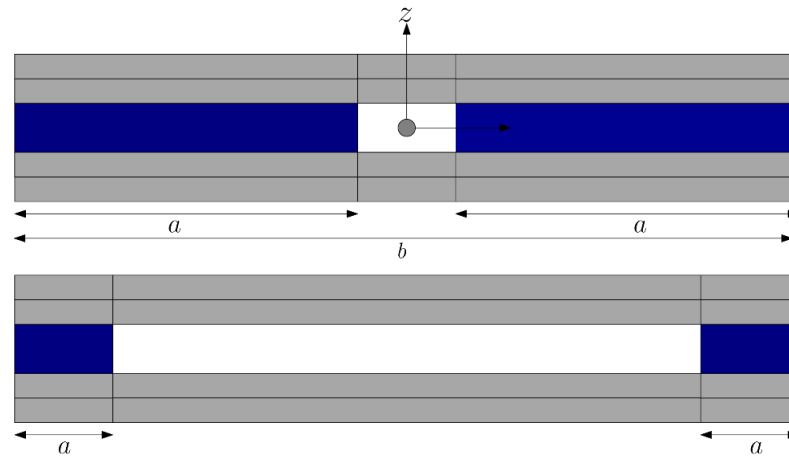


Figure 5-1: A schematic of the laminate's cross section showing the bidirectional layer width.

Table 7 shows that the bidirectional layer has thermal expansion coefficients that are similar to aluminum. However, their modulus of elasticity is small compared with that of the carbon-epoxy prepreg in the fibers' direction, i.e.  $E_1$ . Namely the carbon-epoxy prepreg's modulus of elasticity is about six times that of the bidirectional ply. The results show that the ratio  $2a/b$  qualitatively and quantitatively affects the

laminates' bistability and the initial curvature. In particular, a nominal value of  $2a/b$  around 0.5 yields the maximum initial deflection of the bistable shapes. Away from this value in both sides, it is found out that the initial curvature decreases. Moreover, for very large or very small ratios of  $2a/b$ , the laminate's bistability disappears. Figure 5-2 presents the bistable equilibrium positions for the modified hybrid bistable symmetric laminate (m-HBSL) for  $2a/b = 0.2, 0.3, 0.4$  and  $0.5$  using the analytical model and the ABAQUS FE. There is a good agreement between the model and the FE results for  $2a/b = 0.4$  and  $0.5$ .

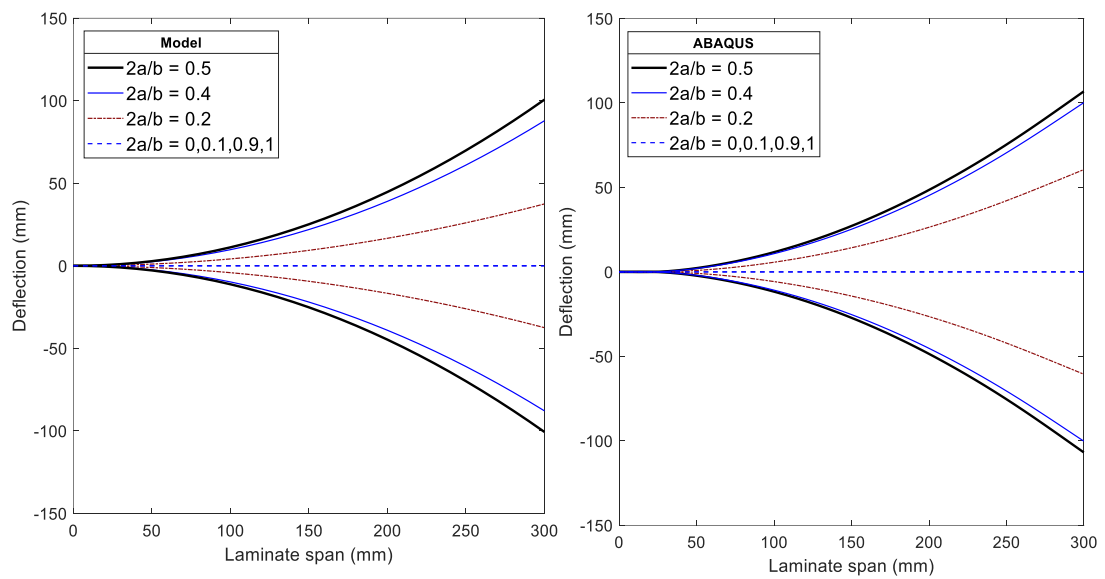


Figure 5-2: The equilibrium shapes of clamped m-HBSL with varying bidirectional ply width using analytical model and ABAQUS.

The results show that the bidirectional glass epoxy plies' width is crucial in identifying the bistability of the m-HBSL. It is interesting to notice that the bistability disappears if the laminate's core is made of almost pure unidirectional prepregs or bidirectional plies. The justification is that the bistability of symmetric laminates was initiated in the first place by Li et al. [25] using a hybrid laminate where the core has a considerable content of both the unidirectional prepreg and the hybrid material whether it is aluminum in [25] or bidirectional glass epoxy in [10]. A concentrated lateral load is applied on the laminate's tip at its center. As the load increases, the laminate deflects until it snaps to the other stable position when the load reaches its threshold. The snapthrough is simulated in *ABAQUS*<sup>®</sup> using the 'static stabilize' procedure. The left of Figure 5-3 presents the load-deflection curves for the loading and unloading

schemes. It also shows the snapthrough and snapback loads for a variety of bidirectional width ratio  $2a/b$ . The variation of the longitudinal curvature  $\kappa_x$  with the applied load for  $2a/b = 0.2, 0.3, 0.4,$  and  $0.5$  is shown at right of Figure 5-3. As the applied load increases, the curvature decreases until the plate settles to the other stable position. Table 12 presents the numerical values of the tip deflection and the snapthrough loads for varying bidirectional width using the model and ABAQUS.

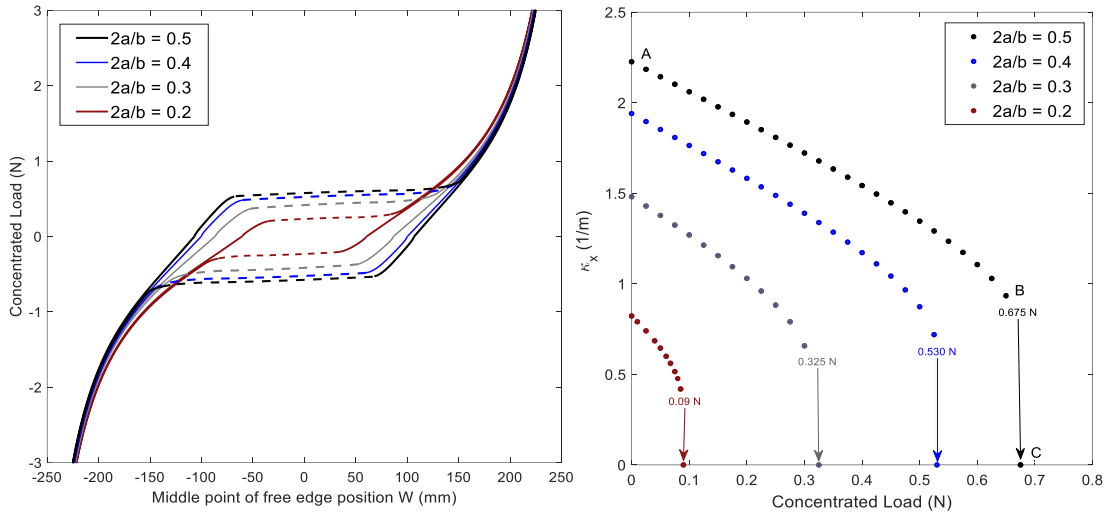


Figure 5-3: The lateral load-tip deflection curves of a clamped m-HBSL with varying bidirectional width using the ABAQUS FE and the variation of the longitudinal curvature  $\kappa_x$  with the applied load for a clamped m-HBSL with varying bidirectional width using analytical model.

Table 12: Comparison of the snapthrough load and tip displacement with varying BD layer width using the analytical model and ABAQUS.

<b>Snapthrough Load (N)</b>			
<b>Configuration</b>	<b>Model</b>	<b>ABAQUS</b>	<b>Error (%)</b>
<b><math>2a/b = 0.5</math></b>	0.675	0.686	1.60
<b><math>2a/b = 0.4</math></b>	0.530	0.5668	6.49
<b><math>2a/b = 0.3</math></b>	0.325	0.46847	30
<b><math>2a/b = 0.2</math></b>	0.09	0.2473	63
<b>Tip Displacement (mm)</b>			
<b>Configuration</b>	<b>Model</b>	<b>ABAQUS</b>	<b>Error (%)</b>
<b><math>2a/b = 0.5</math></b>	100.674	106.859	5.79
<b><math>2a/b = 0.4</math></b>	87.8827	100.213	12.3
<b><math>2a/b = 0.3</math></b>	67.2457	86.7165	22.45
<b><math>2a/b = 0.2</math></b>	37.4874	60.5507	38.08

The results show that the analytical model and ABAQUS are in good agreement except for the case  $2a = 0.2$ , closely match for some parameters. However, for lower  $2a/b$  ratio, the error between the analytical and FEA model increases.

## 5.2. Effect of the BD Glass Epoxy Layer Thickness

Here we investigate the influence of the thickness of the bidirectional glass epoxy layers on the thermally induced bistability of the m-HBSL and the snapthrough response. A schematic of the laminate's cross section of the baseline design is shown in Figure 5-4. The bidirectional plies' width of  $2a/b = 0.5$  is kept fixed and the thickness  $t_{BD}$  is varied. The parameter  $t_{BD}^*$  refers to the new thickness whereas the  $t_{BD}$  refers to the original thickness of the two BD layers, i.e., 0.25 mm. It is worth mentioning that while the thickness of the bidirectional plies varies, the total thickness of the laminate,  $h$ , is kept fixed at 0.75 mm to make the comparison meaningful.

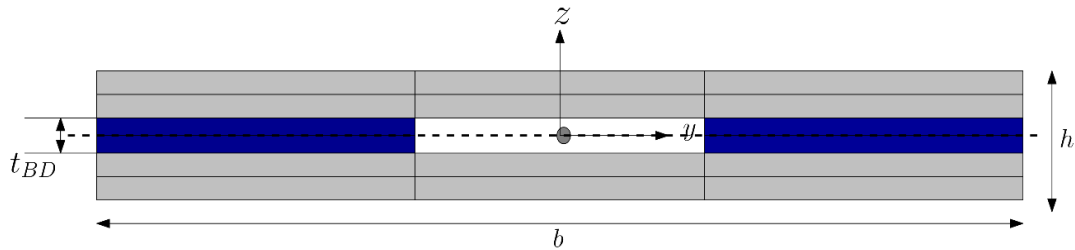


Figure 5-4: A schematic of the laminate's cross section showing the bidirectional layer thickness.

Another way of controlling the curvature and the snapthrough loads can be related to the bi-directional thickness. From the numerical simulations obtained, it is seen that increasing the thickness of bidirectional glass epoxy layers tends to increase the content of the bidirectional prepreg at the expense of the cross-ply prepregs. As per Table 7, the modulus of elasticity of the bidirectional prepregs is bigger than that across the fibers. Therefore, as the thickness increases, the stiffness of the laminate increases and hence the tip deflection decreases and the snapthrough load increases. Table 13 presents the tip deflection and the snapthrough load for a clamped-free m-HBSL with varying BD layers thickness using the analytical model and ABAQUS. The model results match the results of ABAQUS for all cases considered. The table also shows that as the thickness of the BD layers doubles, the tip deflection reduces by 20% and the snapthrough load increases by 51%. This clearly shows that the thickness of the bidirectional layers is significant on the laminate's response. Figure 5-5 presents the bistable configurations of the clamped m-HBSL with varying BD thickness using the

model and ABAQUS, respectively. The right of Figure 5-6 presents the variation of the longitudinal curvature  $\kappa_x$  with the applied load for a clamped m-HBSL with varying bidirectional plies' thickness using analytical model. Finally, the load-deflection plots for the loading and unloading schemes are shown at the left of Figure 5-6. The significance of the BD thickness on the snapthrough and snapback loads, and the laminate's configurations is apparent from the figure.

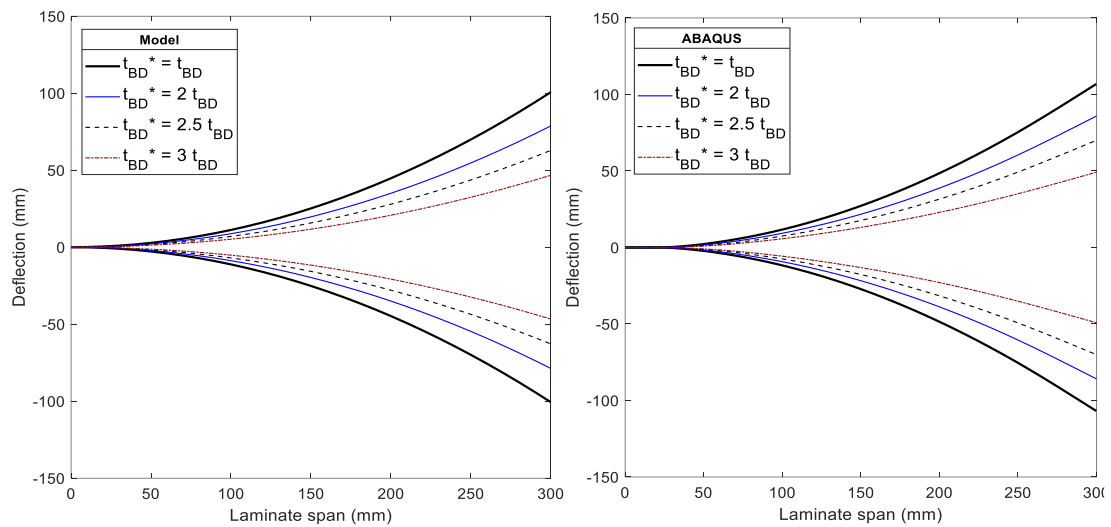


Figure 5-5: Bistable shapes of a clamped m-HBSL with varying bidirectional plies' thickness using the analytical model and ABAQUS.

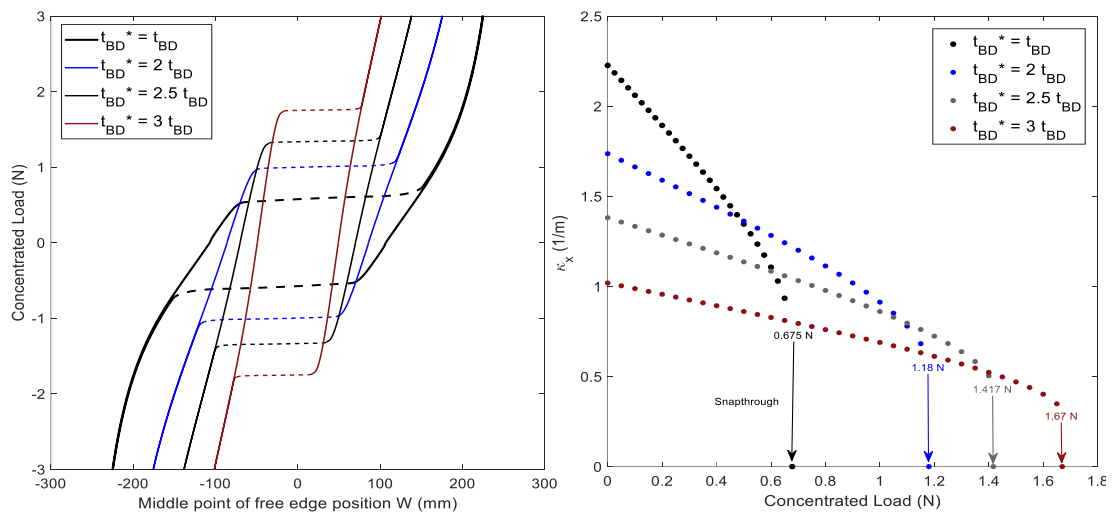


Figure 5-6: The lateral load-tip deflection curves of a clamped m-HBSL with varying bidirectional thickness using ABAQUS FE and the variation of the longitudinal curvature  $\kappa_x$  with the applied load for a clamped m-HBSL with varying bidirectional width using analytical model.

This agrees with the study of [31] which focused on the flexural properties of carbon-epoxy and glass-epoxy hybrid composites, where different stacking configurations of carbon fiber and glass fiber plies were presented. In structural

mechanics, the flexible modulus or bending modulus is defined as the tendency for a material to resist bending. In the paper of [31], results showed that as the glass-epoxy layers thickness are decreased, the flexural modulus decreases. Hence, the structure becomes more flexible or compliant. Table 13 presents the numerical values of the tip deflection and the snapthrough loads for varying bidirectional thickness using the model and ABAQUS.

Table 13: Comparison of the snapthrough load and tip displacement with varying BD layer thickness using the analytical model and ABAQUS.

Configuration	Snapthrough Load (N)		Error (%)	%Load Increase (ABAQUS)
	Model	ABAQUS		
$t_{BD}^* = t_{BD}$	0.675	0.686	1.60	0
$t_{BD}^* = 2 t_{BD}$	1.18	1.03649	13.85	51
$t_{BD}^* = 2.5 t_{BD}$	1.417	1.3456	5.31	96
$t_{BD}^* = 3 t_{BD}$	1.67	1.752	4.68	154
Configuration	Tip Displacement (mm)		Error (%)	% Reduction (ABAQUS)
	Model	ABAQUS		
$t_{BD}^* = t_{BD}$	100.674	106.859	5.79	0
$t_{BD}^* = 2 t_{BD}$	78.7634	85.8839	8.29	20
$t_{BD}^* = 2.5 t_{BD}$	62.8593	70.0526	10.26	34
$t_{BD}^* = 3 t_{BD}$	46.687	49.1976	5.10	54

### 5.3. Effect of the BD Glass Epoxy Layer Location

In this section, the location of the bi-directional glass epoxy layers is varied along the z-axis, i.e., the thickness direction. In the baseline configuration, the glass-epoxy layers are located at the centerline of the laminate  $Z = 0$ . In Figure 5-7a, the bi-directional glass-epoxy layers are located at  $Z_{BD}/h = 0.5$  and  $Z_{BD}/h = -0.5$ . In Figure 5-7b the bi-directional glass-epoxy layers are located at the outer layers of the laminate,  $Z_{BD}/h = 1$  and  $Z_{BD}/h = -1$ . From the obtained results, it is seen that when the bi-directional glass/epoxy layers are placed away from the centerline, i.e.,  $Z_{BD}/h = 0$ ,

the deflection and the initial curvature of the equilibrium shape decreases, as seen in Figure 5-8.

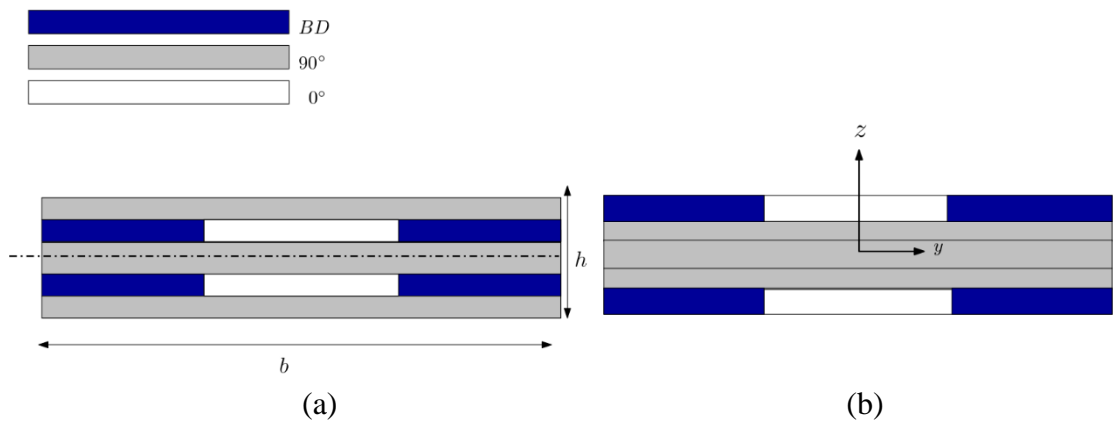


Figure 5-7: Schematic figure of the BD layer's location (a)  $Z_{BD}/h = 0.5$  (b)  $Z_{BD}/h = 1$ .

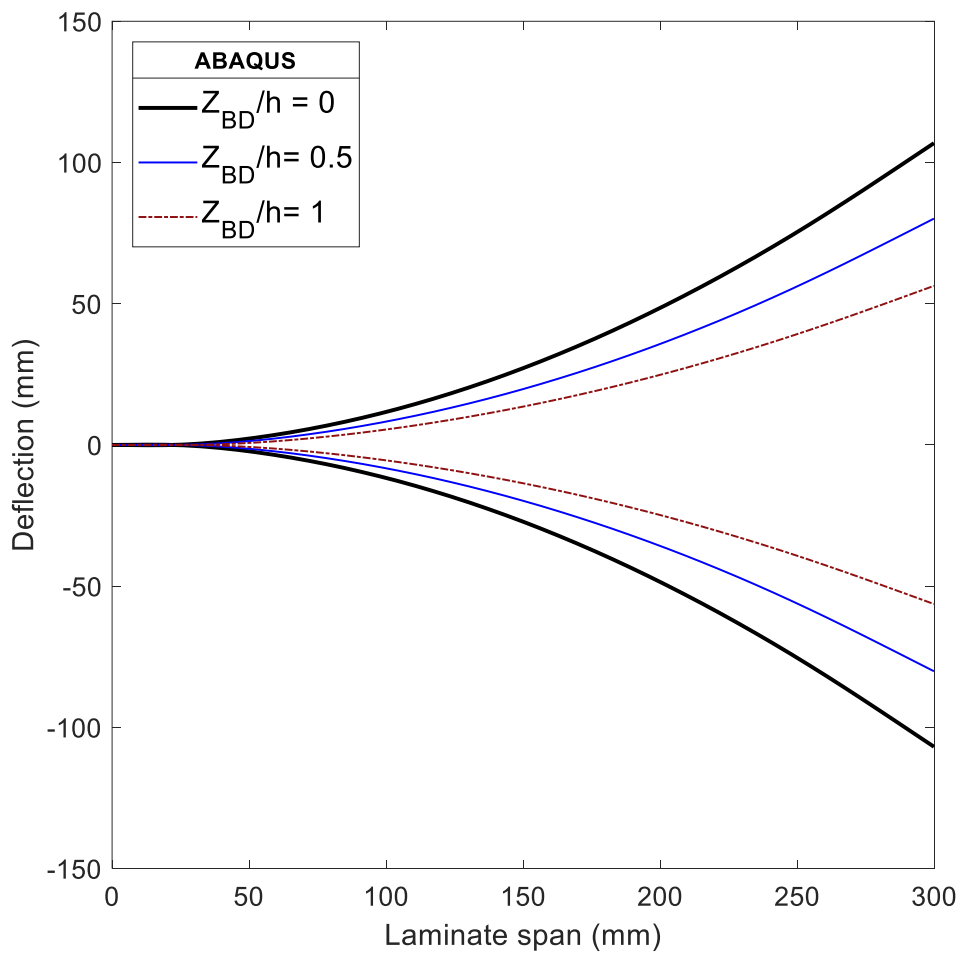


Figure 5-8: Bistable shapes of a clamped m-HBSL with varying bidirectional plies' location using ABAQUS FE.

Figure 5-9 shows the snapthrough behavior for the three different configurations. As the BD layers are placed away from the centerline, the structure becomes stiffer, and this can be observed by examining the slope for each curve. When the BD layers are placed at  $Z_{BD}/h = 1$ , the area under the hypothesis curve reduces, indicating less energy stored within the structure. Also, the load-displacement curve has larger slope, and the critical load where the snapthrough occurs increases to 1.15 N. Therefore, stacking the bi-directional glass/epoxy layers at compressive side (outer layer) where the maximum compressive stress occurs, increase the stiffness of the model yielding to lower stable configuration.

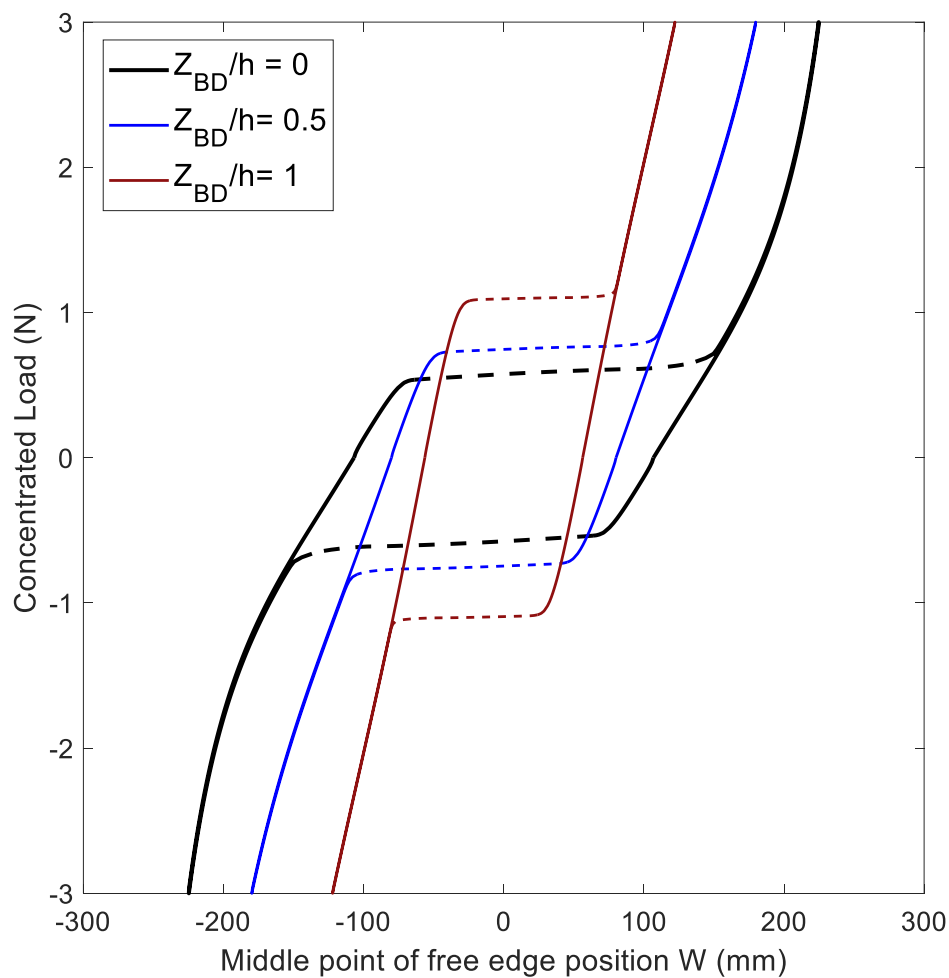


Figure 5-9: Load-deflection curves of a clamped m-HBSL with varying bidirectional plies' location using ABAQUS FE.

The assumed mid-plane strain formulations developed in the model of Li et al. [25] were inspired by the contour maps obtained from ABAQUS FE. For this parameter analysis, the mid-plane strain colormap is shown in Figure 5-10. Where Figure 5-10a

and 5-10b represent the mid-plane distribution for  $Z_{BD}/h = 0$ , whereas Figures 5-10c and 5-10d represent the mid-plane distribution for  $Z_{BD}/h = 0.5$ . The results indicate that as the BD layers are placed away from the centerline, the mid-plane strains distribution i.e.,  $\epsilon_x^0$  and  $\epsilon_y^0$  are changed. Therefore, the formulations of the mid-plane strain Therefore, the formulations of the mid-plane strain presented by Li et. al [25] and Mukherjee et. al [10] are no longer valid. To validate this analysis with ABAQUS FE, different strain fields formulation should be used.

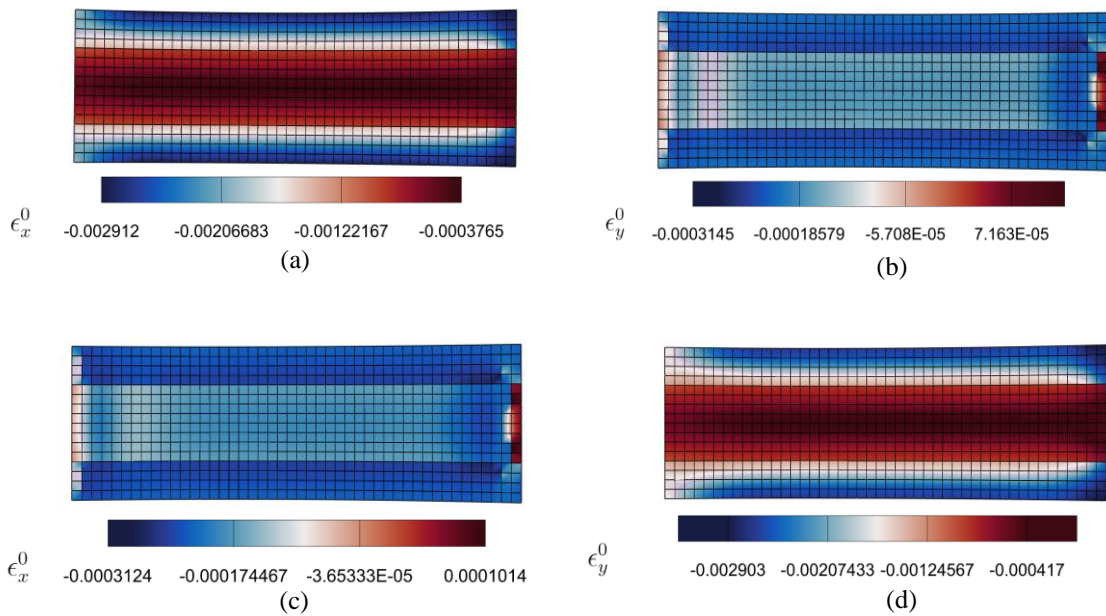


Figure 5-10: Midplane strain colormap for different configurations (a-b)  $Z_{BD}/h = 0$  (c-d)  $Z_{BD}/h = 0.5$

## Chapter 6. An Innovative Bistable Wing

An important aspect in morphing aircraft is that the wing of the aircraft dynamically change state in flight. A bistable morphing wing structure can be engineered to be flexible or stiff, depending on the application. This is achieved through careful and combined selection of material properties and layup sequence. Structures engineered in this way can retain bistability even when constrained under certain conditions, such as fixing one edge. The most important feature of using bistable composites, compared with other smart structures, is that the required load to cause change is only required momentarily to initiate the transition. No continuous power is required to snap from one state to another. In this chapter, the analytical model of Mattioni et al. [22] is improved by replacing the unsymmetric plate with the modified hybrid bistable symmetric laminate proposed by Mukherjee et al. [10] to achieve a structure that has two stable shapes with same curvature values. A schematic figure of the proposed design is shown in Figure 6-1 where the main wing represents the symmetric laminate in the analysis, and the winglet is the modified hybrid bistable laminate. The proposed design is named as an “innovative hybrid bistable symmetric laminate, i-HBSL”.

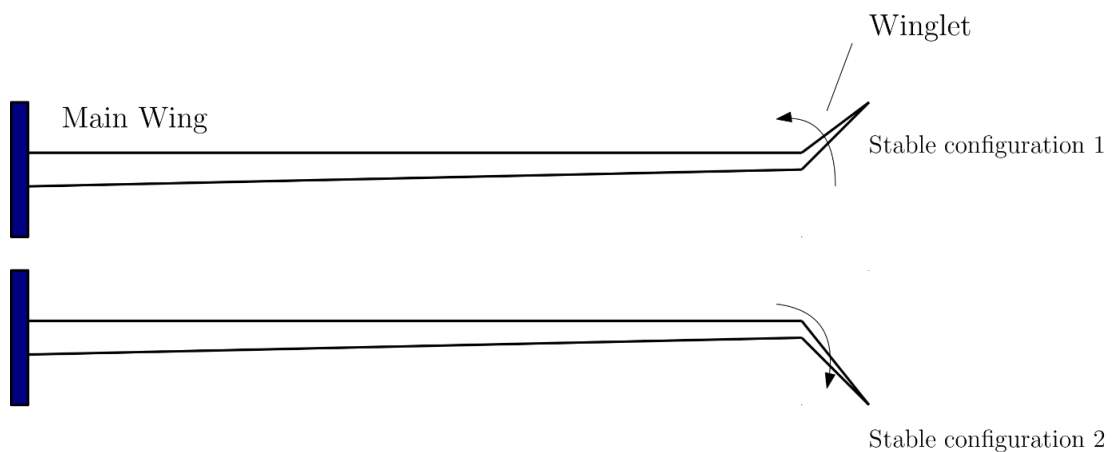


Figure 6-1: Schematic figure of the proposed innovative composite wing.

### 6.1. Analytical Model of an Innovative Hybrid Bistable Symmetric Laminate

A mathematical model is developed to study hybrid symmetric bistable laminates (HBSL) using Rayleigh-Ritz- minimization discussed in the previous chapters. The preliminary results from the previous chapter showed that most of the analytical models were restricted to free-free boundary conditions for predicting

equilibrium states and snapthrough. Mattioni et al. [22] was the first to extend the modeling efforts and consider the continuity requirements between a symmetric and an unsymmetric plate. In the proposed i-HBSL model, the HBSL segment is attached to an elastic structure instead of a rigid wall. This extends the development of bistable wings and proceeds to more realistic configurations. A schematic figure of the layup is shown in Figure 6-2.

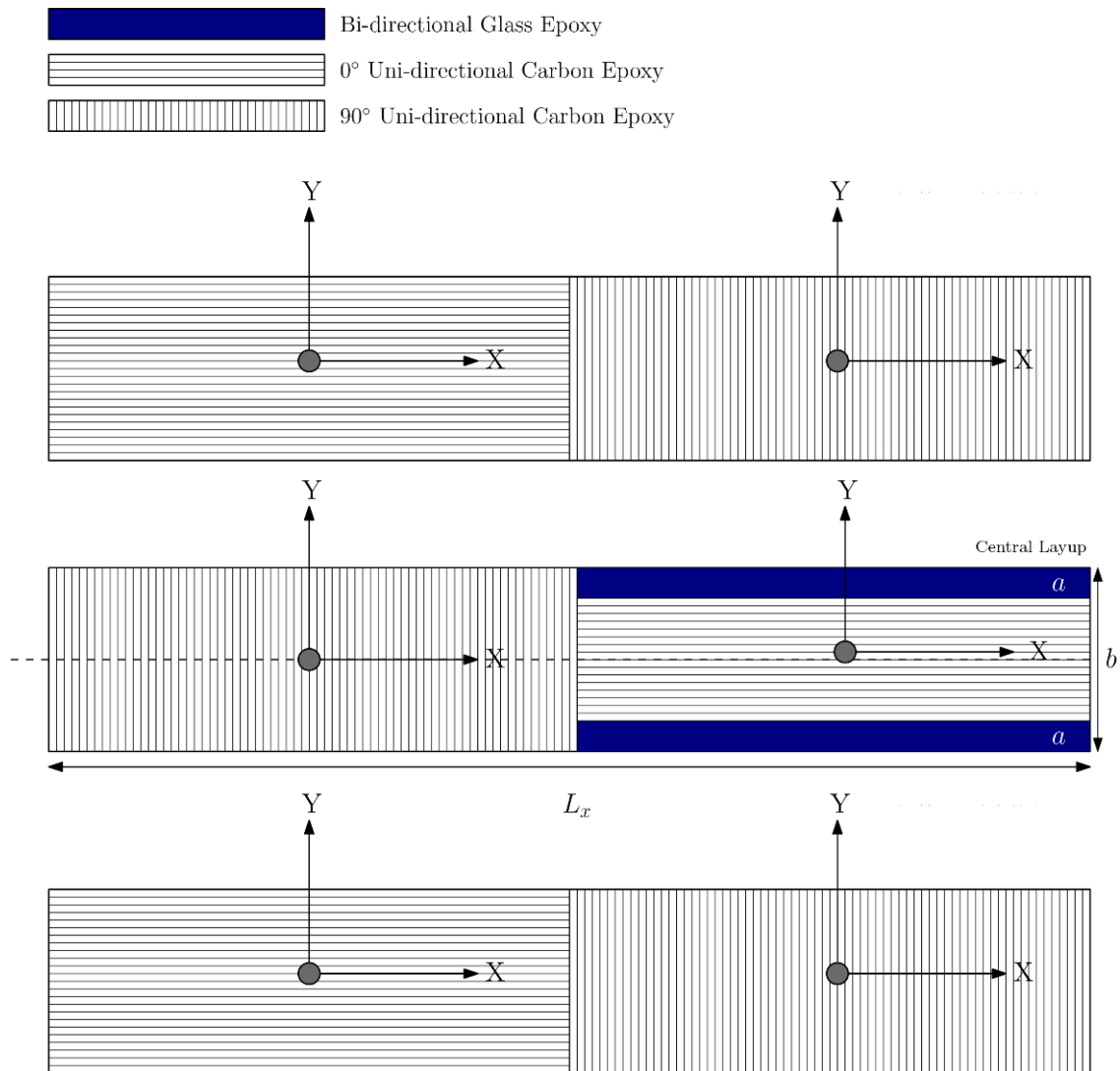


Figure 6-2: Schematic of the stacking sequence of the proposed innovative bistable composite wing (i-HBSL).

The new structure has a length span of  $L_x = 600$  mm and a width, chord of  $b = 100$  mm. The left-hand side of the plate has a symmetric stacking sequence  $(0_2/90)_s$ , while the m-HBSL on the right-hand side consists of three sections: two outer sections with the layup  $(90_2/BD/90_2)_s$  and an inner section with

layup  $(90_2/0_2/90_2)_s$ . The flat and bistable panels attached together make the innovative suggested wing structure. The dimensions of the outer sections are  $300 \times 25$  mm, whereas the dimensions of the inner sections are  $300 \times 50$  mm. The material properties used throughout the analysis are shown in Table 6. The isometric view of the layup of the proposed model is shown in Figure 6-3.

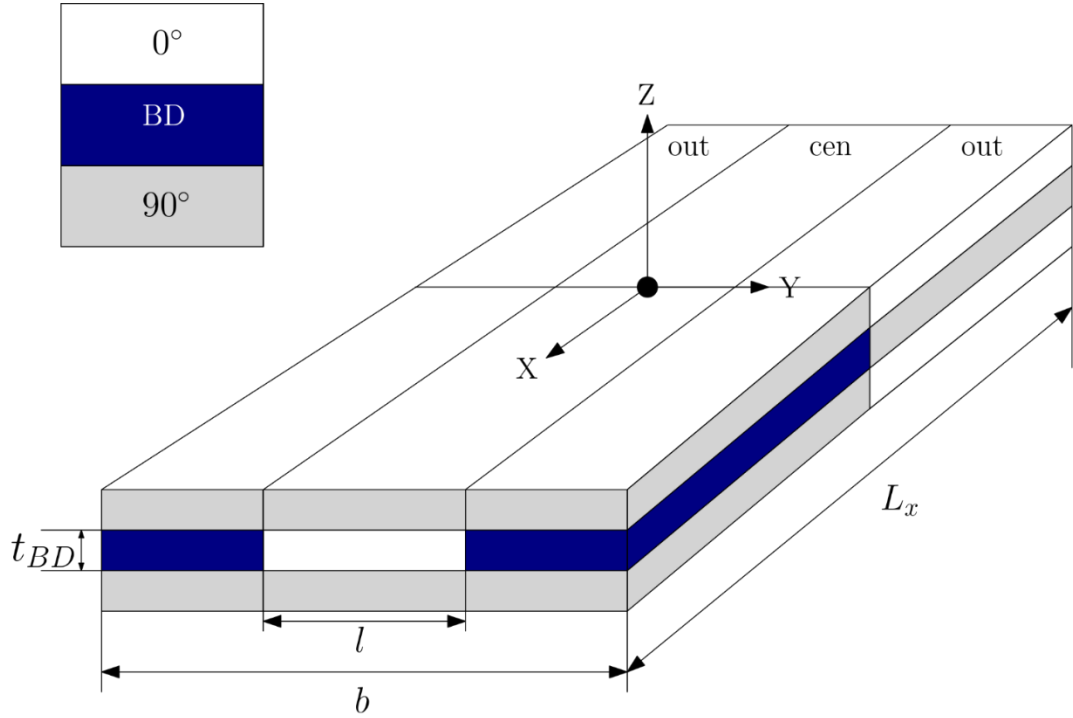


Figure 6-3: Isometric view of the proposed innovative bistable composite wing (i-HBSL).

The structure illustrated in Figure 6-4 is chosen as an example for developing the extended analytical model, which consists of two plates connected along one edge. Let  $A$  be the domain of the whole structure.

$$A = A_1 \cup A_2 \quad (77)$$

where  $A_1$  represents the first plate and  $A_2$  represents the multi-sectioned plate. Despite the use of a multi-sectioned layup, continuous displacement and strain fields were selected for analysis, a more refined model can be obtained by assuming piece-wise displacement fields and enforcing continuity conditions at the interface. This, however, increases the computational cost due to the increased number of unknowns. The out-of-plane displacement selected for the two plates is given by the following:

$$w(x_i, y)^{(i)} = c_9^{(i)} + c_{10}^{(i)} x_i + c_{11}^{(i)} y + c_{12}^{(i)} x_i^2 + c_{13}^{(i)} y^2 + c_{14}^{(i)} x_i y + c_{15}^{(i)} x_i y^2 + c_{16}^{(i)} x_i^2 + c_{17}^{(i)} x_i^2 y^2 \quad (78)$$

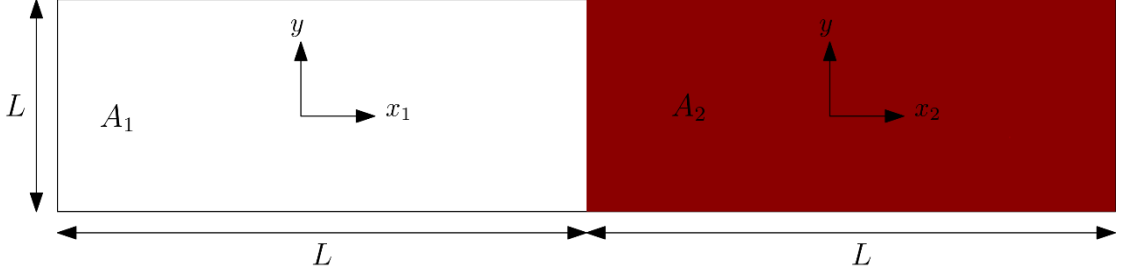


Figure 6-4: Model geometry and coordinate system.

The superscripts (1) and (2) represent the first and second plate of the structure. The strain functions are as follows:

$$\epsilon_x^{0(i)} = c_1^{(i)} + c_2^{(i)} x^2 + c_3^{(i)} x y_i + c_4^{(i)} y_i^2 \quad (79)$$

$$\epsilon_y^{0(i)} = c_5^{(i)} + c_6^{(i)} x^2 + c_7^{(i)} x y_i + c_8^{(i)} y_i^2 \quad (80)$$

The in-plane displacements can be obtained through the following expressions:

$$\epsilon_x^{(i)} = \frac{\partial u^{(i)}}{\partial x} + \frac{1}{2} \left( \frac{\partial w^{(i)}}{\partial x} \right)^2 \quad (81)$$

$$\epsilon_y^{(i)} = \frac{\partial v^{(i)}}{\partial y} + \frac{1}{2} \left( \frac{\partial w^{(i)}}{\partial y} \right)^2 \quad (82)$$

Integrating the above expressions and solving for the in-plane displacements yields to 4 additional coefficients.

$$u_{(x,y)}^{(i)} = \int \left[ \epsilon_x^0 - \frac{1}{2} \left( \frac{\partial w^0}{\partial x} \right)^2 \right] dx + c_{18} y + c_{19} y^3 \quad (83)$$

$$v_{(x,y)}^{(i)} = \int \left[ \epsilon_y^0 - \frac{1}{2} \left( \frac{\partial w^0}{\partial y} \right)^2 \right] dx + c_{20} x + c_{21} x^3 \quad (84)$$

The expression for  $\gamma_{xy}^{(i)}$  is obtained through the following:

$$\gamma_{xy}^{(i)} = \frac{\partial u^{(i)}}{\partial y} + \frac{\partial v^{(i)}}{\partial x} + \frac{\partial w^{(i)}}{\partial x} \frac{\partial w^{(i)}}{\partial y} \quad (85)$$

The strain  $\epsilon_x^{(i)}(x, y)$  and curvature vectors can be assembled as the following:

$$\epsilon^{(i)} = \begin{Bmatrix} \epsilon_x \\ \epsilon_y \\ \gamma_{xy} \end{Bmatrix}^{(i)} \quad (86)$$

$$\kappa^{(i)} = \begin{Bmatrix} -\frac{\partial^2 w^o}{\partial x^2} \\ \frac{\partial^2 w^o}{\partial y^2} \\ -2\frac{\partial^2 w^o}{\partial x \partial y} \end{Bmatrix}^{(i)} \quad (87)$$

The strain energy of the entire structure can now be calculated using a Rayleigh-Ritz technique similar to that used by Hyer [12]. Each substructure has an individual strain energy that is formulated considering the different stacking sequences, and integration limits, and then the two contributions are combined to obtain the total strain energy.

$$\begin{aligned} \Pi = & \iint_{A_1} \frac{1}{2} \left( \begin{bmatrix} \epsilon^{(1)} \\ \kappa^{(1)} \end{bmatrix}^T \begin{bmatrix} A^1 & B^1 \\ B^1 & D^1 \end{bmatrix} \begin{bmatrix} \epsilon^{(1)} \\ \kappa^{(1)} \end{bmatrix} - \begin{bmatrix} \epsilon^{(1)} \\ \kappa^{(1)} \end{bmatrix}^T \begin{bmatrix} N^{th} \\ M^{th} \end{bmatrix}^1 \right) dx dy + \\ & \iint_{A_2} \frac{1}{2} \left( \begin{bmatrix} \epsilon^{(2)} \\ \kappa^{(2)} \end{bmatrix}^T \begin{bmatrix} A^2 & B^2 \\ B^2 & D^2 \end{bmatrix} \begin{bmatrix} \epsilon^{(2)} \\ \kappa^{(2)} \end{bmatrix} - \begin{bmatrix} \epsilon^{(2)} \\ \kappa^{(2)} \end{bmatrix}^T \begin{bmatrix} N^{th} \\ M^{th} \end{bmatrix}^2 \right) dx dy \end{aligned} \quad (88)$$

where  $\epsilon^{(1)}$  and  $\kappa^{(1)}$  are the mid-plane strains and in-plane curvatures respectively  $A^1$ ,  $B^1$ ,  $D^1$ ,  $A^2$ ,  $B^2$ ,  $D^2$ , are the laminate stiffness matrices,  $[A]$ ,  $[B]$  and  $[D]$  are extensional stiffness matrix, bending extension coupling stiffness matrix and bending stiffness matrix respectively.  $N^{th(1)}$ ,  $N^{th(2)}$ ,  $M^{th(1)}$ ,  $M^{th(2)}$  are the thermally induced force and moment vectors respectively.

The total strain energy  $\Pi = \Pi(c_{(j)}^{(i)})$  is a function of 42 unknown coefficients, Where  $j = 1, 2, 3, \dots, 21$  for  $i = 1, 2$ . The local minima of the total strain energy correspond to the stable shapes of the plate. In order to ensure continuity of displacement across domain A, the following compatibility conditions must hold:

$$w_1\left(\frac{L_1}{2}, y\right) = w_2\left(\frac{-L_2}{2}, y\right) \quad (89)$$

$$\frac{\partial w_1}{\partial x}\left(\frac{L_1}{2}, y\right) = \frac{\partial w_2}{\partial x}\left(\frac{-L_2}{2}, y\right) \quad (90)$$

$$u_1\left(\frac{L_1}{2}, y\right) = u_2\left(\frac{-L_2}{2}, y\right) \quad (91)$$

$$v_1\left(\frac{L_1}{2}, y\right) = v_2\left(\frac{-L_2}{2}, y\right) \quad (92)$$

A non-linear constrained optimization method has been used for  $\Pi = \Pi(c_j^{(i)})$  to find the solutions for the present study. Eqs. (89-92) show the constraints used in the analysis to satisfy continuity between the two plates. The analysis has been carried out using the commercial optimization package ‘fmincon’ on MATLAB and the required constraints was set as nonlinear constraints for the optimization tool.

## 6.2. Finite Element Implementation

The equilibrium shapes and snapthrough curves of the proposed model are obtained in *ABAQUS*<sup>®</sup>, using the ‘Static, stabilize procedure’. The proposed laminate is modeled using four noded shell elements (S4R). To account for the geometric nonlinearities the option Nlgeom is kept on during the analysis. To ensure convergence and accuracy of results, an artificial damping factor is used. To obtain the equilibrium shapes with clamped boundary condition, the two following steps are used:

In the first step, an initial temperature field of 150° is applied over the entire model. The laminate is then cooled to room temperature at 30° and an unstable flat configuration is obtained during this step due to the symmetry in the layup. In the second step, the clamped boundary condition is added on the edge of the model, and a concentrated point load is applied at the center of the free edge in z direction. Subsequently, the applied load is removed using an empty step and the laminate settles to one of the two stable equilibrium shapes. To obtain the second equilibrium stable shape, the direction of the concentrated load is changed.

**6.2.1. Snapthrough analysis.** The ‘snap through’ analysis describes the elastic response of the structure when loaded with a concentrated force. During the application of the load, the structure will first deform elastically (i.e., a linear relationship between

force and displacement). When the force reaches a critical magnitude, the structure will buckle and eventually rest in the other stable configuration once the load is removed. The flowchart in Figure 6-5 shows the steps of the procedures.

For the snapthrough analysis, two additional steps are added in the ABAQUS model: A concentrated point load is applied at the center of the free edge, in the direction opposite to the applied test load in the previous steps. The applied load is removed in the final step and the model settles to the other equilibrium stable configuration.

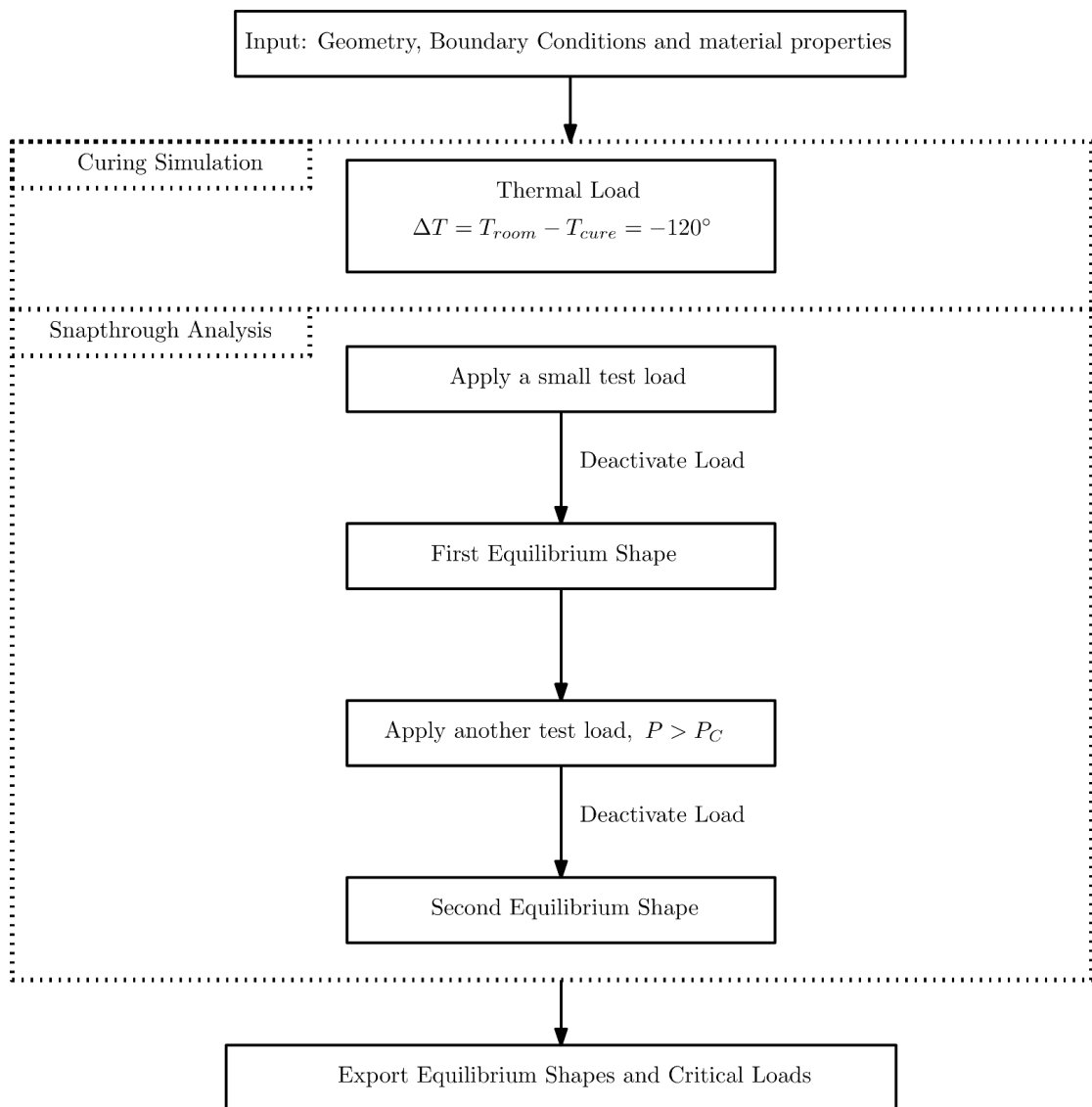


Figure 6-5: FEA simulation flowchart.

## Chapter 7. Results and Discussion

In this chapter, the results obtained using the proposed analytical model discussed in the previous chapter is presented. The parametric analysis for the single m-HBSL plate is repeated for the compound plate to analyze the effect of attaching a multi-sectioned symmetric laminate to a larger structure or an elastic body. The parametric study also analyzes the effect of the load position, length of the symmetric plate and thickness mismatch on the snapthrough behavior. The analysis is based on a fixed BD layer width of 50 mm, i.e.,  $2a/b = 0.5$ . For the baseline configuration the symmetric and multi-sectioned plate have the same length, i.e.,  $L_1/L_2 = 1$ . The equilibrium shape of the proposed innovative composite wing is shown in Figure 7-1 using ABAQUS FE.

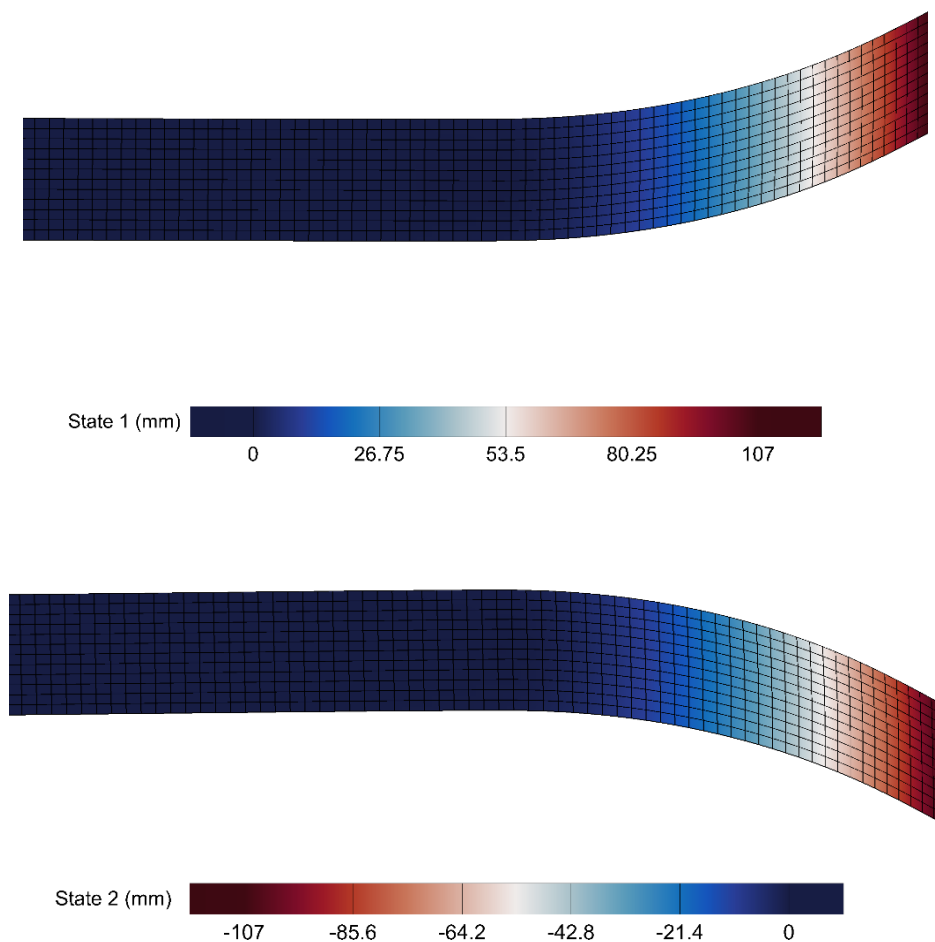


Figure 7-1: Stable equilibrium shapes of the Innovative Composite Wing.

A comparison of the equilibrium shape obtained using the analytical model analyzed in the previous chapter and ABAQUS FE is shown in Figure 7-2. A good agreement is achieved between the simplified proposed model and ABAQUS for the base model.

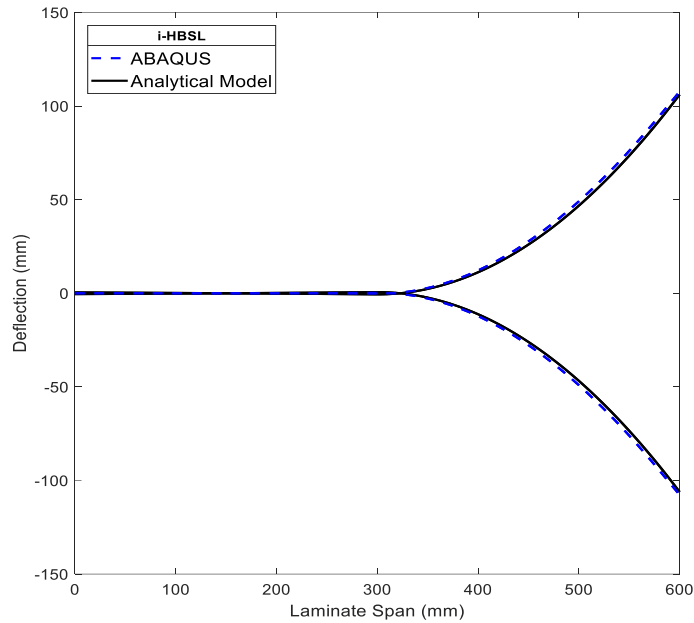


Figure 7-2: Bistable shapes of the innovative composite wing (i-HBSL) using the analytical model and ABAQUS FE.

A bistable laminate's snapthrough properties change significantly when clamped. Many studies have been dedicated to understanding static shapes and snapthrough, though they are limited to free-free boundary conditions. When deploying bistable laminates for structural applications, it is extremely important to understand the nonlinear snapthrough phenomenon. This is achieved by analyzing the snapthrough of the i-HBSL proposed model under various loading condition and parametric studies.

The objectives of this chapter are summarized as follows:

- Study the effect of BD layer thickness and location on the equilibrium shapes and snapthrough loads for the i-HBSL.
- Study the effect of load position along the chord length on the equilibrium shapes and snapthrough loads.
- Analyze the effect of varying the symmetric plate length on the equilibrium shapes and snapthrough loads.
- Analyze the effect of thickness mismatch on the equilibrium shapes.

### 7.1. Effect of the Length of the Flat Segment

The first parameter to consider is the length ratio of the flat plate,  $L_1$  to the HBSL  $L_2$ . The schematic figure of the parameter is shown in Figure 7-3. The equilibrium shapes for different  $L_1/L_2$  ratio at  $2a/b = 0.5$  is seen at the left of Figure 7-4. It is observed that changing the length of the flat plate  $L_1$  does not influence the curvatures of the equilibrium shapes. The load-deflection curve for different  $L_1/L_2$  ratios are presented at the right of Figure 7-4. It is seen that the longer the laminate span, the larger the deflection of the HBSL. At  $L_1/L_2 = 2$ , the deflection is higher at the same applied load, therefore, increasing the length of the flat plate segment plays a significant role in the flexibility of the structure.

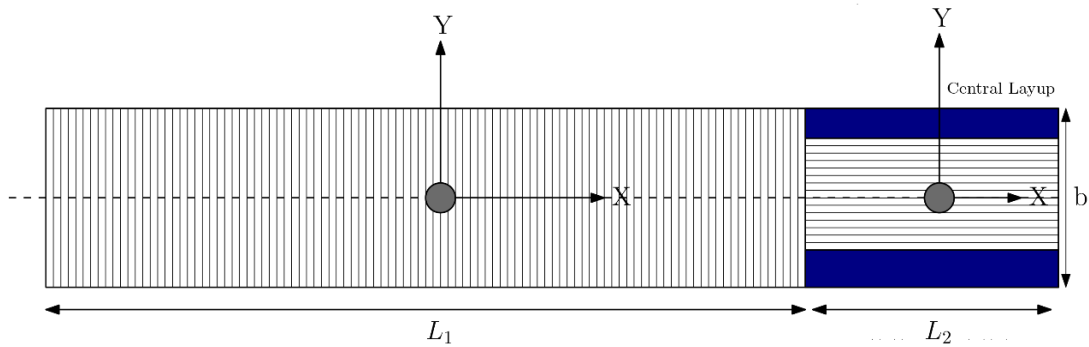


Figure 7-3: Schematic of the proposed innovative bistable composite wing with  $L_1$  varying.

The flexibility of the wing is due to the loads of the wing being shared by all the individual components, meaning that the forces are being equally distributed throughout the wing, if the wing is completely stiff, this indicates that all the forces being applied is concentrated to a certain part in the wing, and this part can be subjected to metal fatigue. However, maintaining flexibility limitations is important to avoid wing break off, this can be done by providing sufficient strength to the structure and proper mass balance to the control surfaces. The flexibility of the structure can be controlled by the varying the parameters discussed in the previous Chapter. However, the length of the flat plate does not have impact on the snapthrough load.

### 7.2. Effect of the BD Glass Epoxy Layer Thickness

The effect of the BD Glass/Epoxy layer thickness was discussed previously on the single m-HBSL. It was observed that changing the thickness of the BD layers has a significant impact on the snapthrough loads and the equilibrium shapes, in which

increasing the thickness of the bidirectional glass/epoxy layers yields to increase in the snapthrough loads and decrease in the tip deflection of the laminate. Similar behavior is obtained using the i-HBSL.

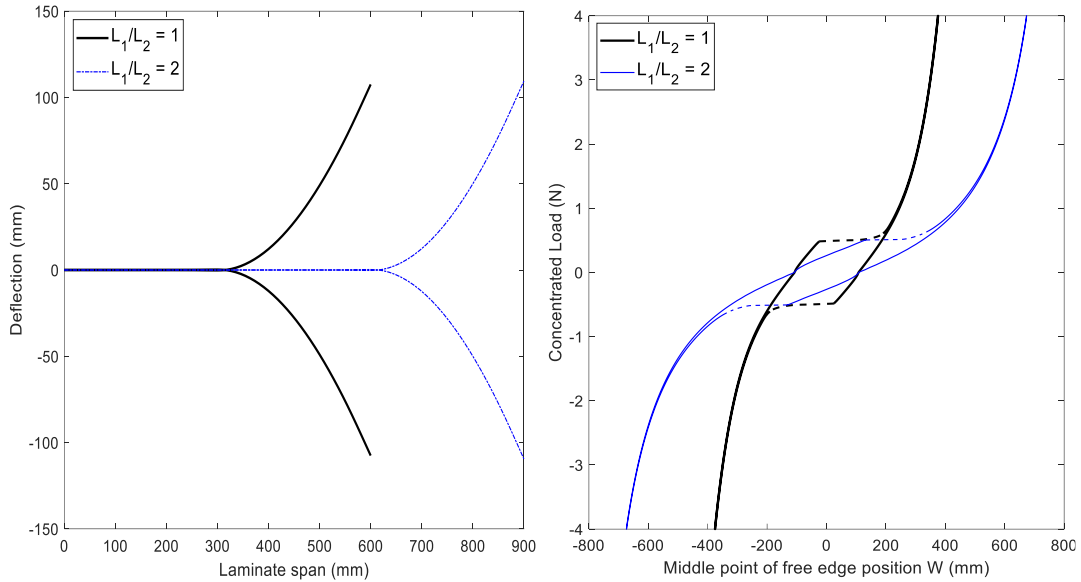


Figure 7-4: The equilibrium shapes and load-deflection curves at different  $L_1/L_2$  ratios.

Figure 7-5 shows the equilibrium shapes and the load-deflection curve obtained for three different configurations. The load-deflection curve is presented to analyze the snapthrough and snapback behavior. Observing the load-deflection curve obtained with the compound plate and single m-HBSL seen in the previous chapter, the relationship between the BD layers thickness and snapthrough loads is similar. Increasing the thickness of the bi-directional  $t_{BD}$  tends to increase the snapthrough load due to the increase in the stiffness of the model.

Figure 7-6 shows the contour maps of the longitudinal curvatures  $\kappa_x$  at different BD layer thickness. Comparing curvature distribution  $\kappa_x$  for the baseline configuration where the BD layer thickness is 0.25 mm, with the third configuration where the BD layer thickness is increased to 3 times the original thickness, i.e.,  $t_{BD} = 0.75$  mm, a change in the curvature  $\kappa_x$  is seen on the end of the flat segment. Therefore, the flat plate experiences a change in the curvature when the BD layer thickness is increased beyond a certain ratio, which indicates that the effect of the bidirectional layers is now extended to the flat plate, causing a curvature along the x axis.

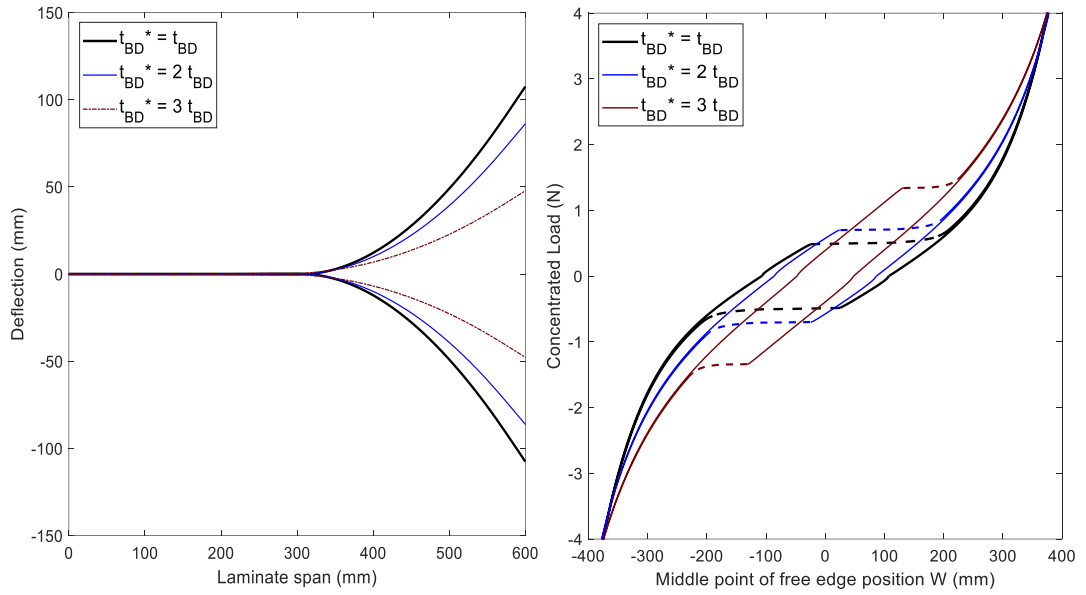


Figure 7-5: The stable equilibrium shapes and load-deflection curve of the compound m-HBSL plate with varying bidirectional plies' thickness using ABAQUS.

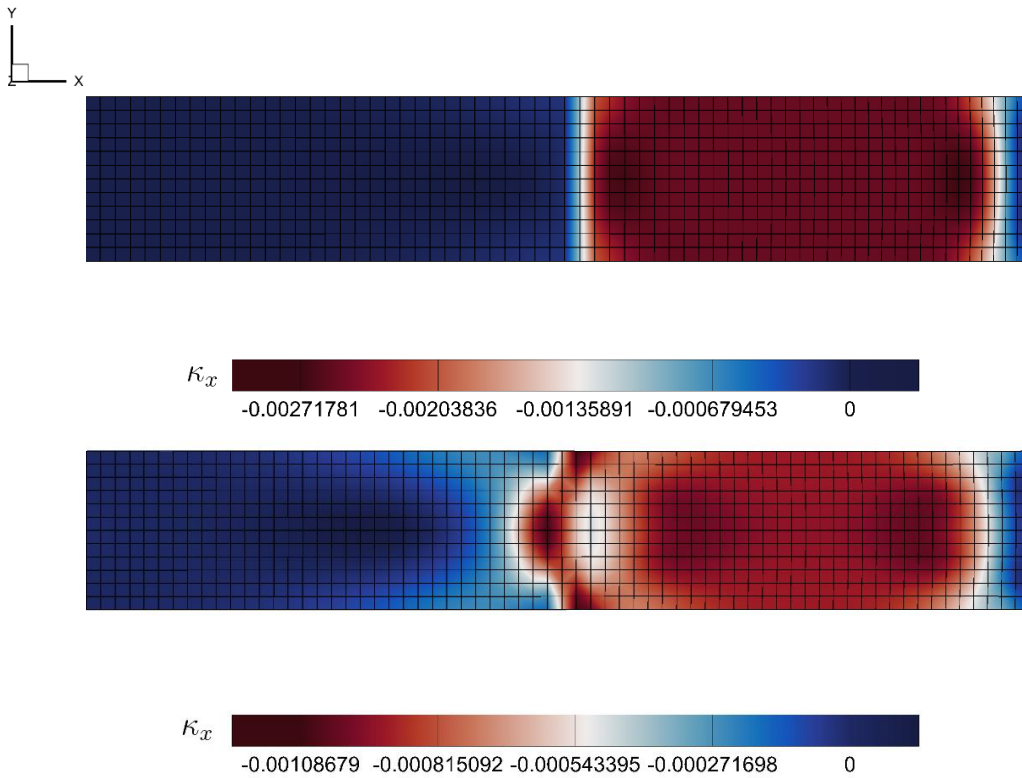


Figure 7-6: Contour maps of the longitudinal curvatures  $\kappa_x$  at different BD layer thickness (a)  $t_{BD} = 0.25$  mm (b)  $t_{BD} = 0.75$  mm.

### 7.3. Effect of the BD Glass Epoxy Layer Location

This section shows the effect of the bidirectional glass/epoxy layer location on the equilibrium shapes and snapthrough loads for the i-HBSL model. As observed in

the previous Chapter, relocating the bidirectional glass/epoxy layers have a huge impact on the snapthrough load, equilibrium shapes and midplane distribution.

The left of Figure 7-7 shows the equilibrium shapes of the i-HBSL at three different configurations,  $Z_{BD}/h = 0$ ,  $Z_{BD}/h = 0.5$  and  $Z_{BD}/h = 1$ . When the BD layers are placed away from the centerline, a reduction in the displacement of the equilibrium shape is observed, and the snapthrough load increases by 40.625% when the layers are placed at the top and bottom layers of the laminate, i.e.,  $Z_{BD}/h = 1$  and  $Z_{BD}/h = -1$ . Therefore, changing the location of the bidirectional layers play key role in changing the snapthrough behavior of the laminate.

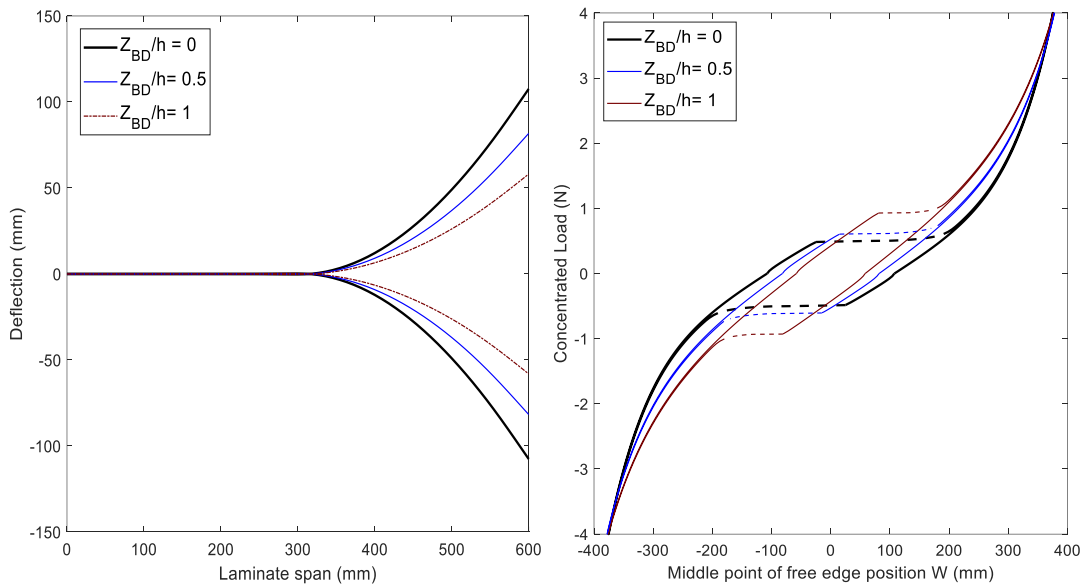


Figure 7-7: The stable equilibrium shapes of the compound m-HBSL and load-displacement plot with varying bidirectional plies' location using ABAQUS.

The contour maps of mid-plane strains  $\epsilon_x^0$  and  $\epsilon_y^0$  are shown in Figure 7-8 for two configurations,  $Z_{BD}/h = 0$  and  $Z_{BD}/h = 1$ . The midplane strain for the two equilibrium shapes are identical, therefore, results of one of the stable shapes is presented. FEA results have shown that characteristics, such as the midplane strain are different when the location of the bidirectional layers is changed. Figures 7-8c and 7-8d show the midplane distribution when the bidirectional layers are placed away from the centerline, and the two  $90^\circ$  composite plies of the hybrid and central region are placed at the midplane of the laminate as illustrated in Figure 5-7b. The midplane strain  $\epsilon_x^0$  in the central region is assumed to be quadratic in the  $x$ -direction and vary linearly along the  $y$ -direction in the hybrid region as seen in Figure 7-8c. Whereas the midplane

strain  $\epsilon_y^0$  is assumed to be continuous along the  $\epsilon_y^0$  and independent of  $x$ . This is the opposite of the colormap obtained with the base configuration, i.e.,  $Z_{BD}/h = 0$ .

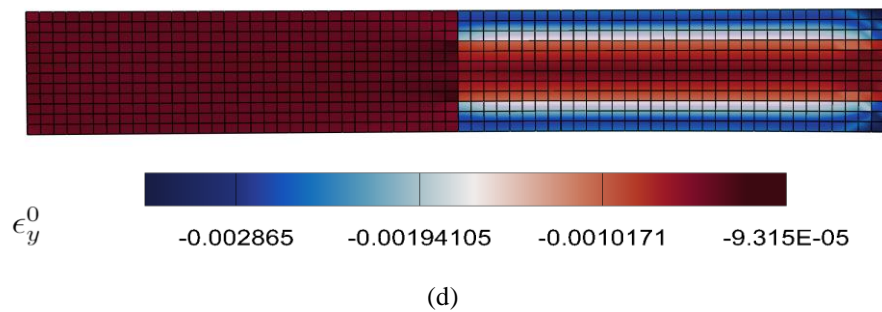
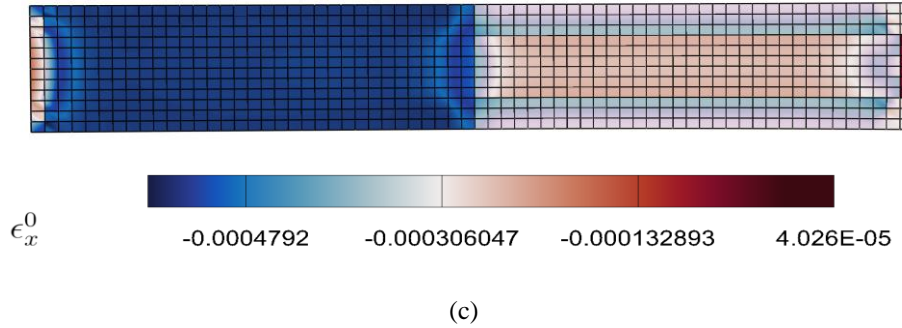
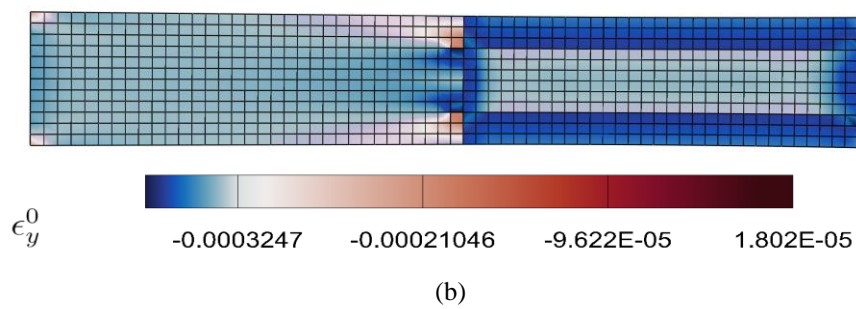
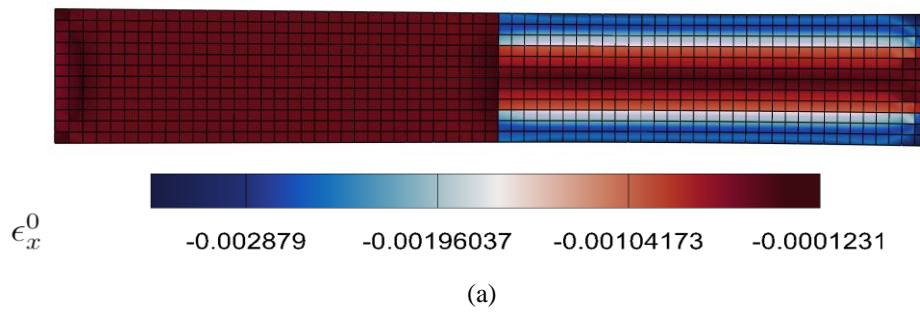


Figure 7-8: Contour maps of mid-plane strain at different BD layer location (a-b)  $Z_{BD}/h = 0$  (c-d)  $Z_{BD}/h = 1$ .

## 7.4. Effect of the Concentrated Load Location

Here we consider the effect of varying the concentrated load position along the centerline as seen in Figure 7-9. It can be seen from the displacement plot, which depending on the distance of the applied load at the centerline of the model, different sets of stable equilibrium configurations can be obtained, named as stable intermediate states. Figure 7-10 shows the equilibrium shapes and load-deflection curve at different load positions where  $L_p$  represent the distance of the applied load on the second plate ( $L_2$ ).

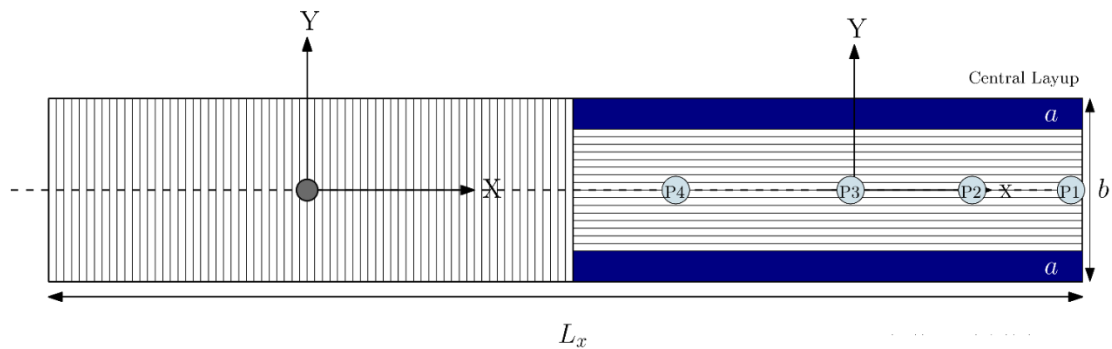


Figure 7-9: Schematic figure of the load applied at different locations.

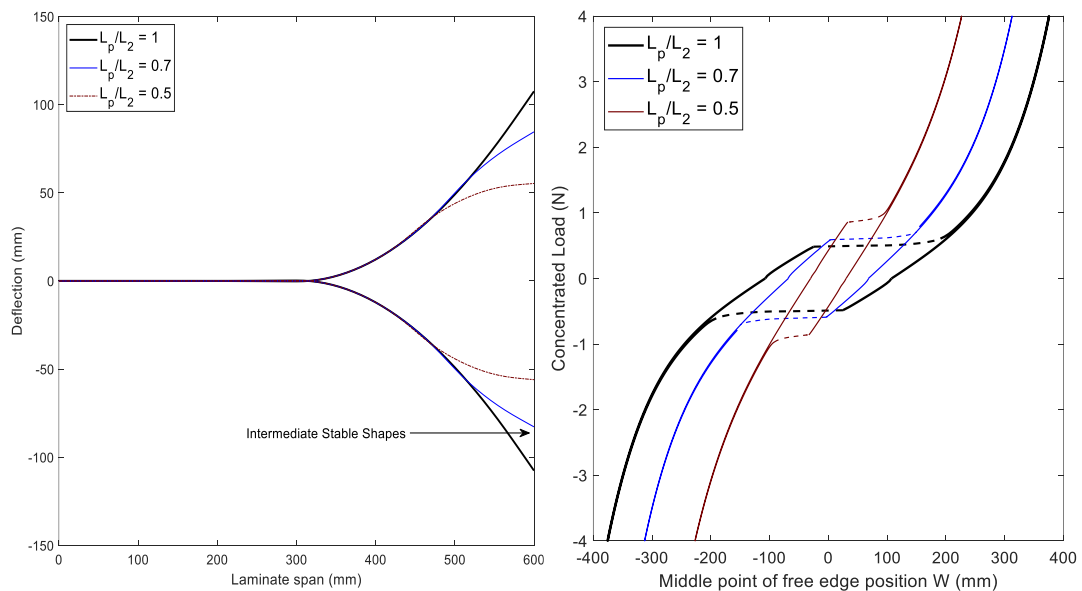


Figure 7-10: The stable equilibrium shapes and load-deflection curve of the compound m-HBSL plate with varying the concentrated load location using ABAQUS.

The position of the applied load has impact on the snapthrough loads. As the load is applied close to the fixed edge of the flat plate, an increase in the snapthrough load is observed. A reduction in the area under the hysteresis curve is also observed as

the distance of the load application from the clamped edge decreases, in addition, it is seen that the snapthrough is not very important for load positions near the fixed edge, as there is no sudden change in the displacement when the applied load is increased. The left of figure 7-10 shows three sets of stable equilibrium shapes that are obtained depending on the distance of force application. The three stable sets are indicated as **I**, **II** and **III**, the load distance ratio of  $L_p/L_2 = 1$  results in the equilibrium state **I**, whereas the load distance ratio  $L_p/L_2 = 0.7$  results in the equilibrium state **II**. When the load distance ratio is less than 0.7, the stable shape is assigned to equilibrium state **III**. In addition, it is seen that the two stable shapes loss symmetry when the load is applied near the flat plate regardless of the model being fully symmetric. Figure 7-11 shows the isometric view of intermediate stable equilibrium shapes.

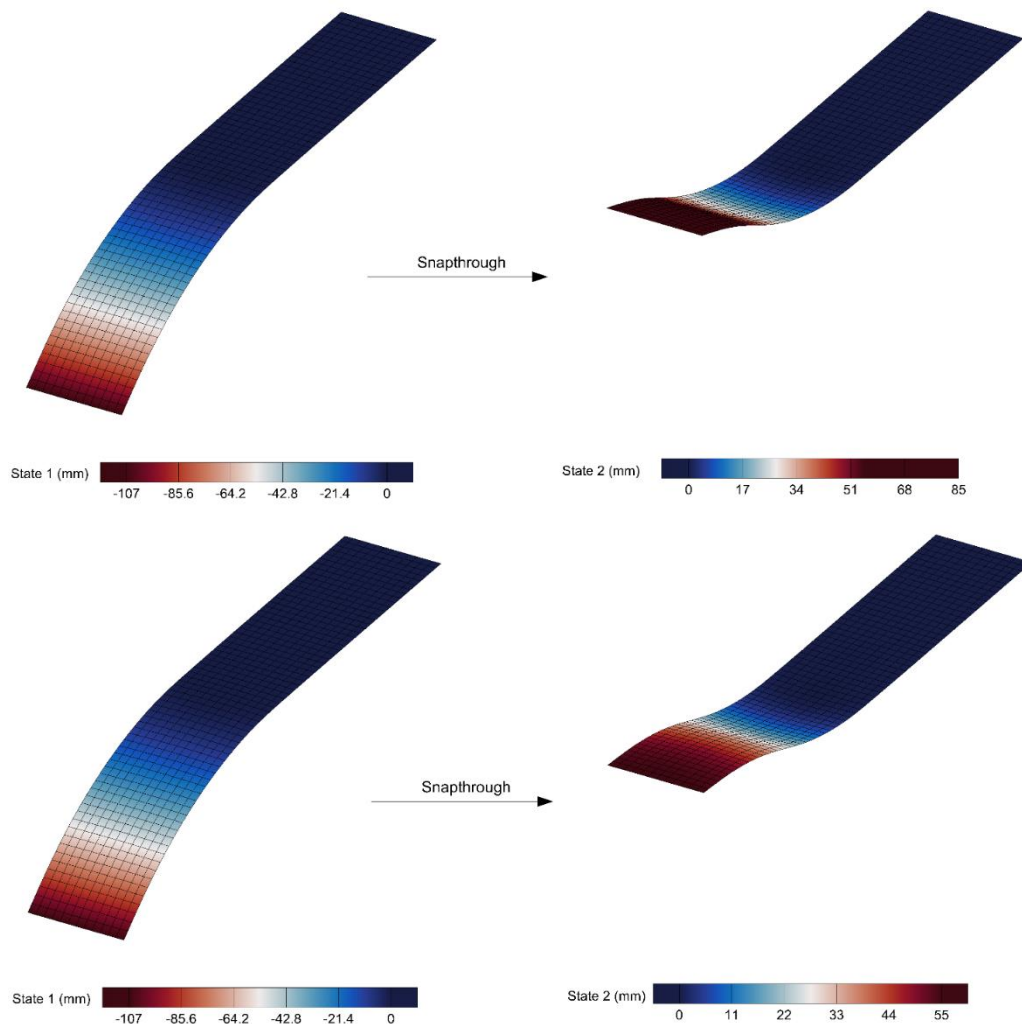


Figure 7-11: The intermediate shapes at different load locations,  $L_p/L_2 = 0.7$  and  $L_p/L_2 = 0.5$ .

## 7.5. Effect of the Thickness Mismatch

In this section, the impact of imperfections on the snapthrough performance of the proposed model is analyzed. It is sometimes difficult to eliminate the mismatch between inner carbon\epoxy and outer hybrid layers while setting up the layup manually on the mold. Hence, thickness mismatch between the layers can be caused due to the following:

- Thickness variation of the hybrid plies.
- Manually setting up the layers while manufacturing leads to misalignment.
- While curing, the pressure is not uniformly distributed.
- The storage of carbon\epoxy prepregs.

According to the results obtained through the numerical simulations using ABAQUS, it is seen that the thickness imperfections do not significantly affect the curvatures. However, the snapthrough is quite sensitive to the mismatch in the relative thickness between the carbon/epoxy central layer and the hybrid outer layer. A layer named “No Material” is used to model the imperfection as seen in Figure 7-12.

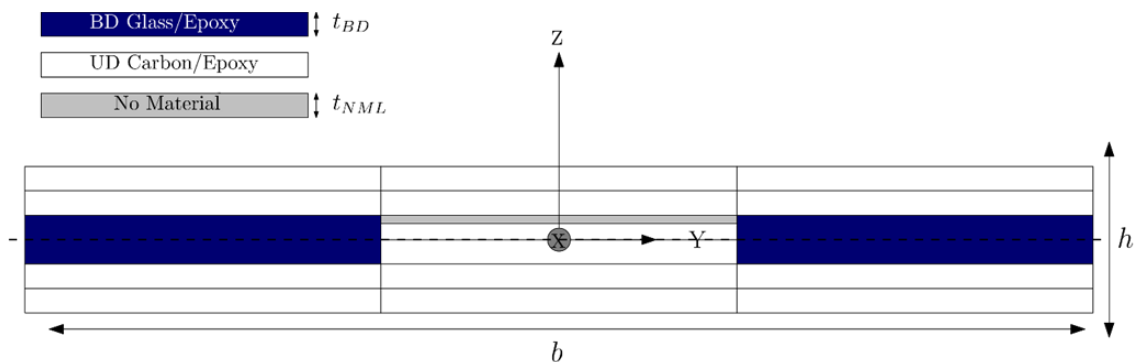


Figure 7-12: Schematic figure of the thickness mismatch.

This layer is assumed to have no material. The material properties of the No material layer are very close to zero. By introducing such a layer, geometric symmetry may be maintained while creating asymmetry in the material layup. The load-deflection curve obtained through the FE simulations for different levels of thickness mismatch between the central carbon/epoxy and hybrid layers is shown in Figure 7-13. In the load-displacement plots, asymmetry is observed due to the imperfection. It is also seen that as the mismatch thickness increases, the asymmetry of the load-displacement plot increases. Initially, a force acting in the positive direction is used to cause a forward

snaphthrough. It is observed that the snaphthrough loads tend to be higher during reverse snapping than in forward snapping. For instance, the layup consisting of bi-directional glass/epoxy layers of thickness 0.35 mm and carbon\epoxy layer of thickness 0.125 mm, and no material layer of thickness 0.1 mm, has a forward snaphthrough load of 0.680 N and a reverse snaphthrough (snapback) load of 0.460 N. In addition, the area under the load-displacement for the perfect and imperfect samples is nearly the same. These similar areas suggest that both the perfect and imperfect samples store a similar amount of thermal strain energy after curing. The total thickness of the laminate is summarized in Table 14.

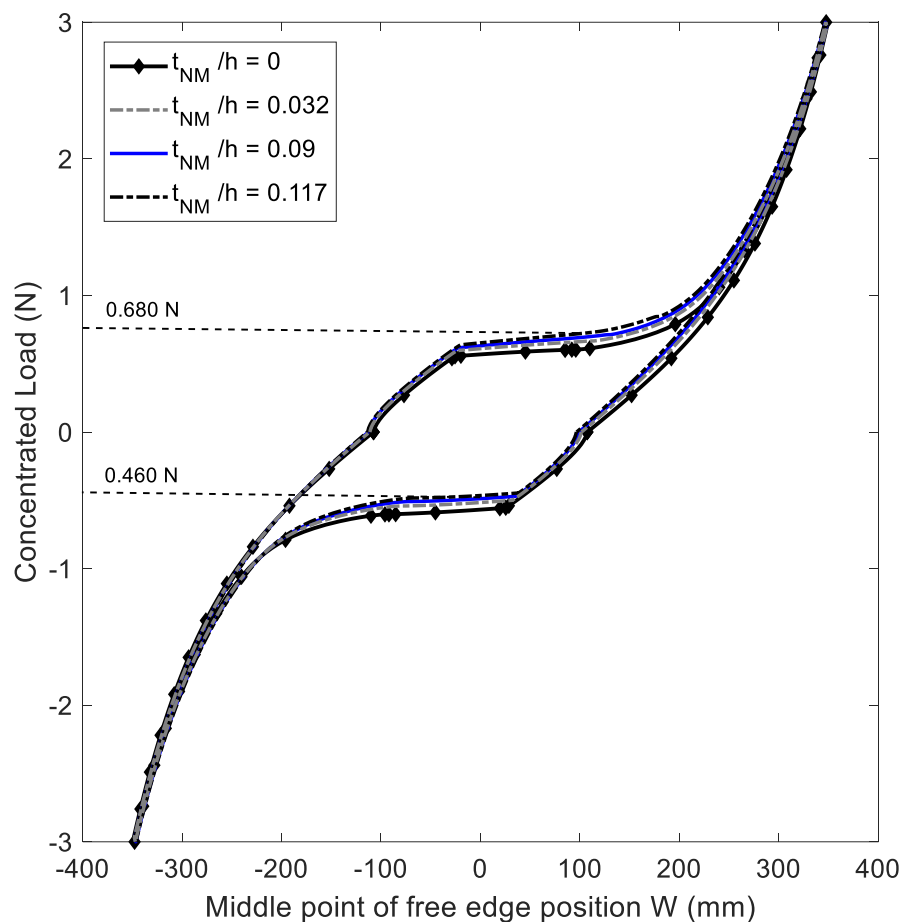


Figure 7-13: Load-displacement plot at different -no material- layer thickness.

Table 14: No material layer thickness.

	Thickness $t$ (mm)			
	Carbon/Epoxy UD	Glass/Epoxy BD	No Material	Total Laminate
$t_{BD}/h = 0.333; t_{NM}/h = 0$	0.125	0.25	0	0.75
$t_{BD}/h = 0.354; t_{NM}/h = 0.032$	0.125	0.275	0.025	0.775
$t_{BD}/h = 0.393; t_{NM}/h = 0.09$	0.125	0.325	0.075	0.825
$t_{BD}/h = 0.412; t_{NM}/h = 0.117$	0.125	0.35	0.1	0.85

## Chapter 8. Conclusion and Future Work

The objective of this thesis is to investigate the static configuration and the snapthrough response of an innovative bistable cantilevered composite wing. First, we presented available models in the literature. The first model was restricted to free-free boundary conditions for unsymmetric bistable laminates. Next, the model was modified to include variation of curvature within the domain to account for boundary conditions other than free-free, however, the unsymmetric laminates found to lose their bistability behavior when they are clamped or attached to a larger structure. Therefore, the hybrid bistable symmetric laminate (HBSL) was then validated with free-free and clamped boundary conditions. Throughout the literature, the snapthrough characteristics of the m-HBSL for different geometric parameters was not yet investigated. Hence, the first part of the thesis started with implementing snapthrough analysis of the HBSL for different geometric parameters.

From the results obtained, it was observed that the snapthrough characteristics is very sensitive to the geometric parameters. The first parametric study conducted on the m-HBSL, was the width of the bi-directional plies. As the width of the bi-directional ply increases, the snapthrough load increases. However, beyond a certain width of BD, the curvature gradually decreases to zero.

The next parameter considered was the thickness of the bi-directional layers. It was seen that as the thickness increases, the snapthrough load increases and a stiffer structure was achieved. The third parameter considered for the m-HBSL is the location of the bi-directional layers. For the base configuration, the bi-directional layers are placed at the center of the laminate. Results showed that as the bi-directional glass/epoxy layers are placed away from the centerline, the snapthrough increases and the deflection of the equilibrium shapes decreases.

Using bistable laminates for structural applications requires understanding the changes in snapthrough characteristic of the bistable laminates when they are integrated as a part of a larger structure. Along this line, the second part of the thesis proposed a simplified model in which the m-HBSL is a part of another structure. The proposed model is i-HBSL referred to as “innovative hybrid bistable symmetric laminate”. Next, a parametric study on the i-HBSL was performed. The first three parametric studies

conducted on the i-HBSL are similar to those performed on the single m-HBSL plate and a similar snapthrough characteristics behavior was achieved. However, when the m-HBSL is attached to another elastic structure, the flexibility increases. The next parametric study on the i-HBSL was the effect of changing the length of the flat segment on the snapthrough load and equilibrium shape. Results showed that changing the length of the flat segment does not affect the deflection of the equilibrium shapes. Yet, the flexibility of the structure increases, resulting in a lower snapthrough load. Another factor considered was the location of the concentrated load along the wingspan. The change in the location of the applied force from the fixed end results in intermediate stable states, as seen in numerical simulations. The last factor considered was the thickness mismatch, which may result during the manufacturing of the hybrid bistable laminates. It was observed that the asymmetry caused by the imperfection results in the loss of symmetry in the load-displacement plots. The snapthrough loads differs from the snapback loads. The performed parametric studies on both m-HBSL and i-HBSL highlight the importance of the geometric and material parameters on the snapthrough characteristics. Also, the parametric study gives the designers more choices based on their design requirements.

### **8.1. Future Work**

Bistable Laminates are still in the early stage of development, as a result, there is considerable scope for future development in manufacturing, design, and modeling. Below are some suggestions in this regard

- Bistable laminates are most used as structural elements for aerostructures. Therefore, designing potential morphing mechanisms requires consideration of the fluid structure interaction.
- Study the dynamic response of the HBSL under aerodynamic loads and harmonic mechanical loads.
- The model was limited to a specific case of m-HBSL and i-HBSLs with cantilever boundary conditions. To handle different boundary conditions and layups, a different framework is needed.

## References

- [1] M. R. Schultz, “A Concept for Airfoil-like Active Bistable Twisting Structures.,” *Journal of Intelligent Material Systems and Structures.*, vol. 19, no. 2, pp. 157-69, 2008.
- [2] F. Mattioni, P. M. Weaver, K. D. Potter and M. I. Friswell, “Analysis of thermally induced multistable composites,” *International Journal of Solids and Structures*, vol. 45, no. 2, pp. 657-675, 2008.
- [3] M. W. Hyer, “Some Observations on the Cured Shape of Thin Unsymmetric Laminates,” *Journal of Composite Materials*, pp. 175-194, 1981.
- [4] K. S. Kim and H. T. Hahn, “Residual stress development during processing of graphite/epoxy composites,” *Composites Science and Technology*, vol. 36, no. 2, pp. 121-132, 1989.
- [5] S. R. White and H. T. Hahn, “Process modeling of composite-materials – residual-stress development during cure. 1. Model formulation,” *J Compos Mater*, vol. 26, no. 16, pp. 2402-2422, 1992.
- [6] M. R. Schultz, M. W. Hyer, R. B. Williams, W. K. Wilkie and D. J. Inman, “Snap-through of unsymmetric laminates using piezocomposite actuators,” *Composites Science and Technology*, vol. 66, no. 14, pp. 2442-2448, 2006.
- [7] M. Gude and W. Hufenbach, “Design of novel morphing structures based on bistable composites with piezoceramic actuators,” *Mechanics of Composite Materials*, vol. 42, no. 4, p. 339–346, 2006.
- [8] C. R. Bowen, R. Butler, R. Jervis, H. A. Kim and A. I. T. Salo, “Morphing and Shape Control using Unsymmetrical Composites,” *Journal of Intelligent Material Systems and Structures*, vol. 18, no. 1, pp. 89-98, 2007.
- [9] M. L. Dano and M. W. Hyer, “SMA-induced snap-through of unsymmetric fiber-reinforced composite laminates,” *International Journal of Solids and Structures*, vol. 40, no. 22, pp. 5949-7683, 2003.

- [10] A. Mukherjee , M. I. Friswell, F. S. Ali and A. Arockiarajan, “Modeling and design of a class of hybrid bistable symmetric laminates with,” *Composite Structures*, vol. 239, p. 112019, 2020.
- [11] S. A. Emam and D. J. Inman, “A Review on Bistable Composite Laminates for Morphing and Energy Harvesting,” *Applied Mechanics Reviews*, vol. 67, no. 6, p. 060803, 2015.
- [12] M. W. Hyer, “The Room-Temperature Shapes of Four-Layer Unsymmetric Cross-Ply Laminates,” *Journal of Composite Materials*, vol. 16, no. 4, p. 318–340, 1982.
- [13] W. J. Jun and C. S. Hong, “Effect of residual shear strain on the cured shape of unsymmetric cross-ply thin laminates,” *Composites Science and Technology*, vol. 38, no. 1, pp. 55-67, 1990.
- [14] M. Schlecht, K. Schulte and M. Hyer, “Advanced calculation of the roomtemperature,” *Journal of Composite Materials*, vol. 32, no. (1-4), pp. 627-633, 1995.
- [15] M. L. Dano and M. W. Hyer, “Snap-through of unsymmetric fiber-reinforced composite laminates,” *International Journal of Solids and Structures*, vol. 39, no. 1, pp. 175-198, 2002.
- [16] S. Daynes and P. Weaver, “Analysis of unsymmetric cfrp–metal hybrid laminates for use in adaptive structures.,” *Composites Part A: Applied Science and Manufacturing*, vol. 41, no. 11, pp. 1712-1718, 2010.
- [17] S. Daynes, C. Diaconu and P. Weaver, “Bistable prestressed symmetric laminates,” *Journal of Composite Materials*, vol. 44, no. 9, pp. 1119-1137, 2010.
- [18] C. Sousa, P. Camanho and A. Suleman, “Analysis of multistable variable stiffness composite plates,” *Composite Structures*, vol. 98, pp. 34-46, 2013.

- [19] A. Haldar, J. Reinoso, E. Jansen and R. Rolfes, “Thermally induced multistable configurations of variable stiffness composite plates,” *Composite Structures*, vol. 183, pp. 161-175, 2018.
- [20] P. Anilkumar, A. Haldar, E. Jansen, B. Rao and R. Rolfes, “Design optimization of multistable variable-stiffness laminates,” *Mechanics of Advanced Materials and Structures*, vol. 26, no. 1, pp. 48-55, 2019.
- [21] A. Firouzian-Nejad, C. Bowen, S. Mustapha, M. Ghayour and S. Ziaei-Rad, “Bi-stable hybrid composite laminates containing metallic strips: an experimental,” *Smart Materials and Structures*, vol. 28, no. 5, p. 055030, 2019.
- [22] F. Mattioni , P. M. Weaver and M. Friswell, “Multistable composite plates with piecewise variation of lay-up in the planform,” *International Journal of Solids and Structures*, vol. 46, no. 1, pp. 151-164, 2009.
- [23] A. Arrieta, I. K. Kuder, T. Waeber and P. Ermanni, “Variable stiffness characteristics of embeddable multi-stable composites,” *Composites Science and Technology*, vol. 97, pp. 12-18, 2014.
- [24] S. Daynes, K. Potter and P. Weaver, “Bistable prestressed buckled laminates,” *Composites Science and Technology*, vol. 68, no. 15-16, p. 3431–3437, 2008.
- [25] L. H. F. Dai, P. Weaver and S. Du, “Bistable hybrid symmetric laminates,” *Composite Structures*, vol. 116, pp. 782-792, 2014.
- [26] C. G. Diaconu, M. P. Weaver and F. Mattioni, “Concepts for morphing airfoil sections using bi-stable laminated composite structures,” *Thin-Walled Structures*, vol. 46, pp. 689-701, 2008.
- [27] F. Mattioni, M. P. Weaver, D. K. Potter and I. M. Friswell, “The application of thermally induced multistable composites to morphing aircraft structures,” *SPIE*, vol. 6930, pp. 310-320, 2008.

- [28] S. Daynes, P. M. Weaver and K. D. Potter, "Aeroelastic Study of Bistable Composite Airfoils," *Journal of Aircraft*, vol. 46, no. 6, pp. 2169-2174, 2009.
- [29] M. L. Dano and M. W. Hyer, "Thermally-induced deformation behavior of unsymmetric laminates," *International Journal of Solids and Structures*, vol. 35, no. 17, p. 2101–2120, 1998.
- [30] M. F., P. Weaver and M. Friswell, "Multistable composite plates with piecewise variation of lay-up in the planform," *International Journal of Solids and Structures*, pp. 151-164, 2009.
- [31] C. Dong, S. and I. J. Davies, "Flexural Properties of E Glass and TR50S Carbon Fiber Reinforced Epoxy Hybrid Composites," *Journal of Materials Engineering and Performance*, vol. 22, p. 41, 2013.
- [32] F. C. Campbell, *Structural Composite Materials*, Ohio: ASM International, 2010, pp. 1-31.
- [33] M. Amabili, *Nonlinear Mechanics of Shells and Plates in Composite, Soft and Biological Materials*, Cambridge: Cambridge University Press, 2018, pp. 90-123.
- [34] M. W. Hyer, *Stress Analysis of Fiber-Reinforced Composite Materials*, Lancaster: DEStech Publications, 2009, p. 222.
- [35] A. Elmiladi, V. Petrović, A. Grbovic, A. Sedmak and I. Balac, "Numerical evaluation of thermal stresses generated in laminated composite structure exposed to low temperatures," *Thermal Science*, vol. 25, no. 0, p. 338, 2020.
- [36] B. Kalaycioglu and M. H. Dirikolu, "Investigation of the design of a metal-lined fully wrapped composite vessel under high internal pressure," *High Pressure Research*, vol. 30, no. 3, pp. 428-437, 2010.



## Appendix A. Fundamentals of Composite Materials

### A.1. Lamina and Laminate

Composite materials are defined as two or more materials. A laminate is particular kind of composite material formed when two or more lamina are stacked together. Lamina or (Individual Ply) is defined as a flat arrangement of continuous long or discontinuous fibers in a matrix, examples of continuous and discontinuous arrangements are seen in Figure A-1.

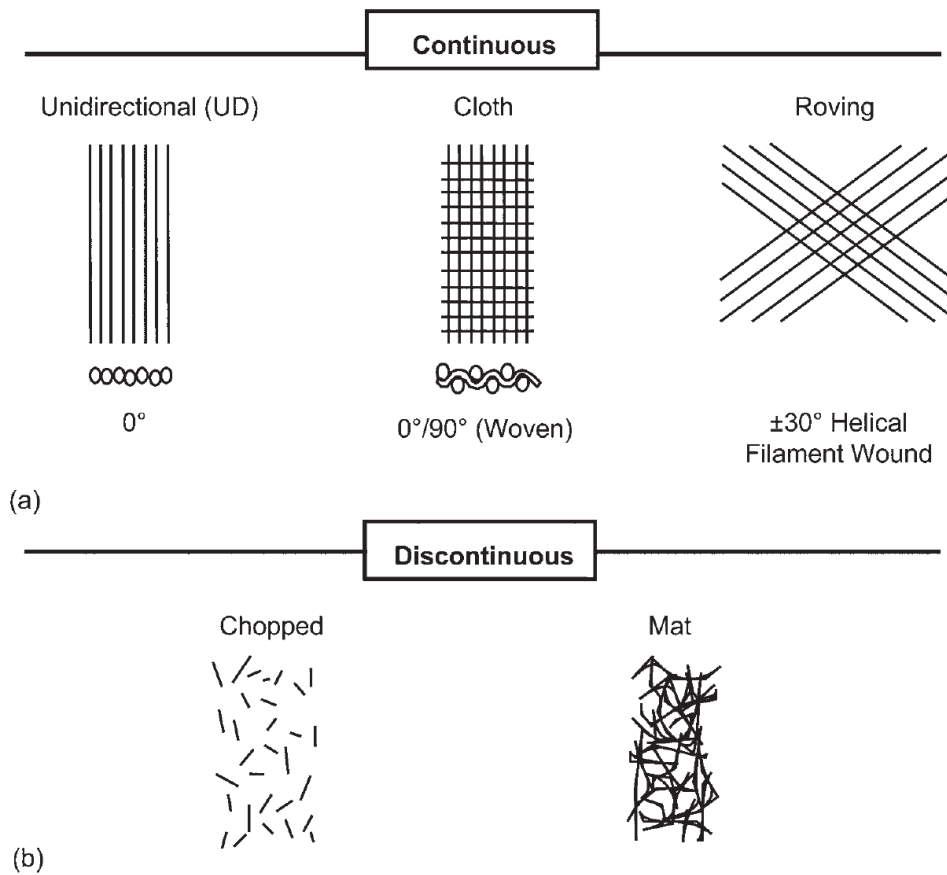


Figure A-1: Various types of fiber orientation (a) Continuous (b) Discontinuous [32].

### A.2. Fibers and Matrix

The length of a fiber is always greater than its diameter. The ratio between the length and diameter of a fiber is known as *aspect ratio*. The aspect ratio of a continuous fibers are larger than the discontinuous fibers. In addition, the orientation of the continuous fibers are very organized. On the other hand, the orientation of the discontinuous fibers is random. Moreover, the cost of the continuous fibers are high

compared to the discontinuous fibers. Hence, it is only used when the strength and stiffness are more important than the cost. The laminates are made by stacking sheets of continuous fibers in different orientation to obtain the desired strength and stiffness. The strength of fibers are increased by reducing the diameter. However, producing fibers with smaller diameter is an expensive process. The fibers are maintained in the proper orientation and spacing through the matrix. Also, the matrix provide protection from abrasion and environment for the fibers. Currently, three types of fiber reinforcements are in common use in polymer matrix composites; carbon-based, graphite fibers or glass-based fibers. Laminates are defined as plates which are made by combining number of layers, each layer is called ply or lamina shown in Figure A-2 and can have different material and different mechanical properties. The mechanical properties of the laminate are obtained using the stiffness matrix, which can be calculated from the properties of the plies, thickness and their stacking sequence. The linear plate bending theory defines the behaviour of the laminate.

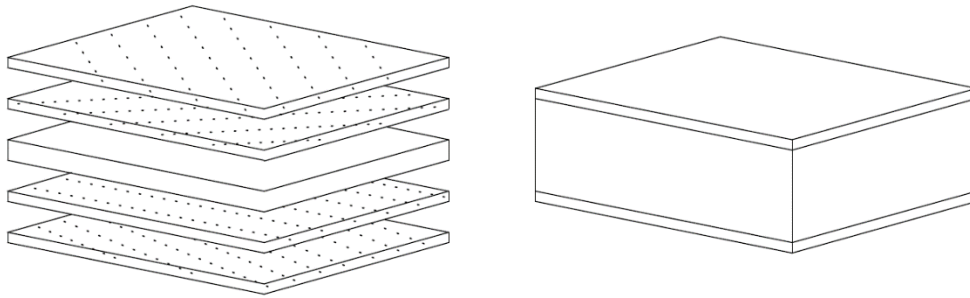


Figure A-2: Scheme of a laminate composite material.

### A.3. Elastic Material Behaviour in Composite Material

**A.3.1. Stiffness matrix  $C_{ij}$ .** The general law relating stresses to strains is defined as the following

$$\sigma_i = C_{ij}\varepsilon_j \quad (A1)$$

The stress components are defined as  $\sigma_i$ , the stiffness matrix is represented by  $C_{ij}$  and  $\varepsilon_j$  for the strain components. The stress-strain relationship and the corresponding stiffness matrix is related using the following:

$$\begin{Bmatrix} \sigma_1 \\ \sigma_2 \\ \sigma_3 \\ \tau_{23} \\ \tau_{13} \\ \tau_{12} \end{Bmatrix} = \begin{bmatrix} C_{11} & C_{12} & C_{13} & C_{14} & C_{15} & C_{16} \\ C_{21} & C_{22} & C_{23} & C_{24} & C_{25} & C_{26} \\ C_{31} & C_{32} & C_{33} & C_{34} & C_{35} & C_{36} \\ C_{41} & C_{42} & C_{43} & C_{44} & C_{45} & C_{46} \\ C_{51} & C_{52} & C_{53} & C_{54} & C_{55} & C_{56} \\ C_{61} & C_{62} & C_{63} & C_{64} & C_{65} & C_{66} \end{bmatrix} \begin{Bmatrix} \varepsilon_1 \\ \varepsilon_2 \\ \varepsilon_3 \\ \gamma_{23} \\ \gamma_{13} \\ \gamma_{12} \end{Bmatrix} \quad (\text{A2})$$

**A.3.2. Compliance matrix  $S_{ij}$ .** The inverse of the previous stress-strain relationship is defined to resolve for the elastic material behaviour. A significant coupling effect occur between the applied stress and the resulting deformation. Hence, this expression shows the different types of coupling for an anisotropic material.  $S_{11}$ ,  $S_{22}$  and  $S_{33}$  represent the coupling due to the individual applied stress  $\sigma_1$ ,  $\sigma_2$ ,  $\sigma_3$ , respectively, in the same direction (Extension). On the other hand,  $S_{44}$ ,  $S_{55}$  and  $S_{66}$  represent the response to the shear strain due to the applied shear stress in the same plane.  $S_{12}$ ,  $S_{13}$  and  $S_{23}$  defines the extension-extension coupling (Poisson Effect).  $S_{14}$ ,  $S_{15}$ ,  $S_{16}$ ,  $S_{24}$ ,  $S_{25}$ ,  $S_{26}$ ,  $S_{34}$ ,  $S_{35}$  and  $S_{36}$  represent the shear-extension coupling. Finally,  $S_{45}$ ,  $S_{46}$  and  $S_{56}$  represent the shear-shear coupling.

$$\varepsilon_i = S_{ij}\sigma_j \quad (\text{A3})$$

$$\begin{Bmatrix} \varepsilon_1 \\ \varepsilon_2 \\ \varepsilon_3 \\ \gamma_{23} \\ \gamma_{13} \\ \gamma_{12} \end{Bmatrix} = \begin{bmatrix} S_{11} & S_{12} & S_{13} & S_{14} & S_{15} & S_{16} \\ S_{21} & S_{22} & S_{23} & S_{24} & S_{25} & S_{26} \\ S_{31} & S_{32} & S_{33} & S_{34} & S_{35} & S_{36} \\ S_{41} & S_{42} & S_{43} & S_{44} & S_{45} & S_{46} \\ S_{51} & S_{52} & S_{53} & S_{54} & S_{55} & S_{56} \\ S_{61} & S_{62} & S_{63} & S_{64} & S_{65} & S_{66} \end{bmatrix} \begin{Bmatrix} \sigma_1 \\ \sigma_2 \\ \sigma_3 \\ \tau_{23} \\ \tau_{13} \\ \tau_{12} \end{Bmatrix} \quad (\text{A4})$$

It is seen that the compliance matrix for an anisotropic material has 21 independent elastic constants. However, if the material possess orientational symmetries, the number of the independent elastic constants will reduce. An example of this is the orthotropic material which has three planes of symmetry and it is independent on 9 elastic constants only. Hence, the compliance for an orthotropic material can be written as:

$$S^{ortho} = \begin{bmatrix} S_{11} & S_{12} & S_{13} & 0 & 0 & 0 \\ S_{21} & S_{22} & S_{23} & 0 & 0 & 0 \\ S_{31} & S_{32} & S_{33} & 0 & 0 & 0 \\ 0 & 0 & 0 & S_{44} & 0 & 0 \\ 0 & 0 & 0 & 0 & S_{55} & 0 \\ 0 & 0 & 0 & 0 & 0 & S_{66} \end{bmatrix} \quad (A5)$$

The compliance matrix for the orthotropic therefore can be written as the following:

$$\begin{Bmatrix} \varepsilon_1 \\ \varepsilon_2 \\ \varepsilon_3 \\ \gamma_{23} \\ \gamma_{13} \\ \gamma_{12} \end{Bmatrix} = \begin{bmatrix} \frac{1}{E_1} & \frac{-\nu_{21}}{E_2} & \frac{-\nu_{31}}{E_3} & 0 & 0 & 0 \\ \frac{-\nu_{12}}{E_1} & \frac{1}{E_2} & \frac{-\nu_{32}}{E_3} & 0 & 0 & 0 \\ \frac{-\nu_{13}}{E_1} & \frac{-\nu_{23}}{E_2} & \frac{1}{E_3} & 0 & 0 & 0 \\ 0 & 0 & 0 & \frac{1}{G_{23}} & 0 & 0 \\ 0 & 0 & 0 & 0 & \frac{1}{G_{13}} & 0 \\ 0 & 0 & 0 & 0 & 0 & \frac{1}{G_{12}} \end{bmatrix} \begin{Bmatrix} \sigma_1 \\ \sigma_2 \\ \sigma_3 \\ \tau_{23} \\ \tau_{13} \\ \tau_{12} \end{Bmatrix} \quad (A6)$$

**A.3.3. Plane-stress assumption.** An important assumption in the development of the mechanics of fiber-reinforced materials is the *plane-stress assumption*. In many engineering applications, where the fiber-reinforced composite material are used in plates, beams or cylinders. In these structures, three of the six components of stress are smaller than the other three. Hence, they can be described using the 2-D case of plane stress shown in Figure A-3. In the plane-stress assumption,  $\sigma_1$ ,  $\sigma_2$  and  $\tau_{12}$  lie in the 2-D plane. On the other hand,  $\sigma_3$ ,  $\tau_{23}$  and  $\tau_{13}$  are perpendicular to this plane and are set to zero since the lamina is able to resist stresses in the fiber direction only, any stresses produced out of the 2-D plane (1-2 plane) would subject the lamina to unnatural stresses. Using the equation in 6, we can say that:

$$\begin{aligned} \sigma_3 &= \sigma_{23} = \sigma_3 = 0 \\ \varepsilon_3 &= S_{13}\sigma_1 + S_{23}\sigma_2 \\ \gamma_{23} &= 0 \quad \gamma_{13} = 0 \end{aligned} \quad (A7)$$

Applying the plane-stress assumption, the  $6 \times 6$  stiffness matrix can be reduced to  $3 \times 3$  matrix, and the strain-stress relation can be represented as the following:

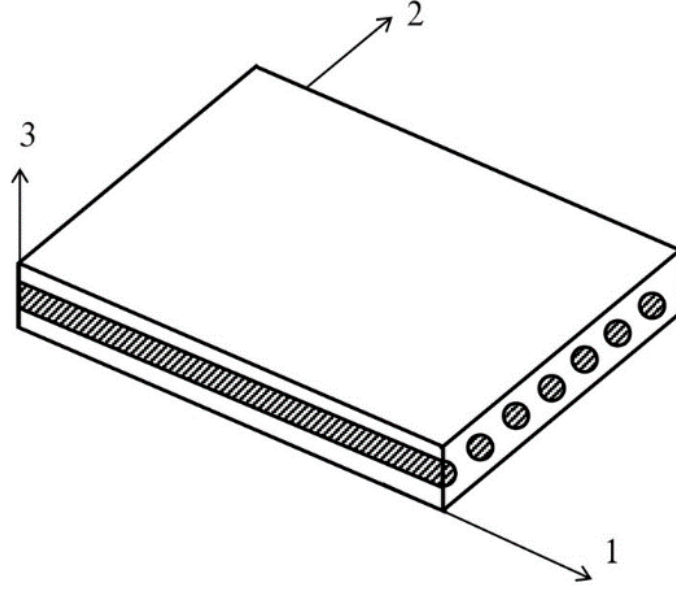


Figure A-3: Coordinates of unidirectional reinforced lamina [33].

$$\begin{Bmatrix} \varepsilon_1 \\ \varepsilon_2 \\ \frac{1}{2}\gamma_{12} \end{Bmatrix} = \begin{bmatrix} S_{11} & S_{12} & 0 \\ S_{21} & S_{22} & 0 \\ 0 & 0 & \frac{1}{2}S_{66} \end{bmatrix} \begin{Bmatrix} \sigma_1 \\ \sigma_2 \\ \tau_{12} \end{Bmatrix} \quad (\text{A8})$$

Similarly, the stress-strain relation can be reduced to the following:

$$\begin{Bmatrix} \sigma_1 \\ \sigma_2 \\ \tau_{12} \end{Bmatrix} = \begin{bmatrix} Q_{11} & Q_{12} & 0 \\ Q_{21} & Q_{22} & 0 \\ 0 & 0 & 2Q_{66} \end{bmatrix} \begin{Bmatrix} \varepsilon_1 \\ \varepsilon_2 \\ \frac{1}{2}\gamma_{12} \end{Bmatrix} \quad (\text{A9})$$

where  $Q_{ij}$  represent the reduced stiffness matrix of the lamina. The components of the reduced stiffness can be related to the compliance matrix and material properties (elastic constants) by the following:

$$\begin{aligned} Q_{11} &= \frac{S_{22}}{S_{11}S_{22}-S_{12}^2} = \frac{E_1}{1-\nu_{12}\nu_{21}} \\ Q_{12} &= Q_{21} = \frac{S_{12}}{S_{11}S_{22}-S_{12}^2} = \frac{\nu_{12}E_2}{1-\nu_{12}\nu_{21}} \\ Q_{22} &= \frac{S_{11}}{S_{11}S_{22}-S_{12}^2} = \frac{E_2}{1-\nu_{12}\nu_{21}} \\ Q_{66} &= \frac{1}{S_{66}} = G_{12} \end{aligned} \quad (\text{A10})$$

**A.3.4. Transformation of axes - ply orientation.** It is necessary to transform the axes from the global coordinate system  $x - y$  frame to the principal coordinate system. The transformation law for Cartesian Cauchy stress can be written as:

$$\begin{aligned}\sigma_1 &= \sigma_x \cos^2 \theta + \sigma_y \sin^2 \theta + 2\tau_{xy} \sin \theta \cos \theta \\ \sigma_2 &= \sigma_x \sin^2 \theta + \sigma_y \cos^2 \theta + 2\tau_{xy} \sin \theta \cos \theta \\ \tau_{12} &= (\sigma_y - \sigma_x) \sin \theta \cos \theta + \tau_{xy} (\cos^2 \theta - \sin^2 \theta)\end{aligned}\quad (\text{A11})$$

where  $\theta$  is defined as the angle from the  $x$  axis in the global coordinate system to fiber axis 1.

***Principal System 1-2 to Global Coordinate System  $x-y$***

The equations shown in 11 can be represented as the following:

$$\begin{pmatrix} \sigma_1 \\ \sigma_2 \\ \tau_{12} \end{pmatrix} = \begin{bmatrix} c^2 & s^2 & 2sc \\ s^2 & c^2 & -2sc \\ -sc & sc & c^2 - s^2 \end{bmatrix} \begin{pmatrix} \sigma_x \\ \sigma_y \\ \tau_{xy} \end{pmatrix}\quad (\text{A12})$$

where  $c = \cos \theta$  and  $s = \sin \theta$ , and the transformation matrix is defined as:

$$T = \begin{bmatrix} c^2 & s^2 & 2sc \\ s^2 & c^2 & -2sc \\ -sc & sc & c^2 - s^2 \end{bmatrix}\quad (\text{A13})$$

Similarly, the transformation matrix can also be applied to the strain tensor as the following:

$$\begin{pmatrix} \varepsilon_1 \\ \varepsilon_2 \\ \frac{1}{2}\gamma_{12} \end{pmatrix} = \begin{bmatrix} c^2 & s^2 & 2sc \\ s^2 & c^2 & -2sc \\ -sc & sc & c^2 - s^2 \end{bmatrix} \begin{pmatrix} \varepsilon_x \\ \varepsilon_y \\ \frac{1}{2}\gamma_{xy} \end{pmatrix}\quad (\text{A14})$$

***Global Coordinate System  $x-y$  to Principal System 1-2***

Using the inverse of the transformation matrix ( $T^{-1}$ ) shown above, we can move from the global coordinate system ( $x-y$ ) to the principal axis (1-2).

$$\begin{pmatrix} \sigma_x \\ \sigma_y \\ \tau_{xy} \end{pmatrix} = \begin{bmatrix} c^2 & s^2 & -2sc \\ s^2 & c^2 & 2sc \\ sc & -sc & c^2 - s^2 \end{bmatrix} \begin{pmatrix} \sigma_1 \\ \sigma_2 \\ \tau_{12} \end{pmatrix}\quad (\text{A15})$$

**A.3.5. Transformed stiffness and compliance matrices.** The stress-strain relationship in orientated coordinates can be obtained by substituting with eliminating the factor of 2 and  $\frac{1}{2}$  by the following:

$$\begin{Bmatrix} \sigma_x \\ \sigma_y \\ \tau_{xy} \end{Bmatrix} = [T]^{-1} \begin{bmatrix} Q_{11} & Q_{12} & 0 \\ Q_{21} & Q_{22} & 0 \\ 0 & 0 & Q_{66} \end{bmatrix} [T] \begin{Bmatrix} \varepsilon_x \\ \varepsilon_y \\ \gamma_{xy} \end{Bmatrix} \quad (\text{A16})$$

The  $[T]^{-1}Q_{ij}[T]$  term represent the transformed reduced stiffness  $\bar{Q}_{ij}$ . The components of the stiffness matrix of the transformed lamina are represented by the following:

$$\begin{aligned} \bar{Q}_{11} &= Q_{11} \cos^4\theta + Q_{22} \sin^4\theta + 2(Q_{12} + Q_{66}) \sin^2\theta \cos^2\theta \\ \bar{Q}_{12} &= \bar{Q}_{21} = (Q_{11} + Q_{22} - 4Q_{66}) \sin^2\theta \cos^2\theta + Q_{12} (\cos^4\theta + \sin^4\theta) \\ \bar{Q}_{22} &= Q_{11} \sin^4\theta + Q_{22} \cos^4\theta + 2(Q_{12} + 2Q_{66}) \sin^2\theta \cos^2\theta \\ \bar{Q}_{16} &= \bar{Q}_{61} = (Q_{11} - Q_{12} - 2Q_{66}) \cos^3\theta \sin\theta - (Q_{22} - Q_{12} - Q_{66}) \cos\theta \sin^3\theta \\ \bar{Q}_{26} &= \bar{Q}_{62} = (Q_{11} - Q_{12} - 2Q_{66}) \cos\theta \sin^3\theta - (Q_{22} - Q_{12} - Q_{66}) \cos^3\theta \sin\theta \\ \bar{Q}_{66} &= (Q_{11} + Q_{22} - 2Q_{12} - 2Q_{66}) \sin^2\theta \cos^2\theta + Q_{66} (\sin^4\theta + \cos^4\theta) \end{aligned} \quad (\text{A17})$$

Therefore, the stress-strain relation of the transformed lamina can be obtained using the transformed reduced stiffness by the following:

$$\begin{Bmatrix} \sigma_x \\ \sigma_y \\ \tau_{xy} \end{Bmatrix} = \begin{bmatrix} \bar{Q}_{11} & \bar{Q}_{12} & \bar{Q}_{16} \\ \bar{Q}_{21} & \bar{Q}_{22} & \bar{Q}_{26} \\ \bar{Q}_{16} & \bar{Q}_{26} & \bar{Q}_{66} \end{bmatrix} \begin{Bmatrix} \varepsilon_x \\ \varepsilon_y \\ \gamma_{xy} \end{Bmatrix} \quad (\text{A18})$$

## A.4. Laminate Formulation

**A.4.1. Classical lamination theory.** For one lamina or ply ( $k$ ) the components of strain in the global coordinate system can be related to the strain in the mid-plane and the curvature of the mid-plane using the plate theory. The main assumptions of the plate theory are the following:

- Each lamina is a homogeneous layer such that its effective properties are known.
- Each lamina is in a state of plane stress.
- The individual lamina can be isotropic, orthotropic or transversely isotropic.
- The laminate deforms according to the Kirchhoff assumptions for bending and stretching of thin plates as assumed in classical plate theory and seen in Figure A-4. The assumptions are the following:

- The normal to the mid-plane remain straight and normal to the mid-plane even after deformation.
- The normal to the mid-plane do not change their lengths.

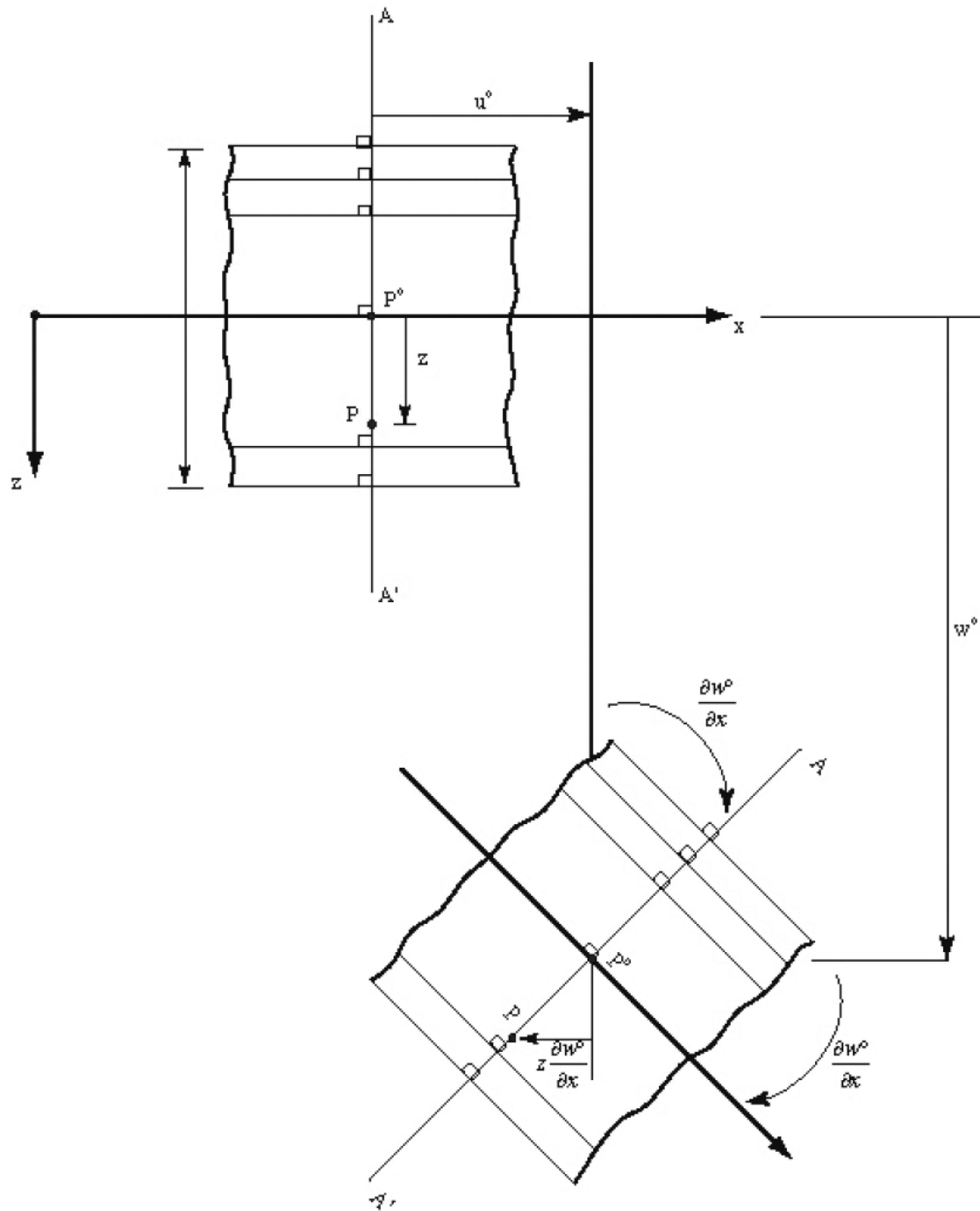


Figure A-4: Schematic of laminate deformation [34].

**A.4.2. Laminate displacements.** The horizontal translation of any point  $P$  with coordinates  $(x, y, z)$  on the normal to the mid-plane is the following:

$$u(x, y, z) = u^o(x, y) - z \frac{\partial w^o(x, y)}{\partial x} \quad (\text{A19})$$

Where the horizontal translation of point  $P_o$  the x-direction is presented as  $u_o$ , on the other hand, the vertical translation and rotation of the reference surface about the y axis at point  $P_o$  are denoted as  $w_o$  and  $\frac{\partial w^o}{\partial x}$ , respectively. The rotation of point  $P_o$  causes the point  $P$  to translate horizontally in the negative x-direction by an amount  $z \frac{\partial w^o}{\partial x}$ . Similarly, the horizontal translation of point  $P$  with coordinates  $(x, y, z)$  in the direction of the y axis is given by the following:

$$v(x, y, z) = v^o(x, y) - z \frac{\partial w^o(x, y)}{\partial y} \quad (\text{A20})$$

Also, the vertical translation of point  $P$  in the direction of the z-axis is given by the following:

$$w(x, y, z) = w^o(x, y) \quad (\text{A21})$$

**A.4.3. Laminate strains.** Next, the strains that result from the displacement are investigated.

$$\epsilon_x(x, y, z) = \frac{\partial u(x, y, z)}{\partial x} = \frac{\partial u^o(x, y)}{\partial x} - z \frac{\partial^2 w^o(x, y)}{\partial x^2} \quad (\text{A22})$$

$$\epsilon_x(x, y, z) = \epsilon_x^o(x, y) + z \kappa_x^o(x, y) \quad (\text{A23})$$

The  $\epsilon_x^o$  is the extensional strain of the reference surface in the x-direction and  $\kappa_x^o$  is the curvature of the reference surface in the x-direction.

$$\epsilon_y(x, y, z) = \frac{\partial v(x, y, z)}{\partial y} = \frac{\partial v^o(x, y)}{\partial y} - z \frac{\partial^2 w^o(x, y)}{\partial y^2} \quad (\text{A24})$$

$$\epsilon_y(x, y, z) = \epsilon_y^o(x, y) + z \kappa_y^o(x, y) \quad (\text{A25})$$

where  $\epsilon_y^o$  is the extensional strain of the reference surface in the y-direction and  $\kappa_y^o$  is the curvature of the reference surface in the y-direction. Similarly, the shear strain is defined as the following:

$$\gamma_{xy}(x, y, z) = \frac{\partial v(x, y, z)}{\partial x} + \frac{\partial u(x, y, z)}{\partial y} = \frac{\partial v^o(x, y)}{\partial x} + \frac{\partial u^o(x, y)}{\partial y} - 2z \frac{\partial^2 w^o(x, y)}{\partial x \partial y} \quad (\text{A26})$$

$$\gamma_{xy}(x, y, z) = \gamma_{xy}^o(x, y) + z\kappa_{xy}^o(x, y) \quad (\text{A27})$$

where  $\gamma_{xy}^o(x, y)$  refers to the reference surface inplane shear strain, and  $\kappa_{xy}^o(x, y)$  is the reference surface twisting curvature.

**A.4.4. Laminate stresses.** Each point within the volume of laminate is in a state of plane stress based on the classical lamination theory. Therefore, the stresses can be computed using the transformed reduced stiffness matrix if the strains and curvature of the reference surface are known.

$$\begin{Bmatrix} \sigma_x \\ \sigma_y \\ \tau_{xy} \end{Bmatrix} = \begin{bmatrix} \bar{Q}_{11} & \bar{Q}_{12} & \bar{Q}_{16} \\ \bar{Q}_{21} & \bar{Q}_{22} & \bar{Q}_{26} \\ \bar{Q}_{16} & \bar{Q}_{26} & \bar{Q}_{66} \end{bmatrix} \begin{Bmatrix} \varepsilon_x^o + z\kappa_x^o \\ \varepsilon_y^o + z\kappa_y^o \\ \gamma_{xy}^o + z\kappa_{xy}^o \end{Bmatrix} \quad (\text{A28})$$

**A.4.5. The ABD matrix.** The ABD matrix is a  $6 \times 6$  matrix and it is a link between the applied loads and moments and the associated strains and curvature of the laminate. The loads and moments are presented per unit width of the laminate cross section. The resultant force and moments acting on the laminate are determined by integrating the stresses in each ply through the thickness of the laminate.

$$N_k = \int_{z_{k-1}}^{z_k} \sigma_k dz \quad (\text{A29})$$

$$\begin{Bmatrix} N_x \\ N_y \\ N_{xy} \end{Bmatrix} = \int_{-h/2}^{h/2} \begin{bmatrix} \sigma_x \\ \sigma_y \\ \sigma_{xy} \end{bmatrix} dz = \sum_{k=1}^N \int_{z_{k-1}}^{z_k} \begin{Bmatrix} \sigma_x \\ \sigma_y \\ \sigma_{xy} \end{Bmatrix}^k dz \quad (\text{A30})$$

$$\begin{Bmatrix} M_x \\ M_y \\ M_{xy} \end{Bmatrix} = \int_{-h/2}^{h/2} \begin{bmatrix} \sigma_x \\ \sigma_y \\ \sigma_{xy} \end{bmatrix} z dz = \sum_{k=1}^N \int_{z_{k-1}}^{z_k} \begin{Bmatrix} \sigma_x \\ \sigma_y \\ \sigma_{xy} \end{Bmatrix}^k z dz \quad (\text{A31})$$

where the  $z_k$  and  $z_{k-1}$  shown in Figure A-5 represent the geometry of the laminate. Substituting Eq. (A28) in Eqs. (A30) and (A31) leads to the following:

$$\begin{Bmatrix} N_x \\ N_y \\ N_{xy} \end{Bmatrix} = \sum_{k=1}^N \begin{bmatrix} \bar{Q}_{11} & \bar{Q}_{12} & \bar{Q}_{16} \\ \bar{Q}_{21} & \bar{Q}_{22} & \bar{Q}_{26} \\ \bar{Q}_{16} & \bar{Q}_{26} & \bar{Q}_{66} \end{bmatrix} \left[ \int_{z_{k-1}}^{z_k} \begin{bmatrix} \varepsilon_x^o \\ \varepsilon_y^o \\ \gamma_{xy}^o \end{bmatrix} dz + \int_{z_{k-1}}^{z_k} \begin{bmatrix} \kappa_x^o \\ \kappa_y^o \\ \kappa_{xy}^o \end{bmatrix} z dz \right] \quad (\text{A32})$$

$$\begin{Bmatrix} M_x \\ M_y \\ M_{xy} \end{Bmatrix} = \sum_{k=1}^N \begin{bmatrix} \bar{Q}_{11} & \bar{Q}_{12} & \bar{Q}_{16} \\ \bar{Q}_{21} & \bar{Q}_{22} & \bar{Q}_{26} \\ \bar{Q}_{16} & \bar{Q}_{26} & \bar{Q}_{66} \end{bmatrix} \left[ \int_{z_{k-1}}^{z_k} \begin{bmatrix} \varepsilon_x^o \\ \varepsilon_y^o \\ \gamma_{xy}^o \end{bmatrix} z dz + \int_{z_{k-1}}^{z_k} \begin{bmatrix} \kappa_x^o \\ \kappa_y^o \\ \kappa_{xy}^o \end{bmatrix} z^2 dz \right] \quad (\text{A33})$$

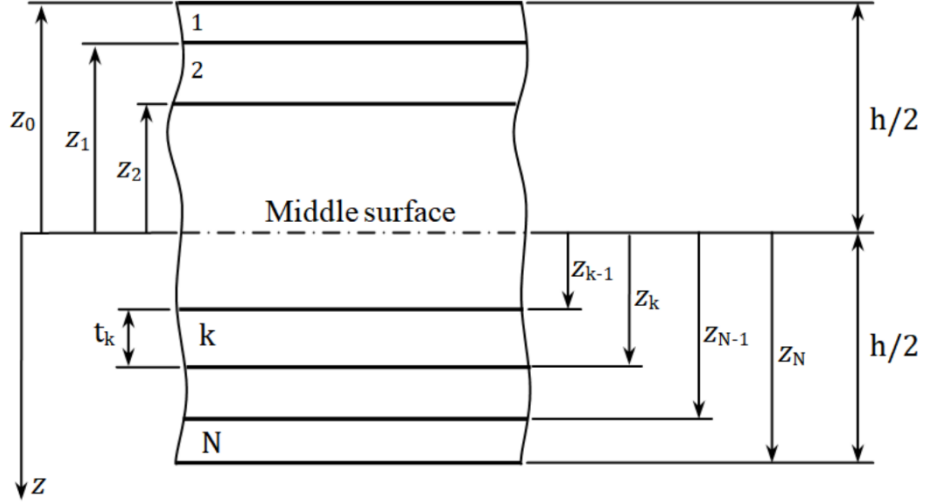


Figure A-4: Laminated plate geometry

Since the strains and curvatures of the reference surface or mid-plane are independent on  $z$ , and the transformed reduced stiffness does not change within a given layer or lamina, both terms can be removed from the integral. The resultant force is then expressed as:

$$N = \sum_{k=1}^N (\bar{Q}_{ij} \varepsilon^o \int_{z_{k-1}}^{z_k} dz + \bar{Q}_{ij} \kappa^o \int_{z_{k-1}}^{z_k} z dz) \quad (\text{A34})$$

Similarly, the moment resultant per unit width can be defined as:

$$M = \sum_{k=1}^N (\bar{Q}_{ij} \varepsilon^o \int_{z_{k-1}}^{z_k} z dz + \bar{Q}_{ij} \kappa^o \int_{z_{k-1}}^{z_k} z^2 dz) \quad (\text{A35})$$

The A, B and D matrices are determined using:

$$A_{ij} = \sum_{k=1}^N \bar{Q}_{ij}^k (z_k - z_{k-1}) \quad (\text{A36})$$

$$B_{ij} = \frac{1}{2} \sum_{k=1}^N \bar{Q}_{ij}^k (z_k^2 - z_{k-1}^2) \quad (\text{A37})$$

$$D_{ij} = \frac{1}{3} \sum_{k=1}^N \bar{Q}_{ij}^k (z_k^3 - z_{k-1}^3) \quad (\text{A38})$$

Now, the resultant force and moments can be combined and related to the strains and curvatures in the mid-plane using the ABD matrix *Laminate stiffness matrix* and the inverse is the *Laminate compliance matrix*.

$$\begin{bmatrix} N \\ M \end{bmatrix} = \begin{bmatrix} A & B \\ B & D \end{bmatrix} \begin{bmatrix} \varepsilon^o \\ \kappa^o \end{bmatrix} \quad (\text{A39})$$

where the  $A_{ij}$  matrix defines the extensional stiffness.  $A_{13}$  and  $A_{23}$  represent the shear-extension coupling. The presence of  $B_{ij}$  implies coupling between bending and extension of a laminate. On the other hand, the  $D_{ij}$  matrix is bending stiffness. Where, the bend-twist coupling is represented by  $D_{13}$  and  $D_{23}$  components seen in Figure A-6.

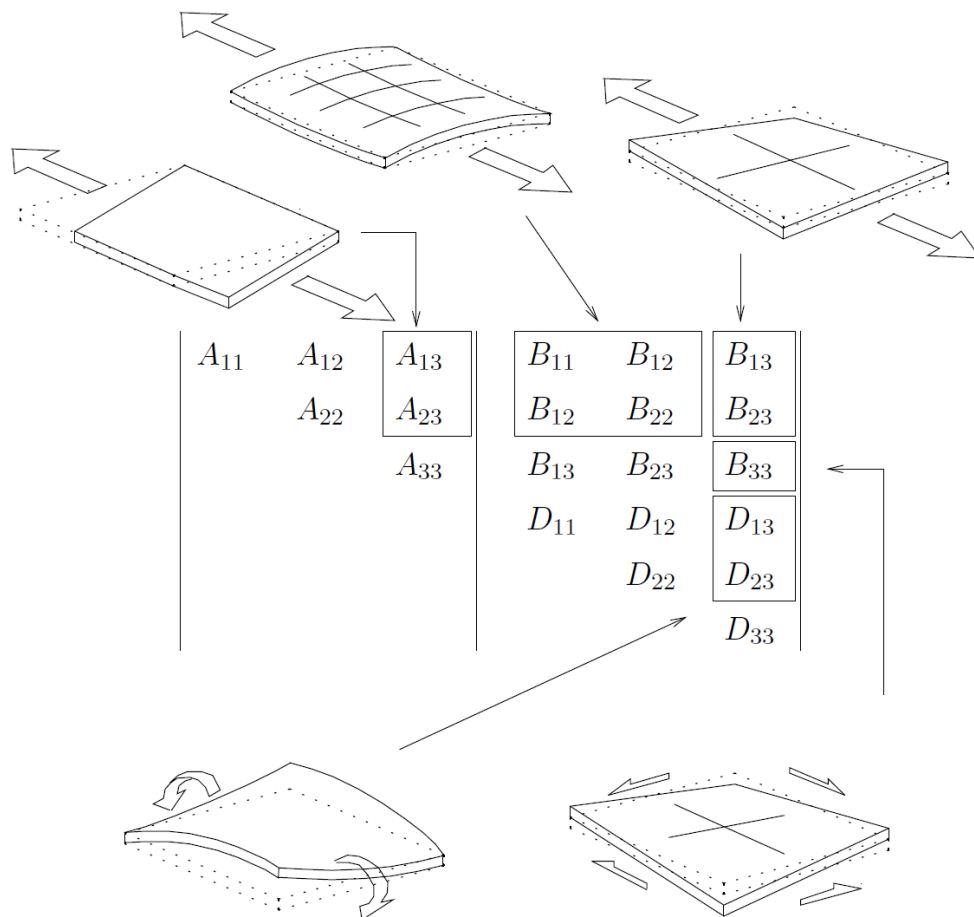


Figure A-5: ABD-matrix components and their impact on the laminate deformation [34].

**A.4.6. Laminate layup and stacking.** A laminate is made up of Lamina with different fiber orientations and it is important to understand the manner in which the laminate lay-up is specified, i.e., stacking sequence notation. For equal thickness layers laminates, a listing of the layers and their orientation suffices, for example, [0/90/45]. If multiple laminae occur at the same angle, then we can present it with a subscript to specify the number of such multiple layers, [0/0/0/90/90] = [0<sub>3</sub>/90<sub>2</sub>]. If the sequences of laminae are repeated, then we can present the sequence as a group with a subscript indicating the number of sequence repetition, [0/90/45/0/90/45] = [0/90/45]<sub>2</sub>. For a symmetric laminate, where the laminae are placed symmetrically with respect to the middle surface of the laminate, the representation is [0/90/45/45/90/0] = [0/90/45]<sub>s</sub> (even number of plies), [0/45/90/45/0] = [0/45/ $\bar{90}$ ]<sub>s</sub> (odd number of plies). If no repetition or symmetry of sequence is indicated, then we can present a subscript T to indicate complete or total specification for emphases, [0/90/45/−45/0/90]<sub>T</sub>.

The different types of laminates commonly used are the following:

*i. Symmetric Laminates*

For a symmetric laminate, the laminae are placed symmetrically with respect to the middle surface of the laminate, i.e., if one ply is at a certain distance above the middle surface, the other ply must have the same distance below the middle surface as seen in Figure A-7a. In addition, each pair has the same material properties, fiber orientation and  $(\bar{Q}_{ij})_k$ . Hence, the extension coupling stiffness  $B_{ij}$  is zero due to the symmetry.

*ii. Unsymmetric Laminates*

Unsymmetric laminates represent any laminate which is not symmetric about with respect to the mid-plane as shown in Figure A-7b, and  $D_{13} = D_{23} = 0$ . For a symmetric laminate, when the composite is cured at the elevated temperature to hold the fibers together by activating the matrix, and then cooled back to the room temperature, the laminate does not bend or twist since the coupling between bending and extension is eliminated  $B_{ij}$ . On the other hand, the unsymmetric laminate tends to deform during the cooling process. This is the reason why most of the commercial composite structures prefers symmetric laminates over unsymmetric laminates.

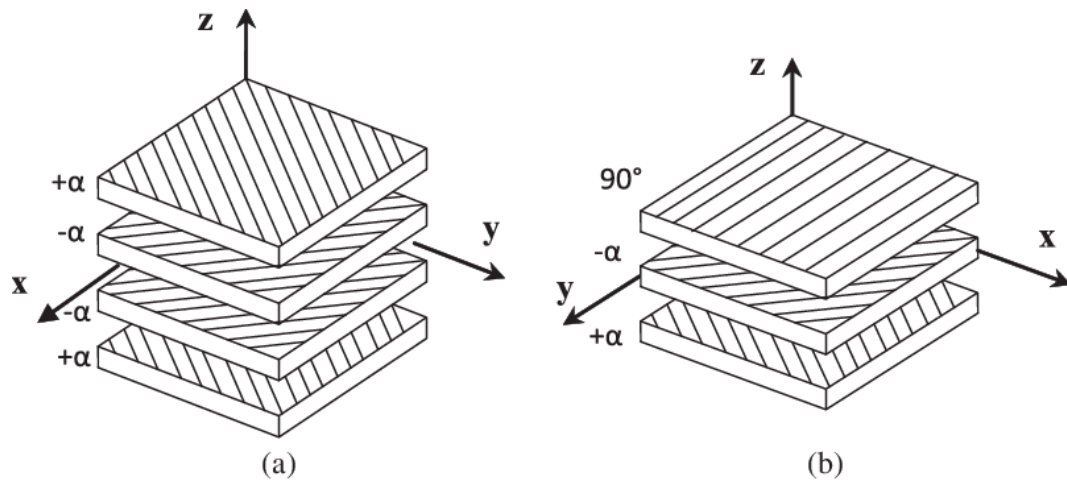


Figure A-6: (a) Symmetric Laminate (b) Unsymmetric Laminate [36].

The deformation of the unsymmetric laminate was found to be undesirable during the initial stages of the composite research. However, the unsymmetric laminates were then used in many structural applications where a significant curvature or twist is required. The classical lamination theory predicted the cured shape of the unsymmetric laminate to be saddle shape where the curvature are defined as  $\kappa_x = -\kappa_y$  or vice versa. Later on it was found that the cured shape of the unsymmetric laminate is found to be cylindrical, where,  $(+\kappa_x, -\kappa_y = 0)$  and a second cylindrical shape  $(\kappa_x = 0, +\kappa_y)$ . The phenomena to go from one stable configuration to another was also introduced, called "Snap through & Snap back". Hence, bistability or Bistable Composites was first introduced to field of composite material by Hyer [29].

Laminates can also be classified as the following:

- Cross-ply [90/0/90/0] are orthotropic plies where the orientation of fibers in alternating plies are at right angle of each other ( $A_{13} = A_{23} = 0$ ). Material directions = global directions.
- Angle-ply are orthotropic plies where each ply material direction (1) is rotated at angle  $\theta$  with respect to the global direction  $x$ .

**A.4.7. Thermal loading.** Thermal strains occur due to thermal expansion when the laminate is subjected to change in temperature. Each lamina or ply has different thermal strain, leading to deformation. It is known that the effect of temperature is more pronounced in composites than on metals and this is due to the large difference in coefficient of thermal expansion between the laminate layers. When a fiber-reinforced

composite material is heated or cooled, the material expands or contracts. The parameter that indicates the extent to which the material is expanded or contracted is referred to *Coefficient of thermal expansion* ( $\alpha$ ), the unit is  $1/C^\circ$ , it is related to strains. Hence, the unit can also be written as  $mm/mm/C^\circ$ . The thermal expansion coefficient is linearly proportional to the temperature change for a linear uniform objects.

The thermal strains are defined as the following:

$$\varepsilon_x^T(T, T_{ref}) = \alpha_x \Delta T \quad (A40)$$

$$\varepsilon_y^T(T, T_{ref}) = \alpha_y \Delta T \quad (A41)$$

$$\varepsilon_z^T(T, T_{ref}) = \alpha_z \Delta T \quad (A42)$$

$$\gamma_{xy}^T(T, T_{ref}) = \alpha_{xy} \Delta T \quad (A43)$$

The coefficients of thermal expansion in x-y-z system are referred as:

$$\alpha_x = \alpha_1 \cos^2 \theta + \alpha_2 \sin^2 \theta \quad (A44)$$

$$\alpha_y = \alpha_1 \sin^2 \theta + \alpha_2 \cos^2 \theta \quad (A45)$$

$$\alpha_{xy} = 2(\alpha_1 - \alpha_2) \cos \theta \sin \theta \quad (A46)$$

$$\alpha_z = \alpha_3 \quad (A47)$$

## **Vita**

Sara Hijazi was born in 1997, in Abu Dhabi, United Arab Emirates. She received her primary and secondary education in Abu Dhabi, UAE. She received her B.Sc. degree in Aeronautical Engineering from Emirates Aviation University.

In January 2020, she joined the Mechanical Engineering master's program in the American University of Sharjah as a graduate teaching assistant. Her research interests are in composite structures and nonlinear dynamics.